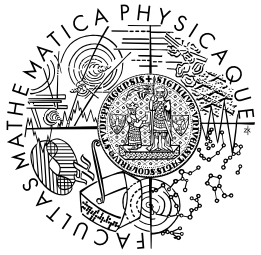

FACULTY
OF MATHEMATICS
AND PHYSICS
Charles University

BACHELOR THESIS

Michal Stratený

Orbital dynamics around a black hole surrounded by matter

Institute of Theoretical Physics

Supervisor of the bachelor thesis: Georgios Loukes Gerakopoulos, Ph.D.
Study programme: Physics
Study branch: Physics

Prague 2023

I declare that I carried out this bachelor thesis independently, and only with the cited sources, literature and other professional sources. It has not been used to obtain another or the same degree.

I understand that my work relates to the rights and obligations under the Act No. 121/2000 Sb., the Copyright Act, as amended, in particular the fact that the Charles University has the right to conclude a license agreement on the use of this work as a school work pursuant to Section 60 subsection 1 of the Copyright Act.

In ..... date ....

Author's signature

I would like to acknowledge and give my thanks to my supervisor, Georgios Loukes Gerakopoulos, who made this thesis possible. His dedicated guidance and advice carried me through all the stages of writing my thesis.

Názov práce: Orbitální dynamika v okolí černé díry obklopené hmotou

Autor: Michal Stratený

Ústav: Ústav teoretické fyziky

Vedúci bakalárskej práce: Georgios Loukes Gerakopoulos, Ph.D., Astronomický ústav Akademie věd České republiky

Abstrakt: Táto práca študuje dynamiku geodetického pohybu v zakrivenom priestoročase okolo Schwarzschildovej čiernej diery, perturbovanej gravitačným poľom vzdialenej osovo symetrickej distribúcie hmoty obklopujúcej systém. Tento konkrétny priestoročas môže slúžiť ako všestranný model pre rôznorodé astrofyzikálne scenáre. V úvode práce je poskytnutý stručný prehľad teórie klasických mechanických systémov a vlastností geodetického pohybu. Taktiež je poskytnuté stručné uvedenie do teórie integrability a neintegrability spolu s podstatnými nástrojmi pre analýzu neintegrabilných systémov, zahrňujúc Poincarého rezy a rotačné čísla. Tieto metódy sú následne aplikované na skúmaný priestoročas pomocou numerických metód. Využitím rotačných čísel sú vypočítané šírky rezonancií, ktoré sú neskôr použité k stanoveniu vzťahu medzi pertubačným parametrom a parametrom charakterizujúcim perturbovanú metriku.

Kľúčové slova: geodetický pohyb, čierne diery, chaos

Title: Orbital dynamics around a black hole surrounded by matter

Author: Michal Stratený

Institute: Institute of Theoretical Physics

Supervisor: Georgios Loukes Gerakopoulos, Ph.D., Astronomical Institute, Czech Academy of Sciences

Abstract: This thesis studies the dynamics of geodesic motion within a curved spacetime around a Schwarzschild black hole, perturbed by a gravitational field of a far axisymmetric distribution of mass enclosing the system. This particular spacetime can serve as a versatile model for a diverse range of astrophysical scenarios. At the beginning of the thesis, a brief overview of the theory of classical mechanical systems and properties of geodesic motion are provided. A brief introduction to the theory of integrability and non-integrability, along with essential tools for analysis of non-integrable systems, including Poincaré surface of section and rotation numbers, is provided as well. These methods are subsequently applied to the under study spacetime through numerical methods. By utilising the rotation numbers, the widths of resonances are calculated, which are then used in establishing the relation between the perturbation parameter and the parameter characterising the perturbed metric.

Keywords: geodesic motion, black holes, chaos

Contents

Introduction

The present thesis studies the geodesic motion within a curved spacetime around a Schwarzschild black hole, perturbed by the gravitational field of a far axisymmetric distribution of mass enclosing the system.

The perturbation of a Schwarzschild black hole by a surrounding matter field can serve as a model for a diverse range of physical scenarios. Notably, massive black holes located in the centres of galaxies are often surrounded by dense nuclear star clusters and other molecular and dust structures [1]. Furthermore, alternative sources of external matter can come from more exotic sources, such as dark matter or scalar fields [2, 3].

Additionally, the perturbation of the Schwarzschild black hole by the surrounding matter can have observational implications on the evolution of extreme mass ratio binary systems consisting of a compact stellar-mass object and a supermassive black hole. In such systems, which are known as extreme mass ratio inspirals, the compact stellar-mass object inspirals into the supermassive black hole, emitting gravitational waves. These gravitational waves peak in the mHz frequency band and are expected to be observed by the next generation of gravitational-wave observatories [4, 5, 6].

A key aspect of Schwarzschild spacetime is its integrability, as the equations of motion can be solved analytically [7]. However, by perturbing the spacetime, the system is no longer entirely symmetrical, which results in the loss of one of the integrals of motion. The insufficient number of integrals of motion leads to non-integrability, which allows chaotic behaviour to emerge.

We focus mainly on resonances, parts of the phase space where two or more characteristic frequencies of the system match in integer ratios. These regions are key parts of the study of chaos because there strongly emerges chaotic behaviour. There are studies, see, e.g., [8] and references therein, showing that such regions can have an observational impact on the gravitational waves emitted during an extreme mass ratio inspiral, since a resonance crossing is expected to cause a dephasing of the gravitational waveforms. Hence, investigating the strength and the growth of the resonances is important for the preparation of the gravitational waveforms needed to detect the signal from an extreme mass ratio inspiral [9].

The thesis is organised as follows. The first chapter begins by introducing the metric tensor and providing a brief overview of the theory of classic mechanical systems and the properties of geodesic motion. Then in the rest of the chapter, we introduce the theory of integrability and the canonical perturbation theory method, along with tools to study non-integrable systems. The chapter concludes with the definition of deterministic chaos. The second chapter presents our numerical results obtained from the computation of geodesic motion within studied curved spacetime. The thesis attachments include a summary of the accuracy achieved by the employed numerical methods.

1. Theoretical foundations

1.1 Notation and conventions

This thesis is founded upon the theoretical framework of the theory of general relativity. The notation follows canonical books on the theory of relativity, such as the Refs. [10, 11]. In particular, abstract index notation is used, wherein indices indicate the type of quantity rather than necessarily representing components on any basis. Greek indices can assume any value 0, 1, 2, or 3, while spatial indices take on values 1, 2, or 3 and are denoted by Latin indices. Whenever the indices are not just abstract, the symbol X^α represents all components, or any individual component, of the quantity X, i.e. $X^\alpha \equiv (X^0, X^1, X^2, X^3)$. In sections encompassing classical mechanics, lowercase, upright boldface font denotes vector quantities.

The covariant metric tensor is denoted as $g_{\alpha\beta}$, and its signature is chosen as $(-+++)$. The contravariant version of the metric tensor is denoted as $g^{\alpha\beta}$. Their corresponding matrices are mutually inverse, which can be expressed by the following identity

$$\sum_\rho g^{\alpha\rho} g_{\rho\beta} \equiv g^{\alpha\rho} g_{\rho\beta} = \delta^\alpha_\beta. \tag{1.1}$$

In the first equivalency, Einstein's summation convention is introduced. This convention implies that in such expressions, we omit the summation symbol for any index which goes over all its possible values and has appeared once as a covariant and once as a contravariant index in a product. The last symbol δ^α_β represents the four-dimensional Kronecker delta, which has the meaning:

$$\delta^\alpha_\beta = \begin{cases} 1 & \text{if } \alpha = \beta, \\ 0 & \text{if } \alpha \neq \beta. \end{cases} \tag{1.2}$$

In general, indices are raised and lowered using the metric tensor; for instance,

$$g_{\mu\nu} A^\mu B^\nu = A_\nu B^\nu = A_\nu B_\mu g^{\mu\nu}. \tag{1.3}$$

The partial derivative is denoted by ∂ or, equivalently, by a comma in an index location; for example,

$$\frac{\partial X^\alpha}{\partial x^\lambda} \equiv \partial_\lambda X^\alpha \equiv X^\alpha{}_{,\lambda}. \tag{1.4}$$

The covariant derivative is denoted by ∇ or by a semicolon in an index location; for instance,

$$\frac{\partial X^\alpha}{\partial x^\lambda} + \Gamma^\alpha{}_{\rho\lambda} X^\rho \equiv \nabla_\lambda X^\alpha \equiv X^\alpha{}_{;\lambda}. \tag{1.5}$$

Higher mixed derivatives are ordered according to

$$X^\alpha{}_{,\lambda\sigma} \equiv \partial_\sigma \partial_\lambda X^\alpha \equiv \frac{\partial^2 X^\alpha}{\partial x^\sigma x^\lambda} \equiv \frac{\partial}{\partial x^\sigma}\left(\frac{\partial X^\alpha}{\partial x^\lambda}\right). \tag{1.6}$$

A dot over variable indicates a derivative with respect to time (for example, $\dot{q}^i \equiv dq^i/dt$ in section 1.4 at page 7) or a derivative with respect to proper time

(for example, $\dot{x}^\alpha \equiv dx^\alpha/d\tau$ in section 1.3 at page 6). The semantic interpretation of the symbol shall be established by its contextual usage.

We denote

$$\Gamma_{\sigma\kappa\lambda} = \frac{1}{2}\left(g_{\sigma\kappa,\lambda} + g_{\lambda\sigma,\kappa} - g_{\kappa\lambda,\sigma}\right), \tag{1.7}$$

$$\Gamma^{\mu}{}_{\kappa\lambda} = \frac{1}{2}g^{\mu\sigma}\left(g_{\sigma\kappa,\lambda} + g_{\lambda\sigma,\kappa} - g_{\kappa\lambda,\sigma}\right), \tag{1.8}$$

as Christoffel symbols of the first kind, respectively, second kind.

Throughout the remainder of this thesis, we will adopt geometric units where $c = 1$ (c represents the speed of light) and $G = 1$ (G represents the gravitation constant).

1.2 Metric

This thesis studies geodesic motion in curved spacetime around a black hole, perturbed by a faraway gravitating ring surrounding the system. The metric was introduced in Ref. [6], where it is also outlined its derivation. This metric expresses a spacetime around a non-spinning black hole of mass M encircled by a rotating gravitating ring with mass $\mathscr{M}_r$ at a radius $r_r \gg M$ much larger than the black hole horizon. The gravitational field near the black hole is influenced by the tidal effects caused by the presence of the ring. Apart from assuming that the black hole is static and stationary in the inertial frame, we also truncate the multipole structure of the ring to the leading quadrupolar order. Then we obtain, in Schwarzschild-like coordinates (t, r, θ, ϕ), the resulting metric valid near the black hole, given by the line element:

$$\begin{aligned} ds^2_{r\ll r_r} = &-\left(1 - \frac{2M}{r}\right)(1 + 2\nu_{\mathscr{Q}})\,dt^2 + \frac{1 + 2\chi_{\mathscr{Q}} - 2\nu_{\mathscr{Q}}}{1 - 2M/r}dr^2 \\ &+ (1 - 2\nu_{\mathscr{Q}})r^2\left[(1 + 2\chi_{\mathscr{Q}})d\theta^2 + \sin^2\theta d\phi^2\right], \end{aligned} \tag{1.9}$$

$$\nu_{\mathscr{Q}} \equiv \frac{\mathscr{Q}}{4}\left[r(2M - r)\sin^2\theta + 2(M - r)^2\cos^2\theta - 6M^2\right], \tag{1.10a}$$

$$\chi_{\mathscr{Q}} \equiv \mathscr{Q}M(M - r)\sin^2\theta, \tag{1.10b}$$

with $\mathscr{Q} \equiv \mathscr{M}_r/r_r^3$ representing the quadrupole perturbation parameter. The local metric is approximately vacuum, static, and axisymmetric with respect to the local time t and azimuthal angle ϕ. The metric is approximately part of the Weyl-type metrics class as it is a static and axisymmetric solution to the Einstein's field equations [12]. However, it should be noted that metric (1.9) is valid only for $r \ll r_r$ and assumes non-compact rings, i.e. $\mathscr{M}_r \ll r_r$. Especially, it neglects all terms starting from $\mathscr{O}(r_r^{-4})$ and $\mathscr{O}(\mathscr{M}_r^2)$.

1.3 Geodesic equations

The theory of general relativity is a geometric theory of gravitation. The natural state of motion influenced by gravity is a *free fall*; thus, it is crucial for this thesis to establish for it a rigorous mathematical framework.

Free fall is the straightest path through spacetime followed by a freely falling, neutral test body, independent of its internal structure and composition. To construct the straightest possible curve, we take a short segment of the curve and move it forward, step by step, always parallel to itself. Ultimately, we obtained such an extremal world-line whose tangent vector transports along it parallelly. We emphasise extremal because, in Euclidean space, a straight line means the shortest connection, whereas, in spacetime, it is not always the shortest.

As demonstrated in Ref. [13], if we take a small segment dx^α of a geodesic curve and displace it forward, parallel to itself, through a displacement dx^α equal to itself, the segment undergoes a change described by:

$$\delta dx^\alpha = -\Gamma^\alpha{}_{\mu\nu} dx^\mu dx^\nu. \tag{1.11}$$

To convert this to the differential equation, it is essential to introduce a parametrisation of the curve, with an affine parameter λ increasing monotonically along the curve. If $d\lambda$ is the increment of this parameter that corresponds to the displacement dx^α, the aforementioned equation can be divided by $(d\lambda)^2$ and rewritten as

$$\frac{d^2x^\alpha}{d\lambda^2} + \Gamma^\alpha{}_{\mu\nu} \frac{dx^\mu}{d\lambda} \frac{dx^\nu}{d\lambda} = 0. \tag{1.12}$$

One should realise that the above equation 1.12 represents four second-order ordinary differential equations. Therefore, two initial conditions, the initial position $x^\alpha\,(\lambda = \lambda_{\text{in}})$ and initial tangent vector $\frac{dx^\alpha}{d\lambda}\,(\lambda = \lambda_{\text{in}})$ must be specified. Let us say that the above only holds for a point-like particle (characterised purely by its rest mass).

Considering the rest of the thesis, we will constrain to time-like geodesics; the Eq. (1.12) could be shortened by choosing the affine parameter as the particle's proper time, transforming the *geodesic equations* to

$$\ddot{x}^\alpha + \Gamma^\alpha{}_{\mu\nu} \dot{x}^\mu \dot{x}^\nu = 0. \tag{1.13}$$

1.4 Lagrangian formalism

The Lagrangian formalism is a formulation of classical mechanics founded upon the principle of least action. For a classical mechanical system, it is often advantageous to define a set of *generalised coordinates* $\mathbf{q} = (q^1, ..., q^n)$ by n arbitrary parameters that are better suited to the symmetries of the problem and completely describe every possible system configuration. To unambiguously describe the possible configuration, there must be as many coordinates as degrees of freedom of the mechanical system.

Generalised coordinates then form *configuration space* $\mathcal{Q}$, which, however, does not possess complete information about the system's mechanical state. As a result, we need to introduce generalised velocities $\dot{\mathbf{q}} = (\dot{q}^1, ..., \dot{q}^n)$, defined as the time derivative of conjugate coordinates $\dot{q}^i \equiv dq^i/dt$. Together, generalised coordinates and velocities form the *velocity phase space* $T\mathcal{Q}$, a complete space of mechanical states. The only missing part is now the equations of motion that govern the time evolution of particles within the space $T\mathcal{Q}$.

According to Ref.[14, 15], the most general formulation leading to equations of motion is the principle of least action. For any mechanical system, the definite

function $\mathcal{L}(\mathbf{q}, \dot{\mathbf{q}}, t)$ is characterised as the *Lagrangian function* of the system. Let the system occupy, at the instants t_1 and t_2, positions defined by vector coordinates $\mathbf{q_1}$ and $\mathbf{q_2}$. The principle of least action states that out of all the conceivable paths between these positions, only those whose action integral

$$\mathcal{S}(\mathbf{q}, t_1, t_2) = \int_{t_1}^{t_2} \mathcal{L}(\mathbf{q}, \dot{\mathbf{q}}, t)\, dt \tag{1.14}$$

is extremal are realised physically. The integral (1.14) is referred to as the *action*. The Lagrangian function contains solely $\mathbf{q}$ and $\dot{\mathbf{q}}$ but not the higher derivatives, implying that only functions $q^i(t)$ have to be determined.

With the application of the variation principle on integral (1.14), we can obtain the Euler-Lagrange's equations:

$$\frac{d}{dt}\frac{\partial \mathcal{L}}{\partial \dot{q}^i} - \frac{\partial \mathcal{L}}{\partial q^i} = 0. \tag{1.15}$$

Mathematically, the equations (1.15) constitute a set of n second-order differential equations for n unknown functions $q^i(t)$. Knowing the $2n$ initial conditions is necessary to determine the system's motion.

In the previous section 1.3 at page 6, we have introduced the geodesic equations, referring to the literature, without further investigation of its physical background, rather than postulating it as a purely geometrical object. We would try to derive it in the section using the Lagrangian formalism.

1.4.1 Derivation of geodesic equations

We again begin with a free test particle moving in curved spacetime. As we know from special relativity (see Ref. [11]), the particle should move along a time-like world-line, which extremises the proper time between two events. Let us label these events A and B. In spacetime, the generalisation of the length is given by the invariant interval $ds^2 = g_{\mu\nu}dx^\mu dx^\nu$, integrated along the curve. For a time-like curve, the interval can be expressed in terms of proper time, $d\tau^2 = -ds^2$. Combining these given facts, we may obtain the corresponding action:

$$\mathcal{S} = \int_A^B d\tau = \int_A^B \sqrt{-ds^2} = \int_A^B \sqrt{-g_{\mu\nu}dx^\mu dx^\nu}. \tag{1.16}$$

In the next step, we introduce a parametrisation of the world-line by an arbitrary parameter λ, which satisfies the condition

$$x^\mu = x^\mu(\lambda) \begin{cases} x^\mu(0) = A \\ x^\mu(1) = B\ . \end{cases} \tag{1.17}$$

Then, we write

$$\tau_{AB} = \int_0^1 \sqrt{-g_{\mu\nu}\frac{dx^\mu}{d\lambda}\frac{dx^\nu}{d\lambda}}d\lambda \equiv \int_0^1 \mathcal{L}\left(x^\mu, \frac{dx^\mu}{d\lambda}\right) d\lambda. \tag{1.18}$$

Here we have formally introduced the relativistic Lagrangian $\mathcal{L}\left(x^\mu, \frac{dx^\mu}{d\lambda}\right)$, in relation to Eq. (1.14). We also note that

$$\mathcal{L} = \frac{d\tau}{d\lambda}, \tag{1.19}$$

which implies how the function $f = f(\tau(\lambda))$, which is parametrised by the parameter λ, transforms the parametrization to the proper time one:

$$\frac{df}{d\lambda} = \frac{df}{d\tau} \cdot \frac{d\tau}{d\lambda} = \mathcal{L}\frac{df}{d\tau}. \tag{1.20}$$

We will use this relation later in derivation to change the derivatives with respect to our arbitrary parameter λ to proper time derivatives.

Having now the form of the Lagrangian, we can proceed to calculate the necessary derivatives in equations (1.15):

$$\begin{aligned} \frac{\partial \mathcal{L}}{\partial x^\alpha} &= -\frac{1}{2\mathcal{L}} g_{\mu\nu,\alpha} \frac{dx^\mu}{d\lambda}\frac{dx^\nu}{d\lambda} \\ &= -\frac{\mathcal{L}}{2} g_{\mu\nu,\alpha} \frac{dx^\mu}{d\tau}\frac{dx^\nu}{d\tau}, \end{aligned} \tag{1.21}$$

$$\begin{aligned} \frac{\partial \mathcal{L}}{\partial\left(\frac{dx^\alpha}{d\lambda}\right)} &= -\frac{1}{2\mathcal{L}} g_{\mu\nu}\left(\frac{dx^\mu}{d\lambda}\delta^\nu_\alpha + \frac{dx^\nu}{d\lambda}\delta^\mu_\alpha\right) \\ &= -\frac{1}{2\mathcal{L}}\left(\frac{dx^\mu}{d\lambda} g_{\mu\alpha} + \frac{dx^\nu}{d\lambda} g_{\alpha\nu}\right) \\ &= -\frac{1}{\mathcal{L}} g_{\alpha\mu}\frac{dx^\mu}{d\lambda} \\ &= -g_{\alpha\mu}\frac{dx^\mu}{d\tau}. \end{aligned} \tag{1.22}$$

The derivative (1.21) is trivial, and we have already proceeded to the proper time parametrisation by employing Eq. (1.20). The second derivative (1.22) requires reindexation of repeated indices. Also, we used the symmetry of the metric and relation (1.20) to obtain the final form.

To continue further, we need to differentiate (1.22) with respect to our arbitrary parameter:

$$\begin{aligned} \frac{d}{d\lambda}\left(\frac{\partial \mathcal{L}}{\partial\left(\frac{dx^\alpha}{d\lambda}\right)}\right) &= \mathcal{L}\frac{d}{d\tau}\left(-g_{\alpha\mu}\frac{dx^\mu}{d\tau}\right) \\ &= -\mathcal{L}\left(g_{\alpha\mu}\frac{d^2x^\mu}{d\tau^2} + \frac{dg_{\alpha\mu}}{d\tau}\frac{dx^\mu}{d\tau}\right) \\ &= -\mathcal{L}\left(g_{\alpha\mu}\frac{d^2x^\mu}{d\tau^2} + g_{\alpha\mu,\nu}\frac{dx^\mu}{d\tau}\frac{dx^\nu}{d\tau}\right), \end{aligned} \tag{1.23}$$

where the only not-trivial is understanding how to operate with the derivatives of the metric. Since

$$\frac{dg_{\mu\nu}}{d\lambda} = \frac{\partial g_{\mu\nu}}{\partial x^\alpha}\frac{dx^\alpha}{d\lambda}, \tag{1.24}$$

we can write Eq. (1.15) as

$$0 = -g_{\alpha\mu}\frac{d^2x^\mu}{d\tau^2} - g_{\alpha\mu,\nu}\frac{dx^\mu}{d\tau}\frac{dx^\nu}{d\tau} + \frac{1}{2} g_{\mu\nu,\alpha}\frac{dx^\mu}{d\tau}\frac{dx^\nu}{d\tau}. \tag{1.25}$$

Multiplying Eq. (1.25) by $g^{\alpha\beta}$, we obtain

$$0 = \frac{d^2x^\beta}{d\tau^2} + \frac{1}{2} g^{\alpha\beta}\left(g_{\alpha\mu,\nu} + g_{\nu\alpha,\mu} - g_{\mu\nu,\alpha}\right)\frac{dx^\mu}{d\tau}\frac{dx^\nu}{d\tau}. \tag{1.26}$$

where one can identify Christoffel symbol of the second kind (1.8). Thus, equation (1.26) becomes

$$0 = \frac{d^2x^\beta}{d\tau^2} + \Gamma^\beta{}_{\mu\nu}\frac{dx^\mu}{d\tau}\frac{dx^\nu}{d\tau}. \tag{1.27}$$

Equation (1.27) is identical to Eq. (1.13) postulated in Section 1.3.

The derivation of the geodesic equations using the Lagrange formalism is perhaps more complicated than using other means. However, it perfectly demonstrates a relationship between classical mechanics and relativistic physics.

At the end of this section, we mention that a seemingly different but utterly equivalent form of the Lagrangian for a free massive particle is the square of the Lagrangian (1.18):

$$\mathscr{L}\left(x^\mu, \frac{dx^\mu}{d\lambda}\right) := g_{\mu\nu}\frac{dx^\mu}{d\lambda}\frac{dx^\nu}{d\lambda} = \pm\mathcal{L}^2\left(x^\mu, \frac{dx^\mu}{d\lambda}\right). \tag{1.28}$$

As shown in Ref. [16], for a Lagrangian along the solution curve parametrised by the proper time, we arrive at $\mathcal{L} \equiv -1$; thus, its square will give the same geodesic equations.

1.5 Hamiltonian formalism

Hamiltonian mechanics is the reformulation of classical mechanics to the language of canonical coordinates and their conjugate momenta. The motivation for Hamiltonian formalism is the availability of the advanced techniques of canonical transformations, symplectic geometry, perturbation theory and other structures, which are less apparent in Lagrangian formalism and can provide deeper insights into the formal structure of mechanics. Moreover, Hamiltonian formalism simplifies numerical work by transitioning the equation of motion from the set of n second-order differential equations to a set of $2n$ first-order differential equations (for the rigorous comparison of the two fundamental formalisms, see Ref. [17])

To perform the transition, mathematically known as Legendre's transformation (see Ref. [18]), it is necessary to introduce a new independent variable called the *canonical momentum* p_i. Once a system has a known Lagrangian, we can define the canonical momentum as

$$p_i := \frac{\partial\mathcal{L}\left(\mathbf{q}, \dot{\mathbf{q}}, t\right)}{\partial q^i}. \tag{1.29}$$

Thus we get a pair of canonically conjugate variables (q^i, p_i) for each degree of freedom. Therefore, we have $2n$ independent variables, forming the phase space $T^*\mathcal{Q}$. A point in such a space fully describes the mechanical state of the system.

The existence of phase space enables the portrayal of the system's time evolution as a unique geometric trajectory dependent solely on the initial conditions. The different sets of the initial conditions are represented by curves (or points), thereby together constituting a *phase portrait* of the system (example shown for Schwarzschild solution in Fig. 1.1).

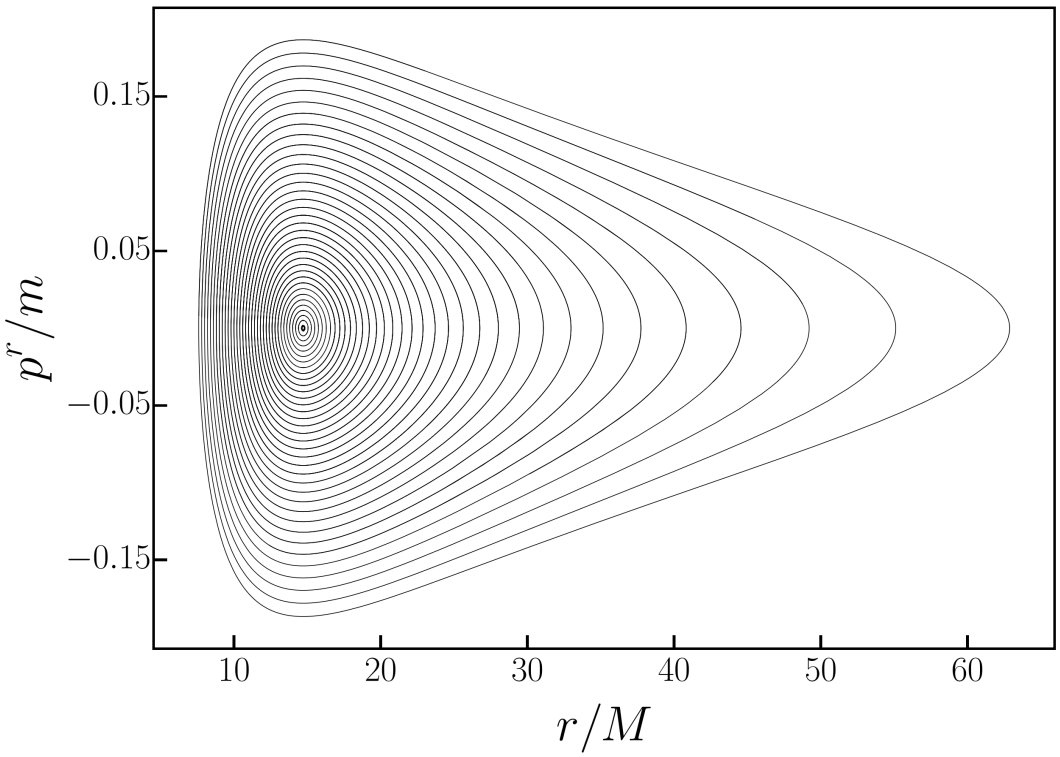

Figure 1.1: The phase portrait of the Schwarzschild solution. Each curve represents a specific energy value conserved along the trajectory. The parameters taken $L = 4.3M$, $r\,[0] \in (7.6M, 14.8M)$ with step $0.2M$ and initial $p^r = 0m$.

One can find in [18] that the obligatory condition of Legendre's transformation from generalised velocities $\dot{\mathbf{q}}$ to canonical momenta $\mathbf{p}$ is the non-singularity of the respective Hessian. In our case, the Hessian is a determinant of a matrix composed of the second derivatives of $\mathcal{L}\left(\mathbf{q}, \dot{\mathbf{q}}, t\right)$ with respect to $\dot{q}^i$. Thus, we need to ensure that condition

$$H\left(\mathcal{L}\right) = \begin{vmatrix} \frac{\partial^2 \mathcal{L}}{\partial \dot{q}^1 \dot{q}^1} & \cdots & \frac{\partial^2 \mathcal{L}}{\partial \dot{q}^n \dot{q}^1} \\ \cdots & \cdots & \cdots \\ \frac{\partial^2 \mathcal{L}}{\partial \dot{q}^1 \dot{q}^n} & \cdots & \frac{\partial^2 \mathcal{L}}{\partial \dot{q}^n \dot{q}^n} \end{vmatrix} \neq 0 \tag{1.30}$$

is fulfilled before we proceed.

Following the general scheme of Legendre's transformation of Lagrangian mechanics (as described in detail in Ref. [19]), we advance in three steps. Firstly, we introduce the new function, which is denoted by $\mathscr{H}$ and called the "total energy":

$$\mathscr{H}\left(\mathbf{q}, \dot{\mathbf{q}}, t\right) = \dot{q}^i p_i\left(\mathbf{q}, \dot{\mathbf{q}}, t\right) - \mathcal{L}\left(\mathbf{q}, \dot{\mathbf{q}}, t\right). \tag{1.31}$$

Secondly, we express the new function (1.31) in terms of the canonical momenta p_i by solving the equation (1.29) for $\dot{q}^i$ and substituting it back into Eq. (1.31). Thus, we obtain a function

$$\mathcal{H}\left(\mathbf{q}, \mathbf{p}, t\right) = \left[\dot{q}^i p_i\left(\mathbf{q}, \dot{\mathbf{q}}, t\right) - \mathcal{L}\left(\mathbf{q}, \dot{\mathbf{q}}, t\right)\right]_{\dot{q}^i \to \dot{q}^i(\mathbf{q}, \mathbf{p}, t)} \tag{1.32}$$

which is referred to as the *Hamiltonian function* of the system.

Just as we started from the Lagrangian function $\mathcal{L}$ and constructed the Hamiltonian function $\mathcal{H}$, we can also, from a known Hamiltonian function $\mathcal{H}$, construct a Lagrangian function $\mathcal{L}$, following the same procedure.

Finally, the last step of the transition to Hamiltonian formalism is assembling a new set of equations of motion from equations (1.15). For a known Hamiltonian $\mathcal{H}$, the equations of motion are called the *Hamilton's canonical equations*:

$$\dot{q}^i = \frac{\partial \mathcal{H}}{\partial p_i}, \qquad \dot{p_i} = -\frac{\partial \mathcal{H}}{\partial q^i}. \tag{1.33}$$

In section 1.4 at page 7, we introduced relativistic Lagrangian for a free particle in curved spacetime. If we take the second form of it (1.28) and perform the described Legendre's transformation, we obtain a relativistic Hamiltonian describing the motion of a free particle in curved spacetime.

The canonical momentum has the form:

$$p_\mu = \frac{\partial \mathscr{L}}{\partial \left(\frac{dx^\mu}{dp}\right)} = 2g_{\mu\nu}\frac{\partial x^\nu}{dp}. \tag{1.34}$$

The second derivatives of $\mathscr{L}$ with respect to $\frac{dx^\mu}{dp}$ form the Hessian, which is equal to the determinant of the metric itself:

$$H\left(\mathscr{L}\right) = \left|g_{\mu\nu}\right|. \tag{1.35}$$

In Ref. [20], one might find that the spacetime (the metric tensor) is non-singular if every half-geodesics is either complete or else contained in a compact set. This particularly means spacetime has no singularity (coordinate or physical). If we restrict ourselves to the region without singularities, we can proceed.

Continuing in the scheme, we first get a total energy function, and then, we substitute the canonical momenta, resulting in the Hamiltonian function:

$$\mathcal{H} = \frac{1}{2}g^{\mu\nu}p_\mu p_\nu. \tag{1.36}$$

It is straightforward to verify that the Hamilton's canonical equations (1.33) for the Hamiltonian (1.36) again reproduce the geodesic equations (1.13). Thus, the Hamiltonian formalism leads to the exact geodesic equations obtained through the Lagrangian formalism.

1.6 Integrals of motion

Consider a pair of arbitrary differentiable functions, denoted as $f\left(q^j, p_j, t\right)$ and $g\left(q^j, p_j, t\right)$, defined on the phase space. We introduce their *Poisson bracket*, which represents a new function on the phase space, expressed as follows:

$$\{f, g\} = \sum_{i=1}^{n}\left(\frac{\partial f}{\partial q^i}\frac{\partial g}{\partial p_i} - \frac{\partial g}{\partial q^i}\frac{\partial f}{\partial p_i}\right). \tag{1.37}$$

Let $\mathcal{I}\left(q^j, p_j, t\right)$ be function on the phase space. Its total time derivative can be expressed as (see Ref. [14]):

$$\frac{d\mathcal{I}}{dt} = \frac{\partial \mathcal{I}}{\partial t} + \{\mathcal{H}, \mathcal{I}\}. \tag{1.38}$$

In the above expression, we have employed the Poisson bracket of the Hamiltonian (1.32) and the function $\mathcal{I}(q^j, p_j, t)$.

Those functions of dynamical variables that remain constant during the system's motion are referred to as *integrals of the motion*. We see from (1.38) that the condition for the quantity $\mathcal{I}(q^j, p_j, t)$ to be an integral of the motion can be written as

$$\frac{\partial \mathcal{I}}{\partial t} + \{\mathcal{H}, \mathcal{I}\} = 0. \tag{1.39}$$

Suppose the integral of the motion is not explicitly dependent on the time. In that case, the above condition simplifies to a vanishing Poisson bracket of Hamiltonian and integral of the motion:

$$\{\mathcal{H}, \mathcal{I}\} = 0. \tag{1.40}$$

The Poisson brackets possess various mathematical properties, among which we highlight just one very useful, known as Jacobi's identity [14]:

$$\{f, \{g, h\}\} + \{g, \{h, f\}\} + \{h, \{f, g\}\} = 0, \tag{1.41}$$

where f, g and h are functions on the phase space. Jacobi's identity leads to Poisson's theorem, which states, that if f and g are two integrals of the motion, their Poisson bracket is likewise an integral of the motion:

$$\{f, g\} = \text{constant}. \tag{1.42}$$

The proof is trivial, as it only requires replacing h in Jacobi's identity (1.41) with $\mathcal{H}$. The particular case is when the constant in (1.42) is identically zero; in such a situation, we say that the integrals are in *involution*.

We can rewrite second Hamilton's equation using the Poisson bracket as follows:

$$\dot{p}_\kappa = -\frac{\partial \mathcal{H}}{\partial q^\kappa} \equiv \{p_\kappa, \mathcal{H}\}. \tag{1.43}$$

Immediately, we can use this knowledge for the relativistic Hamiltonian (1.36) with raised indices and obtain the expression:

$$\{p_\kappa, \mathcal{H}\} = -\frac{\partial \mathcal{H}}{\partial q^\kappa} = -\frac{1}{2} g_{\mu\nu,\kappa} p^\mu p^\nu, \tag{1.44}$$

where we utilised that the canonical momenta are independent of the generalised coordinates; therefore, only the metric tensor will contribute to the derivative with respect to generalised coordinates. This implies that if the metric tensor is independent of a particular generalised coordinate, the conjugate momentum associated with that coordinate is conserved and considered an integral of motion. This observation corresponds with Noether's theorem, which states that symmetries of a system give rise to the existence of integrals of motion. Furthermore, it implies the presence of a Killing vector field in the differential geometry.

In literature linked with general relativity (see, e.g. [10, 13]), the conjugate momentum associated with the time coordinate is denoted $p_t \equiv -E$. It has the meaning of the *total energy*, whereas the conjugate momentum related to the azimuthal angle is denoted $p_\phi \equiv L$ and has the meaning of an *angular momentum*. Both quantities are referenced with respect to an observer standing at infinity.

1.7 Effective potential

This section discusses the effective potential method widely employed to analyse motion in the central force field. This method allows us to distinguish the characteristics of the particle's motion without actually solving equations of motion. This is sometimes advantageous, as solving complicated differential equations may be slow and laborious. To illustrate its applicability, we will examine two fundamental problems, the Kepler problem and the Schwarzschild solution.

1.7.1 Kepler problem

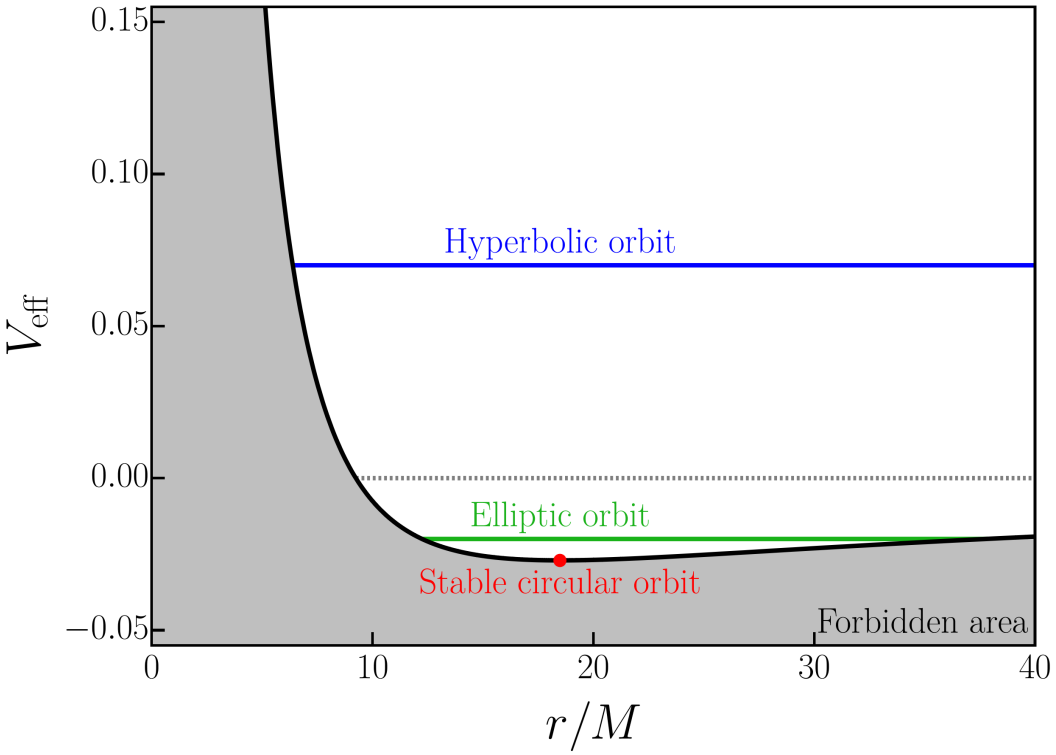

Figure 1.2: The Kepler effective potential and examples of the orbits discussed in the text. The grey dashed line represents the parabolic orbit, a boundary between bound and unbound orbits. The shaded area demonstrates regions where the condition (1.47) is not satisfied. The intersections between a horizontal line representing an energy value and the effective potential curve correspond to turning points, where $\dot{r} = 0$. The parameters are taken $E = 0.98$, $L = 4.3M$. Note that the conventions used for the quantities above are introduced in section 1.7.2

Consider a single particle of reduced mass m that moves around a fixed centre of gravitational force. In this system, the equation of the motion can be expressed in a simple form, as widely known (for more detailed information, see, e.g. [14, 15, 21]):

$$\frac{1}{2}m\dot{r}^2 + \frac{1}{2}\frac{L^2}{mr^2} + V(r) = \text{constant}. \tag{1.45}$$

Here, L denotes total angular momentum and $V(r) = -\frac{mM}{r}$ represents the gravitational potential of the central object with mass M. Equation (1.45) is the

statement of the conservation of total energy. By rearranging equation (1.45) for the derivative of radial distance, we obtain:

$$\begin{aligned} \dot{r}^2 &= \frac{2}{m}\left[E - \left(V(r) + \frac{L^2}{2mr^2}\right)\right] \\ &= \frac{2}{m}\left[E - V_{\text{eff}}(r)\right], \end{aligned} \tag{1.46}$$

where we have introduced a quantity denoted as the *effective potential* $V_{\text{eff}}(r)$. The keystone of this method lies in the fact that the left side of equation (1.46) is the square of the real function, which provides a straightforward condition between the energy and the effective potential:

$$E \geq V_{\text{eff}}(r). \tag{1.47}$$

This condition can be analysed graphically by plotting $V_{\text{eff}}(r)$ and examining where the condition (1.47) holds. As an illustration of this method, the typical shape of the effective potential is shown in Fig. 1.2. As discussed in the cited literature (e.g. [14, 15, 21]), we will briefly distinguish three possible orbits:

- Case $E = E_{\min}$: The total energy equals the minimum value of the effective potential $V_{\text{eff}}(r)$. The orbits are bound and circular ($\dot{r} = \ddot{r} \equiv 0$).
- Case $E \leq 0$: The elliptic orbit remains bounded between the turning points (pericenter, respectively apocenter). An orbit with $E = 0$ is called a parabolic orbit, with its second turning lying theoretically point at infinity, i.e. practically, there is no second turning point.
- Case $E > 0$: The hyperbolic orbit is unbounded. The particle approaches the centre, arrives at the turning point and then moves away towards infinity.

1.7.2 Schwarzschild solution

Here we focus on the Schwarzschild solution, which again involves a single particle of rest mass m, moving around a static, spherically symmetric black hole of mass M. The Schwarzschild line element is given by (for more detailed information, refer to the original work [22] or any elementary relativistic literature, e.g. [10, 13, 16]):

$$ds^2 = -\left(1 - \frac{2M}{r}\right)dt^2 + \frac{dr^2}{1 - \frac{2M}{r}} + r^2\left(d\theta^2 + \sin^2\theta d\phi^2\right). \tag{1.48}$$

We would like to point out that the Schwarzschild metric above describes any spherically symmetric source and is valid anywhere outside this source. Evidently, the metric (1.48) is independent of the coordinates t and the azimuthal angle ϕ. Due to these cyclic coordinates (see section 1.6), the energy E and angular momentum L are conserved. By examining the four-momentum normalisation $g^{\mu\nu}p_\mu p_\nu = -m^2$, and incorporating the integrals of motion, we arrive at the following equation:

$$\begin{aligned} -m^2 &= g^{tt}(p_t)^2 + g^{rr}(p_r)^2 + g^{\theta\theta}(p_\theta)^2 + g^{\phi\phi}(p_\phi)^2 \\ &= \frac{E^2}{g_{tt}} + g_{rr}(p^r)^2 + g_{\theta\theta}\left(p^\theta\right)^2 + \frac{L^2}{g_{\phi\phi}}, \end{aligned} \tag{1.49}$$

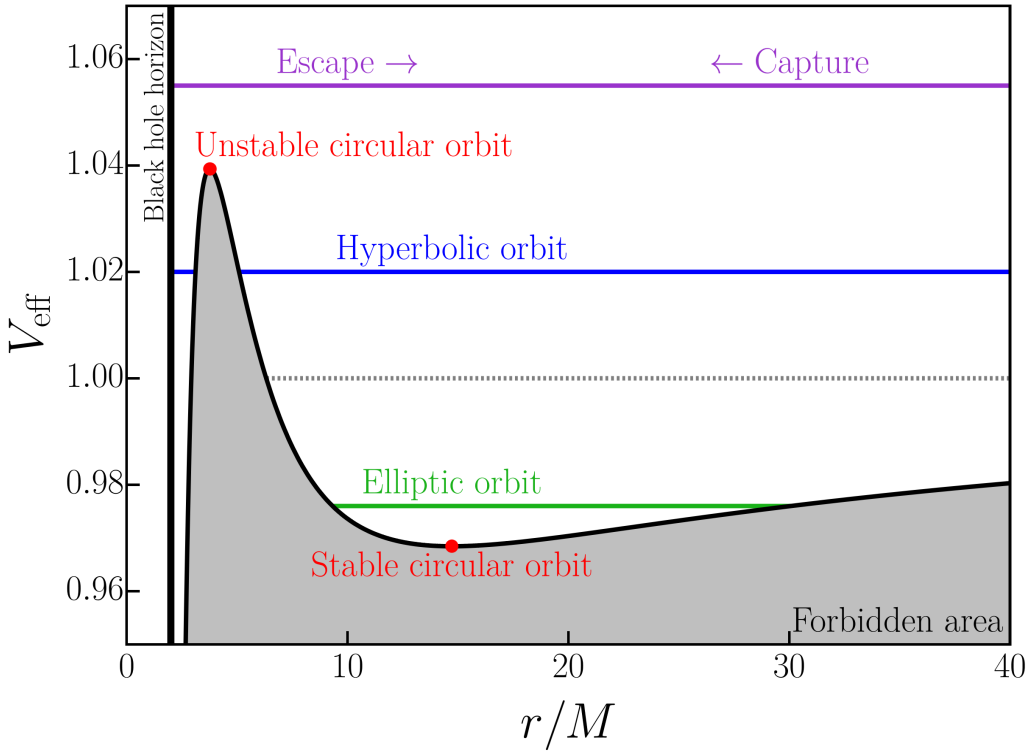

Figure 1.3: The Schwarzshild effective potential and examples of the orbits discussed in the text. The grey dashed line represents the parabolic orbit, a boundary between bound and unbound orbits. The shaded area demonstrates regions where the condition (1.52) is not satisfied. The intersections between the horizontal lines corresponding to a value of the specific energy and the effective potential curve indicate turning points, where $u^r = 0$. The parameters are taken $E = 0.98$, $L = 4.3M$.

where we have employed $g^{\mu\nu} = 1/g_{\mu\nu}$ because of the diagonality of the metric. Moreover, since the motion is planar ($\theta = \text{constant.} \equiv \pi/2$, thus $p^\theta \equiv 0$), equation (1.49) is further simplified. By rearranging the equation (1.49) for the radial component of the four-momentum p_r we obtain:

$$\begin{aligned}(p^r)^2 &= \frac{E^2}{-g_{tt}g_{rr}} - \frac{1}{g_{rr}}\left(m^2 + \frac{L^2}{g_{\phi\phi}}\right) \\ &= E^2 - \left(1 - \frac{2M}{r}\right)\left(m^2 + \frac{L^2}{r^2}\right).\end{aligned} \tag{1.50}$$

Assuming particles with non-zero mass, we can divide the entire equation (1.50) by m^2 to obtain the final form:

$$\begin{aligned}(u^r)^2 &= \widetilde{E}^2 - \left(1 - \frac{2M}{r}\right)\left(1 + \frac{\widetilde{L}^2}{r^2}\right) \\ &= \widetilde{E}^2 - V_{\text{eff}}^2(r),\end{aligned} \tag{1.51}$$

where $\widetilde{E} := E/m$, $\widetilde{L} := L/m$ are the specific energy and angular momentum respectively. In equation (1.51), we have formally introduced the *relativistic effective potential* $V_{\text{eff}}(r)$ (per unit of rest mass m). The condition where the

particle is allowed to move, similar to one in the Kepler problem (1.47), is given by the relation

$$\widetilde{E}^2 \geq V_{\text{eff}}^2(r) \tag{1.52}$$

and can be again analysed graphically by plotting $V_{\text{eff}}(r)$ and examining where the condition (1.52) holds.

A typical shape of the effective potential is shown in Fig. 1.3. In analogy to Kepler problem, we classify possible orbits in the Schwarzschild field:

- Case $\widetilde{E} > \widetilde{E}_{\text{max}}$: The total energy is greater than the maximum of the effective potential $V_{\text{eff}}(r)$. These trajectories have no turning points since they nowhere hit the effective potential. Along such unbound trajectories, the particle either arrives from infinity and plunges to the centre or, on the contrary, it starts from some radius larger than the black hole horizon and escapes to infinity. These trajectories do not exist in the Kepler problem because the Keplerian effective potential diverges to infinity as r approaches zero (for $L \neq 0$), making it impossible to overflown the potential and reach the centre with finite energy.

- Case $\widetilde{E} = \widetilde{E}_{\text{max}}$: The total energy is equal to the maximum of the effective potential $V_{\text{eff}}(r)$. The orbits are circular ($\dot{r} = \ddot{r} \equiv 0$), but they are unstable. Depending on the value of the maximum ($\widetilde{E}_{\text{max}} < 1$ or $\widetilde{E}_{\text{max}} > 1$), these orbits can be either bound or unbound, if they are slightly shifted from bounded circular orbit by perturbation. Such trajectories also do not exist in the Kepler problem since the Keplerian effective potential does not have a local maximum.

- Case $\widetilde{E}_{\text{max}} > \widetilde{E} > 1$: The total energy is below the maximum of the effective potential but is greater than the rest energy. In addition, they also include trajectories with $\widetilde{E} < 1$ entirely lying below the radius corresponding to $\widetilde{E}_{\text{max}}$. These are unbound trajectories analogous to hyperbolic orbits in the Kepler problem. The particle either approaches the centre, arrives at the turning point and then moves away towards infinity, or, on the contrary, they travel outwards from the centre, stops at its turning point, and falls back.

- Case $\widetilde{E}_{\text{min}} < \widetilde{E} \leq 1$: The total energy is below the rest energy, but greater than $\widetilde{E}_{\text{min}}$. Concurrent, their radius is greater than the radius corresponding to $\widetilde{E}_{\text{max}}$. These bounded trajectories are the counterparts of the Keplerian elliptical orbits. The counterpart of the Keplerian parabolic orbit corresponds to $\widetilde{E} = 1$.

- Case $\widetilde{E} = \widetilde{E}_{\text{min}}$: The total energy is equal to a local minimum of the effective potential $V_{\text{eff}}(r)$. The orbits are circular ($\dot{r} = \ddot{r} \equiv 0$) and stable.

In summary, the Schwarzschild solution encompasses various trajectories, some of which are not present in the Kepler problem.

The effective potential method holds for this thesis significant importance in identifying the bounded trajectories as only they may exhibit chaotic behaviour. Acquiring knowledge about the specific range of r, where these trajectories exist, is essential, as it allows more efficient integration of the equations of the motion.

Although discussing the previous two systems may seem redundant, we believe it essential to do so. Kepler problem represents a fundamental problem in classical mechanics, while the Schwarzschild solution, which we subsequently perturb, serves as its counterpart in general relativity. Understanding the traits of these problems is significant for comprehending the overarching concepts presented in this thesis.

1.8 Canonical transformations

For a system described by a Lagrangian $\mathcal{L}(\mathbf{q}, \dot{\mathbf{q}}, t)$ or Hamiltonian $\mathcal{H}(\mathbf{q}, \mathbf{p}, t)$ function, it is often advantageous, due to reasons such as symmetry of the system, to introduce a new set of coordinates, which allow the equations of the motion to become simpler or even trivial.

The choice of the generalised coordinates in Lagrange's formalism has no restriction; thus, the formal structure of Lagrange's equations (1.15) remains uniform regardless of this choice. Consequently, the equations of the motion remain invariant under a given transformation from one set of generalised coordinates to any other set of independent quantities, denoted by:

$$Q^i = Q^i(\mathbf{q}, t). \tag{1.53}$$

Since Lagrange's equations are unaffected by Legendre's transformation (see section 1.5), Hamilton's equations (1.33) also remain unchanged under coordinates transformation. However, in the Hamiltonian formalism, the canonical momenta are treated as independent variables on the same level as the generalised coordinates. Therefore, the range of permissible transformations must be extended to include the simultaneous transformation of the set of independent coordinates q^i and momenta p_i to a new set Q^i and P_i, respectively, with invertible equations of transformation:

$$Q^i = Q^i(\mathbf{p}, \mathbf{q}, t), \qquad P_i = P_i(\mathbf{p}, \mathbf{q}, t). \tag{1.54}$$

Thus, the new coordinates are defined not only in terms of the original coordinates but also in terms of the original momenta.

The equations of motion cannot maintain their canonical form under arbitrary transformations of the type (1.54). Hence, it becomes necessary to derive the conditions that must be satisfied in order for the new coordinates $\mathbf{Q}$ and $\mathbf{P}$ to form the Hamiltonian $\mathcal{H}'(\mathbf{Q}, \mathbf{P}, t)$, which also obey the canonical equations (1.33). These particular transformations are denoted as *canonical transformations*.

Definition 1 (Canonical transformation [23])**.** *A transformation* $(\mathbf{q}, \mathbf{p}) \to (\mathbf{Q}, \mathbf{P})$ *defined by equations* (1.54) *is a canonical transformation if and only if the Poisson brackets are invariant, i.e., if the three equalities*

$$\{Q^i, P_j\}_{\mathbf{q},\mathbf{p}} = \delta^i_j, \qquad \{Q^i, Q^j\}_{\mathbf{q},\mathbf{p}} = \{P_i, P_j\}_{\mathbf{q},\mathbf{p}} = 0 \tag{1.55}$$

are satisfied for all $i, j = 0, ..., n$*, where the Poisson brackets in equation* (1.55) *are those defined in equation* (1.37) *with* f *and* g *replaced by the various* Q^i *and* P_i *coordinates.*

In the aforementioned definition, we had to employ subscripts for the Poisson brackets denoting the coordinates for which the brackets are defined. The proof of this theorem can be found in references such as [15]. It should be noted that if the transformation is canonical, its inverse transformation is also canonical. The definition 1 is one of several equivalent definitions of canonical transformations (e.g. symplectic condition exists, for more details, see, e.g. [23]).

With the established conditions for canonical transformation, we are able to proceed further and determine a transformation to a set of variables where the Hamiltonian is $\mathcal{H}'(\mathbf{Q},\mathbf{P}) \equiv 0$, resulting in trivial motion; consequently determined solely by $2n$ integration constants. This leads us to the Hamilton-Jacobi theory.

1.8.1 Hamilton-Jacobi theory

In the equation (1.14), we defined the action as the integral of the Lagrangian. In section 1.5, we introduced Legendre's transformation, enabling us to transition from Lagrangian to Hamiltonian formalism. Taking advantage of this, we express the action integral (1.14) once again, but in terms of the Hamiltonian formalism:

$$\mathcal{S} = \int_{t_1}^{t_2} \left(p_i \frac{dq^i}{dt} - \mathcal{H}(\mathbf{q},\mathbf{p},t) \right) dt. \tag{1.56}$$

By applying the principle of least action, we vary $\mathcal{S}$ with respect to the independent variables $\mathbf{q}$ and $\mathbf{p}$; we once more obtain the Hamilton's equations (1.33). Under canonical transformations, the form of the equations (1.33) remains unchanged (by definition), thus necessitating the invariance of the principle of least action under canonical transformation as well.

The simultaneous validity of equation (1.56) for the old Hamiltonian function $\mathcal{H}(\mathbf{q},\mathbf{p})$ and the new one $\mathcal{H}'(\mathbf{Q},\mathbf{P})$ leads to the equality:

$$\delta \int_{t_1}^{t_2} \left(p_i \frac{dq^i}{dt} - \mathcal{H}(\mathbf{q},\mathbf{p},t) \right) dt = \delta \int_{t_1}^{t_2} \left(P_i \frac{dQ^i}{dt} - \mathcal{H}'(\mathbf{Q},\mathbf{P},t) \right) dt. \tag{1.57}$$

Therefore, the integrands must be equal apart from the total time differential of the arbitrary function F on the phase space (with continuous second derivatives):

$$p_i dq^i - \mathcal{H}(\mathbf{q},\mathbf{p},t)\, dt = P_i dQ^i - \mathcal{H}'(\mathbf{Q},\mathbf{P},t)\, dt + dF. \tag{1.58}$$

The function F can be added since the total time differential does not prevail in the action variation and hence does not affect the equations of motion (e.g., see [21]). Here we explicitly exclude the scale transformation, which only leads to the multiplication of one side of equation (1.58) by an arbitrary constant, which is insignificant for our purposes (details can be found in [15]). The function F is commonly referred to as the *generating function* (of a canonical transformation). It may depend on one of the old phase space variables $(\mathbf{q},\mathbf{p})$ and one of the new phase space variables $(\mathbf{Q},\mathbf{P})$.

In *Hamilton-Jacobi theory*, our goal is to find such a transformation to a set of variables where the Hamiltonian is $\mathcal{H}'(\mathbf{Q},\mathbf{P},t) \equiv 0$. In this case, the Hamilton's equations become trivial, as all the derivatives of the Hamiltonian vanish:

$$\frac{dP_i}{dt} = 0 = \frac{dQ^i}{dt}. \tag{1.59}$$

Therefore the new generalised coordinates $\mathbf{Q}$ and momenta $\mathbf{P}$ become constants of motion. Additionally, we assume that the generating function is given as a function of the old and new coordinates and time: $F = F(\mathbf{q}, \mathbf{Q}, t)$. Under these conditions, equation (1.58) can be rearranged as follows:

$$\begin{aligned} dF(\mathbf{q}, \mathbf{Q}, t) &= \frac{\partial F}{\partial q^i} dq^i + \frac{\partial F}{\partial Q^i} dQ^i + \frac{\partial F}{\partial t} dt \\ &= p_i dq^i - P_i dQ^i - \mathcal{H}(\mathbf{q}, \mathbf{p}, t)\, dt. \end{aligned} \tag{1.60}$$

Consequently, the generating function $F(\mathbf{q}, \mathbf{Q}, t)$ satisfies, term by term:

$$\frac{\partial F}{\partial q^i} = p_i, \qquad \frac{\partial F}{\partial Q^i} = -P_i, \qquad \frac{\partial F}{\partial t} + \mathcal{H}(\mathbf{q}, \mathbf{p}, t) = 0. \tag{1.61}$$

Combining these equations yields the Hamilton-Jacobi equation, expressed as:

$$\frac{\partial F}{\partial t}\left(\mathbf{q}, \mathbf{Q}, t\right) + \mathcal{H}\left(\mathbf{q}, \frac{\partial F}{\partial \mathbf{q}}, t\right) = 0. \tag{1.62}$$

We emphasise that the generalised coordinate is a function of old generalised coordinates and time: $\mathbf{Q} = \mathbf{Q}\left(\mathbf{q}, \frac{\partial F}{\partial \mathbf{q}}, t\right)$. Therefore the Hamilton-Jacobi equation (1.62) is a single, first-order nonlinear partial differential equation in $(n+1)$ variables $(q^1, ..., q^n; t)$, for the generating function $F(\mathbf{q}, \mathbf{Q}, t)$.

It is conventional to denote the solution $F(\mathbf{q}, \mathbf{Q}, t)$ of equation (1.62) by $S(\mathbf{q}, t)$ and call it *Hamilton's principal function*. Remarkably, when the $2n$ constant parameters $\mathbf{Q}$ and $\mathbf{P}$ are identified with the initial values $\mathbf{Q} = \mathbf{q}(t_1)$, $\mathbf{P} = \mathbf{p}(t_1)$, the Hamilton's principal function $S(\mathbf{q}, t)$ is equal to the classical action $\mathcal{S}(\mathbf{q}, t)$ defined by equation (1.14) [14, 24].

Similar to Lagrange's equations (1.15) and Hamilton's equations (1.33), the Hamilton-Jacobi equation (1.62) serves as the basis of a general method of integrating the equations of motion.

1.9 Integrability of the Hamiltonian systems

In accordance with the Hamilton-Jacobi theory, we proceed from solving the system of $2n$ ordinary differential equations (1.33) to the single partial differential equation (1.62). Solving partial differential equations can be notoriously complicated, which can sometimes hinder the effectiveness of the Hamilton-Jacobi theory. Nevertheless, under certain conditions, separating the variables in the Hamilton-Jacobi equation (1.62) becomes possible, consequent in a solution reducible to integration alone.

The complete integral of the Hamilton-Jacobi equation (1.62) must contain $n+1$ arbitrary integration constants. Since the Hamilton's principal function $S(\mathbf{q}, t)$ appears in the equation (1.62) solely through its derivatives, one of these constants is additive (as precisely described in [14]). Thus, a complete solution takes the form:

$$S = s(\mathbf{q}; \alpha_1, ..., \alpha_n; t) + A, \tag{1.63}$$

where α_i and A represent arbitrary constants. The additive constant A may be omitted as it holds no importance in the Hamilton's principal function. According

to [14, 15], if all coordinates in the Hamilton-Jacobi equation (1.62) appear only in some combination $(q^i, \partial S/\partial q^i)$, which does not involve the other coordinates or time (i.e. the coordinates are separable) then the function in form (1.63) is completely separable and can be rewritten in the following form:

$$S = \sum_i S_i\Big(q^i; \alpha_1, ..., \alpha_n\Big) - E\Big(\alpha_1, ..., \alpha_n\Big)t, \tag{1.64}$$

where each of the functions S_i depends solely on one coordinate q^i.

When a Hamiltonian system, characterised by n degrees of freedom, exhibits complete separability, it implies it has n independent conserved quantities. However, in order to reveal this separability, it is necessary to select appropriate canonical variables. Consequently, two fundamental theorems regarding the integrability of the Hamiltonian systems and the definition of action-angle variables come into play.

Theorem 1 (Liouville's theorem on integrability [21])**.** *Let us consider a Hamiltonian system with n degrees of freedom, described by $2n$ generalised coordinates (q^i, p_i). If there exist n functions $\mathcal{I}$ (on a subset $\mathcal{U}$ of the phase space), satisfying the following properties (without loss of generality $\mathcal{I}_1 = \mathcal{H}$):*

- *$\{\mathcal{I}_i, \mathcal{H}\} = 0, i = 2, ..., n$; indicating that the quantities $\mathcal{I}_i$ are conserved;*
- *$\{\mathcal{I}_i, \mathcal{I}_j\} = 0, i, j = 1, ..., n$; indicating that the functions $\mathcal{I}_i$ are in involution;*
- *The total differentials $d\mathcal{I}_i = \Big(\partial\mathcal{I}_i/\partial q^k\Big)\, dq^k + (\partial\mathcal{I}_i/\partial p_k)\, dp_k$ are linearly independent;*

then the system is integrable (on the subset $\mathcal{U}$); thus in principle the analytical solution of the Hamilton's equations (1.33) *can be obtained through integration.*

The proof of this theorem can be found in [25], where one can also find another theorem on integrability, further developing Liouville's theorem and introducing the canonical transformation to *action-angle variables*.

Theorem 2 (Liouville-Arnold theorem [25])**.** *Let us consider a Hamiltonian system with n degrees of freedom to be integrable, possessing independent, involutive integrals of motion $\mathcal{H}, \mathcal{I}_2, ..., \mathcal{I}_n$. For a fixed $\mathbf{f} \in \mathbb{R}^n$, we set*

$$\mathcal{M}_f = \{x : \mathcal{I}_i(x) = f_i, i = 1, ..., n\}.$$

Then

- *$\mathcal{M}_f$ is a smooth manifold, invariant under the phase flow governed by the Hamiltonian function $\mathcal{H}$.*
- *If the manifold $\mathcal{M}_f$ is compact and connected, then it is diffeomorphic to an n-dimensional torus*
$$\mathbb{T}^n = S^1 \times ... \times S^1.$$
- *If the manifold $\mathcal{M}_f$ is compact and connected, then locally, there exists a canonical coordinate transformation $(\mathbf{q}, \mathbf{p}) \to (\boldsymbol{\theta}, \boldsymbol{\mathcal{I}})$ to a new coordinate system, referred to as the action-angle coordinates, such that the angles $\{\theta_i\}_{i=1}^n$*

serves as coordinates on $\mathbb{T}^n$; the action $\{\mathcal{I}_i\}_{i=1}^n$ are integrals of motion and $\mathcal{H}(\mathbf{q},\mathbf{p}) = \mathcal{H}'(\mathcal{I})$ does not depend on $\boldsymbol{\theta}$ [21]. In particular, the Hamilton's equations are given by

$$\dot{\mathcal{I}} = 0, \qquad \dot{\theta} = \frac{\partial \mathcal{H}'}{\partial \mathcal{I}} \equiv \omega(\mathcal{I}). \tag{1.65}$$

Once all the integrals $\boldsymbol{\mathcal{I}}$ of motion are specified, both the torus on which the motion occurs as well as the *fundamental frequencies* of motion $\omega(\mathcal{I})$ are determined. By varying $\boldsymbol{\mathcal{I}}$, we can explore the phase space $T^*\mathcal{Q}$ on a foliation of tori. Fig. 1.4 shows a trajectory of a system of two degrees of freedom on a torus $\mathbb{T}^2$, with highlighted particular actions $\boldsymbol{\mathcal{I}}$ and angles $\boldsymbol{\theta}$. It is evident that the solution to equations (1.65) results in a spiral-shaped curve on the surface of a torus (the blue trajectory in Fig. 1.4).

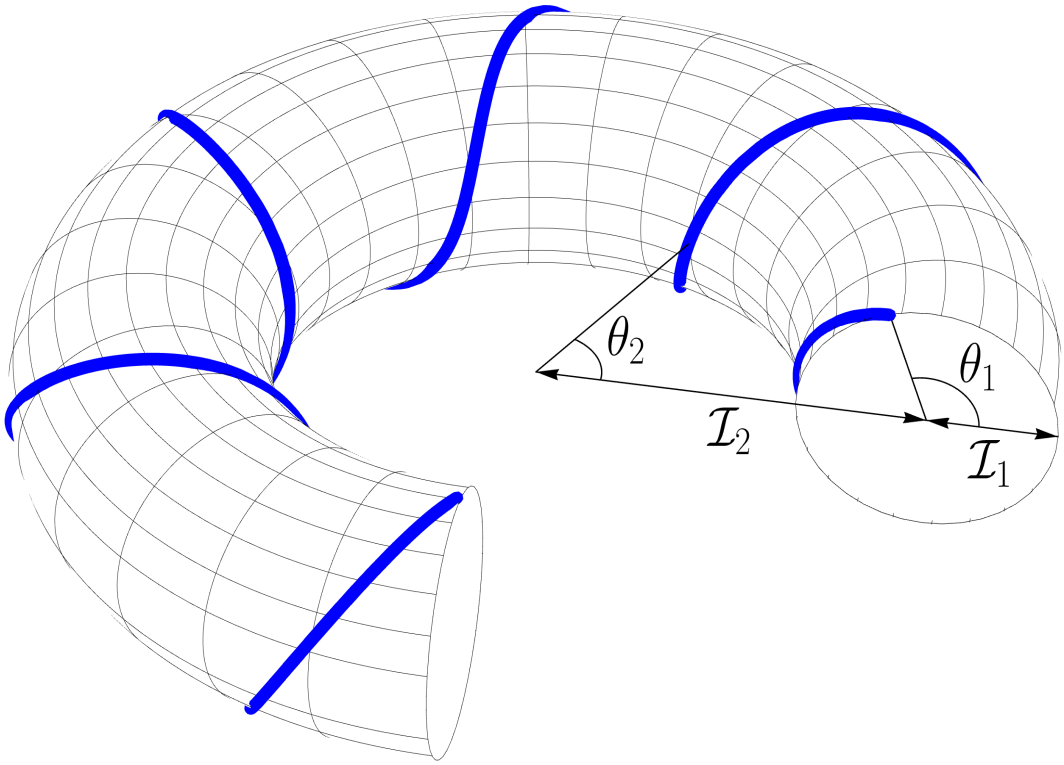

Figure 1.4: A trajectory on a torus of a two degrees of freedom system.

The nature of the motion on the torus relies on whether any of the fundamental frequencies are related by an integer ratio. This condition referred to as *resonance condition* and discussed in [8], establishes that the character of the motion on the torus depends on the existence of linearly independent integer-vectors $\mathbf{k}$ that satisfy the following equation:

$$\mathbf{k}\cdot\boldsymbol{\omega} \equiv \sum_{i=1}^{n} k_i\omega^i = 0, \text{ where } k_i \in \mathbb{Z} \text{ and } |\mathbf{k}| \equiv \sum_{k=1}^{n} |k_i| \neq 0. \tag{1.66}$$

If there are no such $\mathbf{k}$ that satisfy the condition (1.66), the motion on the torus $\mathbb{T}^n$ is classified as quasiperiodic. In this case, the quasiperiodic orbit densely covers the torus $\mathbb{T}^n$ over an infinite amount of time and does not return to its

initial state from where it started within a finite period. Furthermore, this particular orbit is considered ergodic, indicating that a phase space average across the torus can be used instead of an infinite-time average on the phase space function along the motion.

If there are less than $m < n-1$ independent resonant conditions fulfilled, the quasiperiodic orbit will only densely cover a $\mathbb{T}^{n-m}$ torus, which is a submanifold of the corresponding $\mathbb{T}^n$ torus. On the other hand, if there are $n-1$ resonant conditions, the motion turns periodic.

Fig. 1.5 depicts an example of a two degrees of freedom system's resonant and three examples of non-resonant phase space trajectories on a torus $\mathbb{T}^2$ with various ratios of fundamental frequencies.

1.10 Discrete and continuous systems

A dynamical system is characterised by the evolution of one or more state variables across time, where the current state dictates all future states. We can distinguish between discrete or continuous dynamical systems depending on the nature of the time variable. Throughout the remainder of the thesis, we will focus solely on Hamiltonian systems. Therefore, we restrict the dynamical systems to the Hamiltonian ones.

Formally, a *continuous dynamical system* is defined by a set of differential equations:

$$\frac{d\mathbf{x}}{dt} = \mathbf{f}\left(\mathbf{x}, t\right). \tag{1.67}$$

In equation (1.67), $\mathbf{x}$ represents a vector from the phase space $T^*\mathcal{Q}$, $\mathbf{f}\left(\mathbf{x}, t\right)$ is a vector function defined on phase space and $t \in \mathbb{R}$ is a continuous parameter that commonly associated with time.

On the other hand, analogous to equation (1.67), we can introduce a set of differential equations

$$\mathbf{x}_{n+1} = \mathbf{F}\left(\mathbf{x}_n, n\right), \tag{1.68}$$

which defines a *discrete mapping*. Likewise, in previous definition, $\mathbf{x}_n$ and $\mathbf{x}_{n+1}$ are vectors from the phase space $T^*\mathcal{Q}$, $\mathbf{F}\left(\mathbf{x}_n, n\right)$ is a vector function on the phase space and $n \in \mathbb{N}$ is a discrete parameter.

In continuous dynamical systems, the equations of motion give rise to a flow in a phase space $\mathcal{F}_t : T^*\mathcal{Q} \to T^*\mathcal{Q}$ along which an initial condition $\mathbf{x}_0$ evolves to $\mathbf{x}$ over time, i.e. $\mathbf{x}\left(t\right) = \mathcal{F}_t\left(\mathbf{x}_0\right)$. If there is a volume element on $T^*\mathcal{Q}$ such that the size of any volume of initial conditions along the flow remains constant, the system is referred to as conservative. In particular, for Hamiltonian systems, this is well known as Liouville's theorem:

Theorem 3 (Liouville's theorem [21])**.** *For a time evolution of a closed Hamiltonian system described by the flow in the phase space* $\mathbf{x}\left(t\right) = \mathcal{F}_t\left(\mathbf{x}_0\right)$*, Liouville's theorem states that an arbitrary volume of the region in phase space remains constant as it evolves.*

Consequently, the Hamiltonian systems are conservative. The proof of Liouville's theorem can be found in Ref. [21]. The remarkable feature of the above

theorem is that the flow in the phase space can be treated as canonical transformation [14]. Thus, the arbitrary volume of the phase space $T^*\mathcal{Q}$ is invariant under canonical transformation.

If the vector function $\mathbf{f}(\mathbf{x}, t)$ in equation (1.67) does not explicitly depend on time, then the system is considered autonomous. Specifically for Hamiltonian systems, this implies $\partial\mathcal{H}/\partial t = 0$, which in connection to the equation (1.38), yields $d\mathcal{H}/dt = 0$ since $\{\mathcal{H}, \mathcal{H}\} \equiv 0$ (by the definition of the Poisson bracket). Thus, the autonomous Hamiltonian systems have the Hamiltonian as the integral of the motion, reflecting the system's total energy conservation.

1.11 Poincaré surface of section

In the domain of general relativity, the studied dynamical systems are continuous. However, these continuous systems can be discretised, allowing them to be represented by discrete mappings.

The subsequent sections of this thesis will focus on Hamiltonian systems of two degrees of freedom. Therefore, let us glance at the visualisation of 4-dimensional phase space foliation by the $\mathbb{T}^2$ tori. Such a dynamical system possesses two integrals of motion (without loss of generality $\mathcal{I}_1 = \mathcal{H}$). By confining ourselves to a hypersurface, where one of the integrals of motion remains fixed, we are left with a 3-dimensional space filled with 2-dimensional tori. Additionally, we can select a section within this space that intersects the Hamiltonian flow perpendicularly, i.e. cuts transversally through the tori (for more information, see Ref. [8]). This selected section enables us to examine the foliation (an example is shown in Fig. 1.5). This surface is commonly known as the *Poincaré surface of section*, which corresponds to a discrete mapping called Poincaré mapping described by an equation (1.68), because every successive point is determined by the preceding one.

To computationally create a Poincaré section, one must integrate the equations of motion and identify the constant of the motion that remains fixed, as well as the section condition that reflects the symmetries of the system. Only two remaining phase-space coordinates are recorded once the trajectory passes through this section surface. After a sufficient number of crossings have been recorded, the results can be plotted.

In the case of an integrable system, the torus is densely populated with a quasiperiodic trajectory, and the set of points derived from it will progressively trace out a single closed curve on the plot. This particular curve is referred to as an *invariant curve* since, on a Poincaré surface of section, the curve is mapped to itself. When several independent trajectories are used, the foliation is revealed as a sequence of nested, non-intersecting closed curves. Conversely, trajectories that meet a resonant condition occupy just a subspace of the torus and manifest as a finite set of periodically repeated points on the section. For each resonance, the number of these sets is infinite. However, each set is made up of a finite number of points equal to the periodicity of the resonance, which represents the number of mappings required for a periodic orbit to return to its initial conditions).

Poincaré surfaces of section provide valuable insights into the dynamics of Hamiltonian systems. They enable us to visualise and analyse the behaviour of trajectories in a phase space. These surfaces of section are a powerful tool in

studying the complex and rich dynamics of dynamical systems.

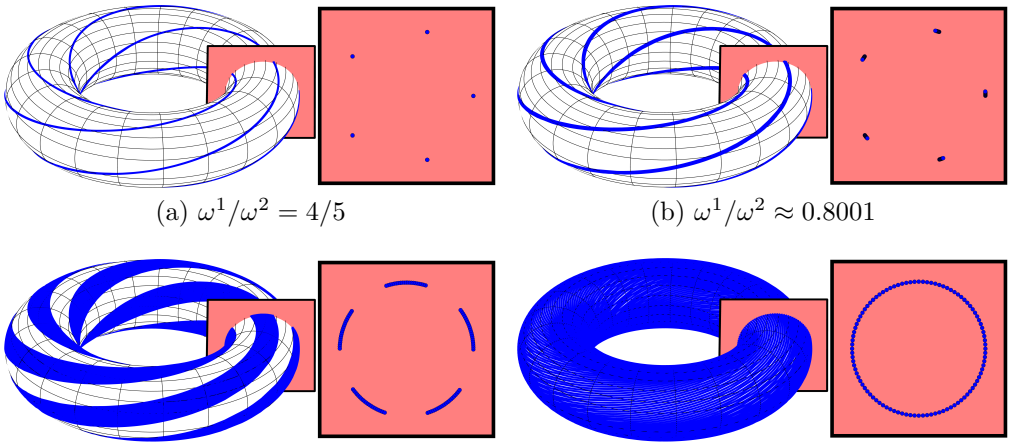

(a) $\omega^1/\omega^2 = 4/5$ (b) $\omega^1/\omega^2 \approx 0.8001$

(c) $\omega^1/\omega^2 \approx 0.801$ (d) $\omega^1/\omega^2 \approx 0.81$

Figure 1.5: An illustration of a resonant (a) torus and three quasiperiodic ones (b,c,d) in a two degree of freedom system. The trajectories on the tori are depicted in blue, while the Poincaré surfaces of section are in red. Each trajectory undergoes calculations until the motion intersects the Poincaré surface of section for a total of 100 occurrences. The resonant trajectory, located in the upper left plot, exhibits a resonant ratio expressed as $\omega^1/\omega^2 = 4/5$, representing the fundamental frequency of the small circle over the large circle. In contrast, the remaining trajectories represent non-resonant trajectories, characterised by ratios that deviate from the resonant ratio and are of an irrational nature. Over time, the non-resonant trajectories asymptotically trace out the torus cross-section.

1.12 Transition to non-integrability

Let us consider an integrable system that undergoes perturbation, causing it to lose its integrability, enabling chaos to occur. To analyse the trajectory changes caused by perturbation, we must establish a correspondence between parts of the phase space in the perturbed system and their counterparts in the unperturbed system, for which it is suitable to use the action-angle framework. The transition from integrable systems to non-integrable ones is governed by two fundamental theorems: the Kolmogorov-Arnold-Moser theorem (abbreviated as the KAM theorem, for detailed references see the original papers [26, 27, 28]) and the Poincaré-Birkhoff theorem (for detailed references see the original papers [29, 30]).

Consider the Hamiltonian $\mathcal{H}_0(\mathbf{q}, \mathbf{p})$ of an autonomous integrable system that must be solved. We perturb this system with the additional term $\epsilon\mathcal{H}_1$, where ϵ is sufficiently small, i.e. $\epsilon \ll 1$. The perturbed system's resultant Hamiltonian is given by:

$$\mathcal{H}(\mathbf{q}, \mathbf{p}) = \mathcal{H}_0(\mathbf{q}, \mathbf{p}) + \epsilon\mathcal{H}_1(\mathbf{q}, \mathbf{p}). \tag{1.69}$$

In the next step, we transform the coordinates of this Hamiltonian from $(\mathbf{q}, \mathbf{p})$ to action-angles variables $(\boldsymbol{\theta}, \boldsymbol{\mathcal{I}})$. In particular, if this transformation yields the following expression for the Hamiltonian:

$$\mathcal{H}(\boldsymbol{\theta}, \boldsymbol{\mathcal{I}}) = \mathcal{H}_0(\boldsymbol{\mathcal{I}}) + \epsilon\mathcal{H}_1(\boldsymbol{\theta}, \boldsymbol{\mathcal{I}}), \tag{1.70}$$

we call such a Hamiltonian system quasi-integrable [31] or nearly integrable.

Theorem 4 (KAM theory [21]). *If the fundamental frequencies $\omega_{0,i}$ on a torus in an unperturbed system $\mathcal{H}_0$ are sufficiently non-resonant, then there exists also in the system $\mathcal{H} = \mathcal{H}_0 + \epsilon\mathcal{H}_1$ at small, but finite values of ϵ a distorted torus (referred to as KAM torus), which for $\epsilon \to 0$ turns into the torus of the unperturbed system $\mathcal{H}_0$.*

To quantify the notion of "sufficiently non-resonant", we introduce a Diophantine condition [8]. This condition necessitates the presence of $K(\epsilon) \lesssim \mathcal{O}(\sqrt{\epsilon})$ and an integer $d > n-1$ such that the set of tori satisfying the Diophantine condition:

$$\left| \sum_{i=1}^{n} k_i \omega^i \right| > \frac{K(\epsilon)}{|k|^d} \tag{1.71}$$

is sufficiently non-resonant. The Diophantine criterion guarantees that the distorted torus is sufficiently distant from a resonance. However, the condition (1.71) is satisfied only in a fraction of the phase space volume, approximately equal to $1 - \mathcal{O}(\sqrt{\epsilon})$ [8]. As a result, even with little perturbations, the qualitative character of the motion in the system is mostly preserved. However, there is a volume of the phase space $\mathcal{O}(\sqrt{\epsilon})$ around the resonances, where the character of the motion undergoes qualitative changes. That brings us to the second theorem, known as the Poincaré-Birkhoff theorem.

Theorem 5 (Poincaré-Birkhoff theorem [30]). *When an integrable Hamiltonian system $\mathcal{H}_0(\boldsymbol{\mathcal{I}})$ is perturbed, the rational curve with resonant ratio $\omega^1/\omega^2 = r/s$ under a Poincaré mapping is dissolved, and only an even number of periodic points $2\kappa s$ ($\kappa \in \mathbb{N}$) under the perturbation survive. These periodic points alternate between stable and unstable ones forming a chain of resonance points known as the Birkhoff chain.*

1.13 Resonance analysis

Resonances are parts of the phase space where chaotic behaviour emerges. Therefore, having the methods to identify these zones effectively would be advantageous. In systems with two degrees of freedom, we might take advantage of the Poincaré surface of section to evaluate the rotation number ν_ϑ (for further information on the rotation numbers, see Ref. [8, 32]). The rotation number ν_ϑ represents the ratio of the system's two fundamental frequencies, i.e. ω^1/ω^2.

Assuming we have already produced a Poincaré surface of section of the system (an illustration of the following is depicted in Fig. 1.6), we must first distinguish the centre of the main island of stability, represented by a fixed point $\mathbf{x}_s$ on the Poincaré section, around which most invariant curves are nested. Next, we evaluate rotation angle, defined as the angle between two vectors originating from $\mathbf{x}_s$ and pointing towards two consecutive points on the Poincaré surface of section:

$$\vartheta_i := ang\Big[(\mathbf{x}_{i+1} - \mathbf{x}_c)\,;(\mathbf{x}_i - \mathbf{x}_c)\Big]. \tag{1.72}$$

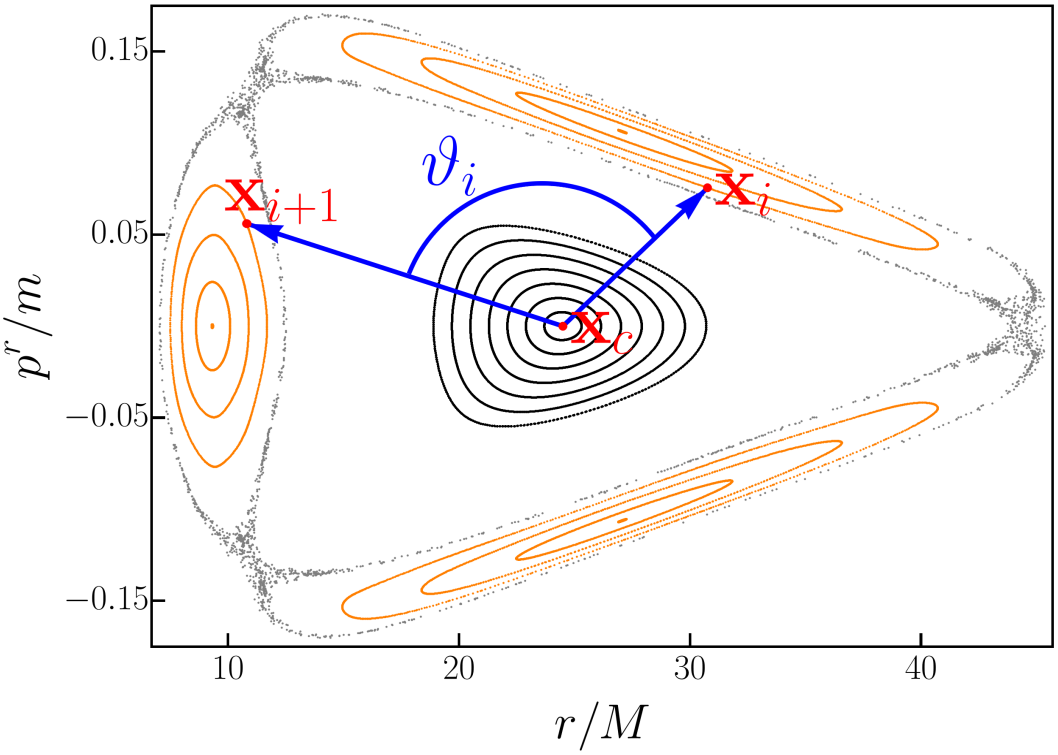

Figure 1.6: An illustration of a two degrees of freedom system's Poincaré surface of section. The central region of the figure shows black invariant curves, representing components of the main island of stability with their centre denoted as x_c. The orange curves are part of 2/3 resonance, wherein centres of islands are stable points of the respective resonance. The grey points illustrate the chaotic layer, where the unstable points of 2/3 resonance are located. On the resonance layer, two consecutive points and their corresponding rotation angle are marked.

To ensure numerical consistency, it is customary to restrict the angle value spectrum to a proper interval so there is no discontinuity [32]. The *rotation number* is then obtained as the average of these rotation angles as follows:

$$\nu_\vartheta = \lim_{N\to\infty} \frac{1}{2\pi N} \sum_{i=1}^{N} \vartheta_i. \tag{1.73}$$

In the limit, $N \to \infty$, the rotation number (1.73) corresponds to the ratio of two fundamental frequencies ω^1/ω^2, presented in section 1.9.

The plot of rotation numbers ν_ϑ as a function of distance from the main island's centre is referred to as a *rotation curve*.

The rotation curve is strictly monotonic for integrable systems as one advances away from the centre $\mathbf{x}_s$. In contrast, for perturbed non-integrable systems, the curve maintains qualitative similarity to the unperturbed one, except in the vicinity of the resonances where it exhibits significant changes. The resonance curve starts to fluctuate randomly in chaotic layers near the resonance. Moreover, within the Birhoff chain, stable regions known as islands of stability appear as plateaus with constant values in the rotation curve.

The *width of a resonance* is a useful measure as it can be related to the perturbation parameter ϵ in the perturbed Hamiltonian introduced in Eq. (1.70).

Let us summarise the relationship between the width of the resonance and the perturbation parameter of two degrees of freedom system, as provided in [8] (further details can also be found in [33, 31]). The Hamiltonian (1.70) can be expressed as:

$$\mathcal{H} = \mathcal{H}_0\left(\mathcal{I}_1, \mathcal{I}_2\right) + \epsilon \mathcal{H}_1\left(\mathcal{I}_1, \mathcal{I}_2, \theta^1, \theta^2\right). \tag{1.74}$$

Considering the unperturbed Hamiltonian system $\mathcal{H}_0$, we assume that there exists a resonance satisfying the resonance condition (1.66) (i.e. $k_1\omega^1 + k_2\omega^2 = 0$) at action coordinates $\mathcal{I}_1 = \mathcal{I}_1^{\text{np}}$ and $\mathcal{I}_2 = \mathcal{I}_2^{\text{np}}$. We perform rotation of the action-angle variables as follows:

$$\widetilde{\mathcal{I}}_1 = \frac{\mathcal{I}_1}{2k_1} + \frac{\mathcal{I}}{2k_2}, \widetilde{\theta}^1 = k_1\theta^1 + k_2\theta^2, \tag{1.75}$$

$$\widetilde{\mathcal{I}}_2 = \frac{\mathcal{I}_1}{2k_1} - \frac{\mathcal{I}}{2k_2}, \widetilde{\theta}^2 = k_1\theta^1 - k_2\theta^2. \tag{1.76}$$

These new variables also maintain canonical properties. In the transformed variables, the resonance condition reduces to $\widetilde{\omega}_1 = 0$. The final form of the Hamiltonian can be written as (the steps leading to this relation can be found in [8]):

$$\mathcal{H} = \frac{\beta}{2}\left(\Delta\widetilde{\mathcal{I}}_1\right)^2 + \epsilon\alpha\cos\left(\kappa\widetilde{\theta}^1\right), \tag{1.77}$$

where κ corresponds to the one discussed in Poincaré-Birkhoff theorem 5 and α, β are positive parameters, while $\Delta\widetilde{\mathcal{I}}_1 = \widetilde{\mathcal{I}}_1 - \widetilde{\mathcal{I}}_1^{\text{np}}$.

Separatrices, which separate the near-resonant Birkhoff chain from the rest of the KAM tori, are approximately located as the level set $\mathcal{H} = \epsilon\alpha$ of the Hamiltonian (1.77), resulting in:

$$\left(\Delta\widetilde{\mathcal{I}}_1|_{\text{sep}}\right)^2 = \frac{2\epsilon\alpha}{\beta}\left(1 - \cos\left(\kappa\widetilde{\theta}^1\right)\right). \tag{1.78}$$

The definition of the width of resonance, which we denote as w, is as the difference between the maximum and the minimum of $\Delta\widetilde{\mathcal{I}}_1$ on the separatrix, which occurs when $\cos\left(\kappa\widetilde{\theta}^1\right) = -1$:

$$w := \max\left(\Delta\widetilde{\mathcal{I}}_1|_{\text{sep}}\right) - \min\left(\Delta\widetilde{\mathcal{I}}_1|_{\text{sep}}\right) = 4\sqrt{\frac{\alpha}{\beta}}\sqrt{\epsilon}. \tag{1.79}$$

Returning to the initial system (1.74) and choosing a Poincaré surface of section on the plane $\theta^2 = 0$, then from (1.75), we obtain $\widetilde{\theta}^1 = k_1\theta^1$ throughout the section. This implies that on the surface of section and at the resonance, a total of $\kappa \cdot k_1$ islands of stability and $\kappa \cdot k_1$ unstable points will emerge.

1.14 Chaos

This thesis is dedicated to the study of dynamical systems which exhibit chaotic behaviour. Chaotic behaviour emerges when an integrable system is perturbed and loses its integrability. A widely accepted definition of chaos has been introduced by Devaney in Ref. [34].

Definition 2 (Topologically transitive [34]). *A mapping $f : \mathcal{J} \to \mathcal{J}$ is considered to be topologically transitive if, for any pair of open sets $U, V \subset \mathcal{J}$, there exists a positive integer $k > 0$ such that $f^k(U) \cap V = \emptyset$.*

In practical terms, this concept states that points of topologically transitive maps move from one arbitrarily small neighbourhood to any other during iterations. As a result, the dynamical systems governed by such maps cannot be decomposed into two disjoint open sets that are invariant under the map.

Definition 3 (Sensitive dependence on initial conditions). *A mapping $f : \mathcal{J} \to \mathcal{J}$ is said to have sensitive dependence on initial conditions if there exists a positive value $\delta > 0$ such that, for any $x \in \mathcal{J}$ and any neighbourhood $\mathcal{N}$ of x, there exists a point $y \in \mathcal{N}$ and a non-negative integer n satisfying*

$$\left| f^n(x) - f^n(y) \right| > \delta.$$

Sensitive dependence on initial conditions implies that for at least one point y arbitrarily close to the point x, the f cause eventually deviation from x within at least δ under n iteration. It is not required for all points near x to exhibit this kind of behaviour, but there must be at least one such point in any x neighbourhood.

Definition 4 (Devaney's definition on chaos [34]). *Let us consider V a set and f a mapping $f : \mathcal{J} \to \mathcal{J}$. f is said to be chaotic on V if it satisfies the following conditions:*

- *f exhibits sensitive dependence on initial conditions,*
- *f is topologically transitive,*
- *periodic points are dense in V.*

Among these three conditions, the first one, sensitive dependence on initial conditions, is widely accepted as the central concept of chaos. However, it has been proven in [35] that for the mapping f, the sensitive dependence on initial conditions is redundant in the definition of chaos because the other two conditions imply that. Furthermore, [36] demonstrates that this is the only redundancy in definition 4.

2. Numerical Results

In this chapter, we aim to employ our theoretical concepts to examine the spacetime described by the metric (1.9). First, it is necessary to discuss the values of the parameters used. The metric tensor encompasses two parameters, the mass of black hole M and quadrupole perturbation parameter $\mathcal{Q}$. Moreover, as parameters for the test particle, we shall employ the conserved energy E and angular momenta L. To work with dimensionless quantities, we establish the scale of all parameters with respect to the black hole mass M, which effectively entails setting $M \equiv 1$.

To numerically integrate the geodesic equations (1.13) and obtain further numerical results, the new authentical program was written in environment *Wolfram Mathematica* (version 13.2.0). The numerical accuracy achieved during the integration is summarised in appendix A.1.

2.1 Reduced Hamiltonian

The initial system exhibits four degrees of freedom; however, if we examine the form of the metric (1.9), we see that it does not depend on the time variable t and the azimuthal angle ϕ. In section 1.6, we have previously discussed that these cyclic coordinates of the metric result in the conservation of the total energy E, respectively, in the conservation of the angular momentum L. Therefore, this symmetry allows us to reduce our system to a two degrees of freedom problem solely described by coordinates r and θ. The reduced Hamiltonian of this system takes the following form:

$$\mathcal{H} = \frac{1}{2}\left(\frac{(p_r)^2}{g_{rr}} + \frac{(p_\theta)^2}{g_{\theta\theta}} + \frac{E^2}{g_{tt}} + \frac{L^2}{g_{\phi\phi}}\right). \tag{2.1}$$

2.2 Effective potential

Upon examining the 4-momentum normalisation in equation (1.49), we can also apply it to our system. By rearranging the particular equation appropriately, we obtain the following:

$$(p^r)^2 + \frac{g_{\theta\theta}}{g_{rr}}\left(p^\theta\right)^2 = \frac{E^2}{-g_{rr}g_{tt}} - \frac{1}{g_{rr}}\left(m^2 + \frac{L^2}{g_{\phi\phi}}\right). \tag{2.2}$$

Assuming particles with non-zero mass, we can divide the entire equation by m^2 to obtain the final form:

$$(u^r)^2 + \frac{g_{\theta\theta}}{g_{rr}}\left(u^\theta\right)^2 = \frac{\widetilde{E}^2}{-g_{rr}g_{tt}} - \frac{1}{g_{rr}}\left(1 + \frac{\widetilde{L}^2}{g_{\phi\phi}}\right), \tag{2.3}$$

where we have again introduced the tilted quantities $\widetilde{E}$ and $\widetilde{L}$ with meaning per unit of rest mass. Throughout the remainder of this thesis, we will work solely with the quantities per unit of rest mass; thus, for the simplicity of notation, we will denote $\widetilde{E} \to E$ and $\widetilde{L} \to L$. Moreover, in the remainder of this thesis, we

will work with the radial part of the momentum per unit of rest mass; thus, for the simplicity of notation, we will denote p^r/m as p^r.

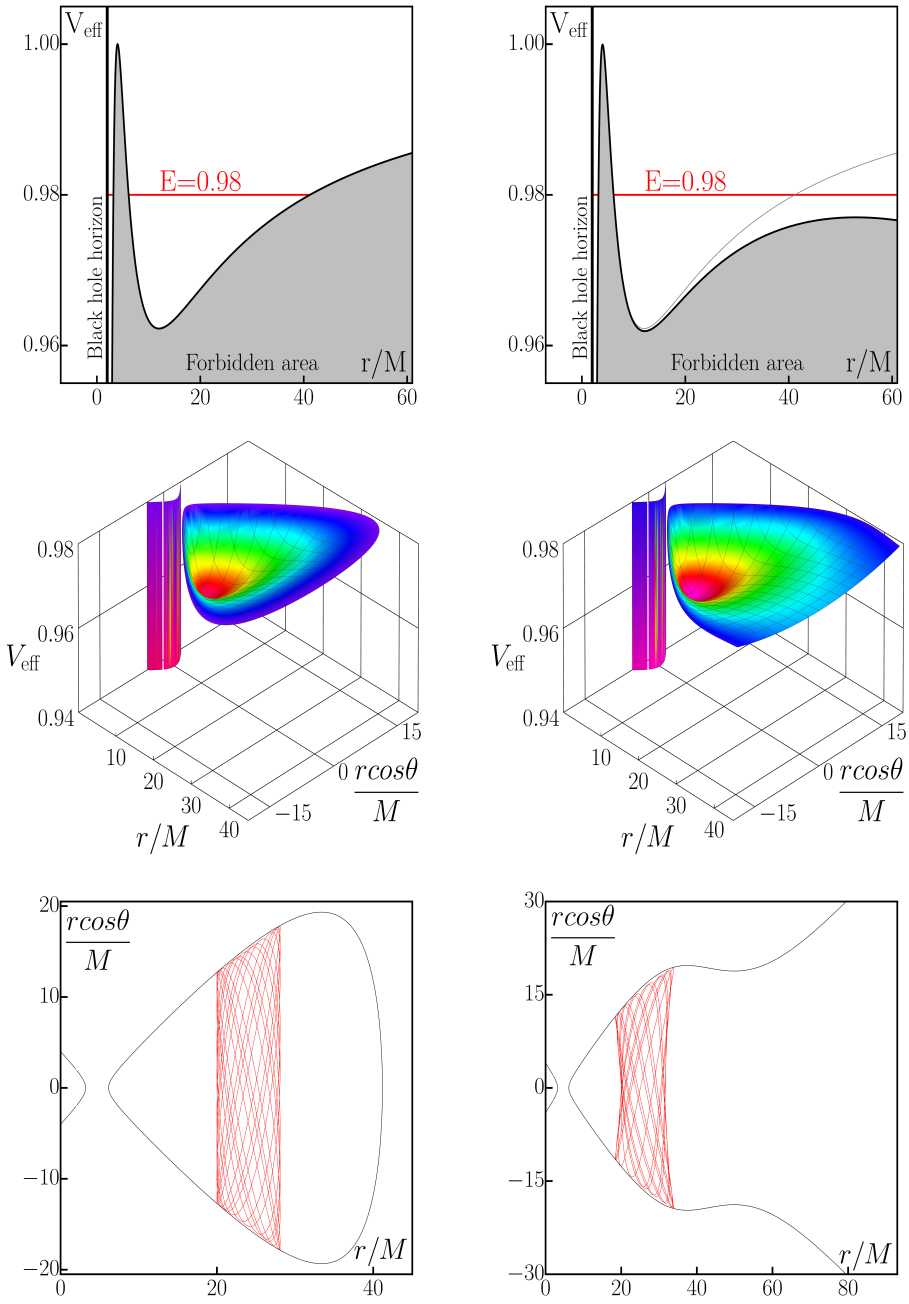

Figure 2.1: Three options on displaying the effective potential. The left column represents the slightly perturbed system ($\mathcal{Q} = 10^{-8}M^{-2}$), while the right column represents the significantly perturbed system ($\mathcal{Q} = 10^{-5}M^{-2}$). In the top figure of the right column, the grey line represents the effective potential of an unperturbed Schwarzshild solution. The first row is the 2D effective potential. The second row shows the 3D potential, where the displayed area corresponds to $E \leq 0.98$. The third row displays the intersection of the 3D potential with a plane of constant energy (i.e. the edge of the 3D potential for $E \leq 0.98$), denoted as the CZV. These plots also show projections onto CZV of bounded motion with a given energy. The parameters taken are $L = 4.0M, r\,[0] = 20M, p^r\,[0] = 0$ and $\theta\,[0] = \pi/2$.

In the Schwarzschild solution 1.7.2, the motion is planar, resulting in $u^\theta \equiv 0$. Consequently, the left-hand side of equation (2.3) reduces to the square of a real function (u^r), which allows us to employ a quantity of effective potential as the right side of equation 2.3. By perturbing the Schwarzschild solution, we have lost one of the integrals of motion; therefore, the motion is no longer planar and $u^\theta \not\equiv 0$. However, since the term $g_{\theta\theta}/g_{rr}$ is non-negative beyond $r = 2M$ (the black hole horizon), we can consider the left-hand side of the equation (2.3) to be non-negative in every reasonable region and employ the same procedure as before with the Schwarzschild solution.

To maintain the consistency with the effective potential presented in the theoretical part of this thesis, we demand that as $\mathcal{Q} \to 0$, the perturbed effective potential approaches the unperturbed one (for $\theta \equiv \pi/2$). Consequently, we define effective potential as follows:

$$V_{\text{eff}}(r, \theta) = \sqrt{E^2 + \frac{E^2}{g_{rr} g_{tt}} + \frac{1}{g_{rr}} \left(1 + \frac{L^2}{g_{\phi\phi}}\right)}. \tag{2.4}$$

The aforementioned definition of the effective potential appears identical to the one for the Schwarzschild solution. However, it is essential to note that the unperturbed effective potential is a function of a single variable (r), whereas the perturbed one (2.4) is a function of two variables (r, θ).

Although it is still possible to compute the one-dimensional effective potential as a function of the radial coordinate, similar to Figures 1.2 and 1.3, it is not as informative since it does not include all the possible turning point for a given energy. Alternatively, we could employ the two-dimensional effective potential (2.4), plotted as a function of r and θ. However, three-dimensional plots are not as concise in practical means. Therefore, we introduce the *curve of zero velocity* (abbreviated as the CZV) as a curve in meridian plane $(r, r \cdot \cos\theta)$, where the effective potential (2.4) is equal to specific energy, i.e. $V_{\text{eff}}(r, \theta) = E$. This nomenclature originates from the fact that whenever the right-hand side of equation (2.3) equals zero, it implies that both u^r and u^θ are also zero; thus, the velocity component in the meridian plane $(r, r \cdot \cos\theta)$ vanishes, indicating a turning point.

In Figure 2.1, a comparison of the three aforementioned plots is presented for two specific quadrupole perturbation parameters (for more examples on 3D potential, respectively, CZV curve in various spacetimes, see Refs. [37, 38]).

2.3 Poincaré surface of section

To study the particle's motion qualitatively, we should employ the Poincaré surface of section as described in 1.11. The system we study exhibits reflection symmetry along the equatorial plane; thus, in order to ensure that chosen section intersects the Hamiltonian flow perpendicularly, we set the Poincaré surface of section as the equatorial plane (i.e. $\theta \equiv \pi/2$). Additionally, we only consider points intersecting the surface of section from a specific direction, i.e. without loss of generality, selecting the additional condition $u^\theta > 0$. Therefore, we are left with the two remaining phase coordinates, r and p^r, which we record.

The illustrations of Poincaré surface of section are presented in the following discussion of the possible bounded motion (Fig. 2.2 - 2.5).

Let us emphasise that the accessible region of the Poincaré surface of section is determined by the normalisation of four-momentum (see e.g. [39]). To establish the boundary curve, we shall employ the effective potential 2.4 and define it as follows:

$$u^r = \pm\sqrt{E^2 - V_{\text{eff}}^2(r, \pi/2)}. \tag{2.5}$$

In the subsequent depictions of the Poincaré surface of section (except the ones in the following section, where the boundary curve is a thin black line), we represent this boundary curve of accessible region (2.5) as a thick magenta line.

2.3.1 Types of off-equatorial motion

To comprehend the diverse range of possible motions within the gravitational field described by the metric (1.9), we integrate the geodesic equations 1.13 and analyse the motion through various perspectives. We can identify four distinct scenarios of bounded motion for given energy, which we shall distinguish as follows:

- The generic circular orbit depicted in Fig. 2.2. Examining the spatial representation of this motion, we see that it is circular, although it is not confined to the equatorial plane. This observation becomes evident from the CZV, where the vertical line implies that r/M remains constant while θ oscillates between two values. The remaining subfigures further reinforce the fact that the motion is circular, as represented by the circular trajectory in the projection onto the equatorial plane, respectively, resembling a single point within the particular Poincaré surface of section.

- The invariant trajectory on the KAM torus depicted in Fig. 2.3. The spatial representation of this motion shows that the trajectory is not confined to any plane and might be considered chaotic at first sight. The remaining subfigures show this is false, and the motion is quasi-periodic. The curve of the Poincaré surface of section is closed, referring to the fact that the curve is mapped to itself.

- The resonant trajectory depicted in Fig. 2.4. The initial conditions are chosen to align approximately with the middle of the 2/3 resonance. The motion is thus seen as resonant straight from the spatial representation of this motion. Notably, the trajectory intersects the particular Poincaré surface of section in three distinct sets of points, indicating that the periodicity of the motion is three.

- The chaotic trajectory depicted in Fig. 2.5. The chaos is hardily observed from the spatial representation, respectively, from CZV and projection onto the equatorial plane. Nevertheless, upon examination of the particular Poincaré surface of section, we see solely the scattered distribution of points without discernible pattern, which is mostly referred to as a chaotic layer.

The concentric circles in the projections onto the equatorial plane are obtained from the effective potential (2.4) as the inner-most, respectively, the outer-most turning points for a given energy.

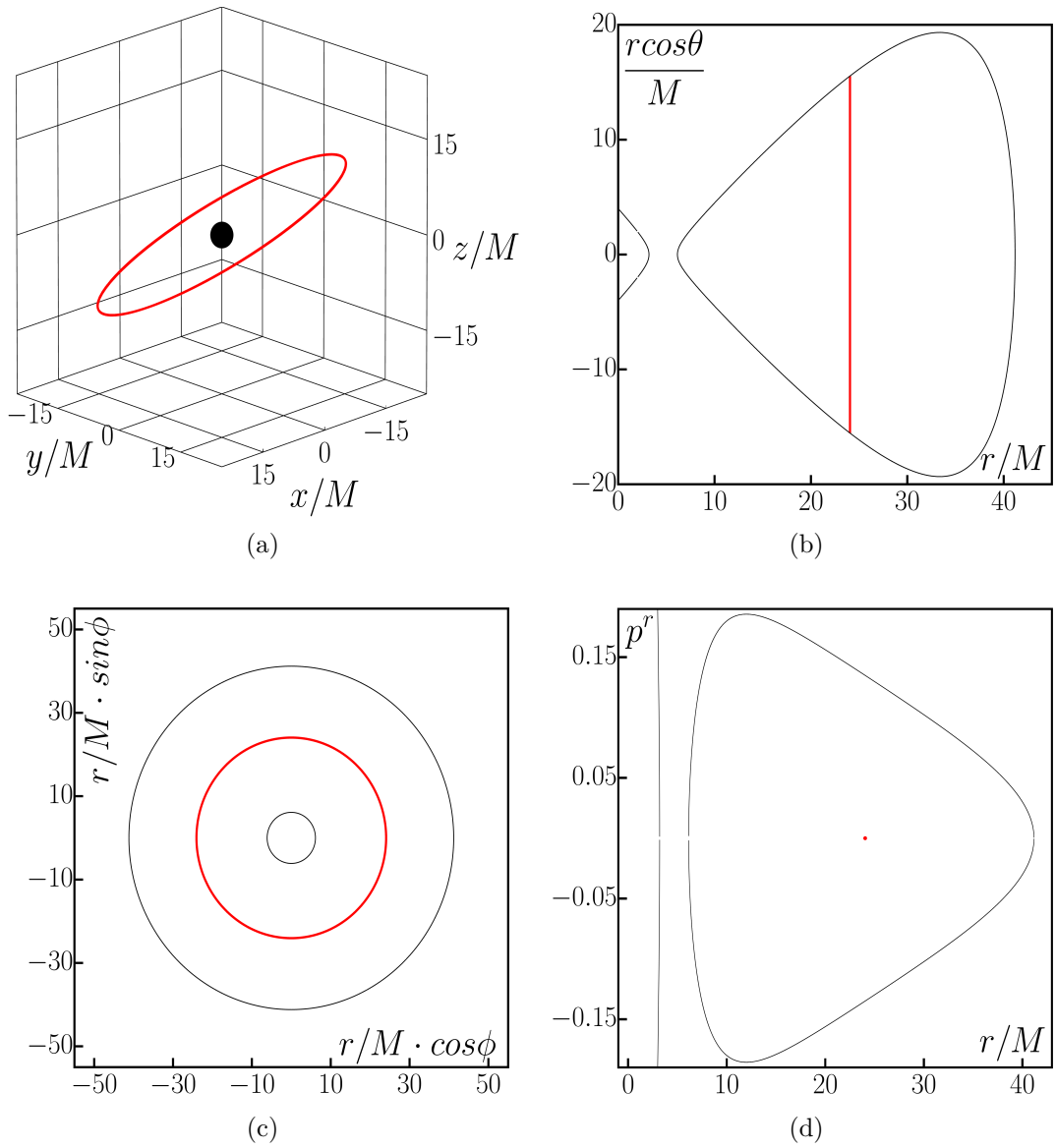

Figure 2.2: The circular motion of the slightly perturbed system. Figure (a) shows the spatial motion in Cartesian-like coordinates, with the trajectory calculated over $\tau = 10000$ time steps. Figure (b) displays the corresponding CZV, whereas figure (c) shows a projection of the motion onto the equatorial plane ($\theta = \pi/2$). Figure (d) depicts the Poincaré surface of section. The parameters taken are $L = 4.0M, E = 0.98, \mathcal{Q} = 10^{-8}M^{-2}, r\,[0] = 24.054M, p^r\,[0] = 0$ and $\theta\,[0] = \pi/2$.

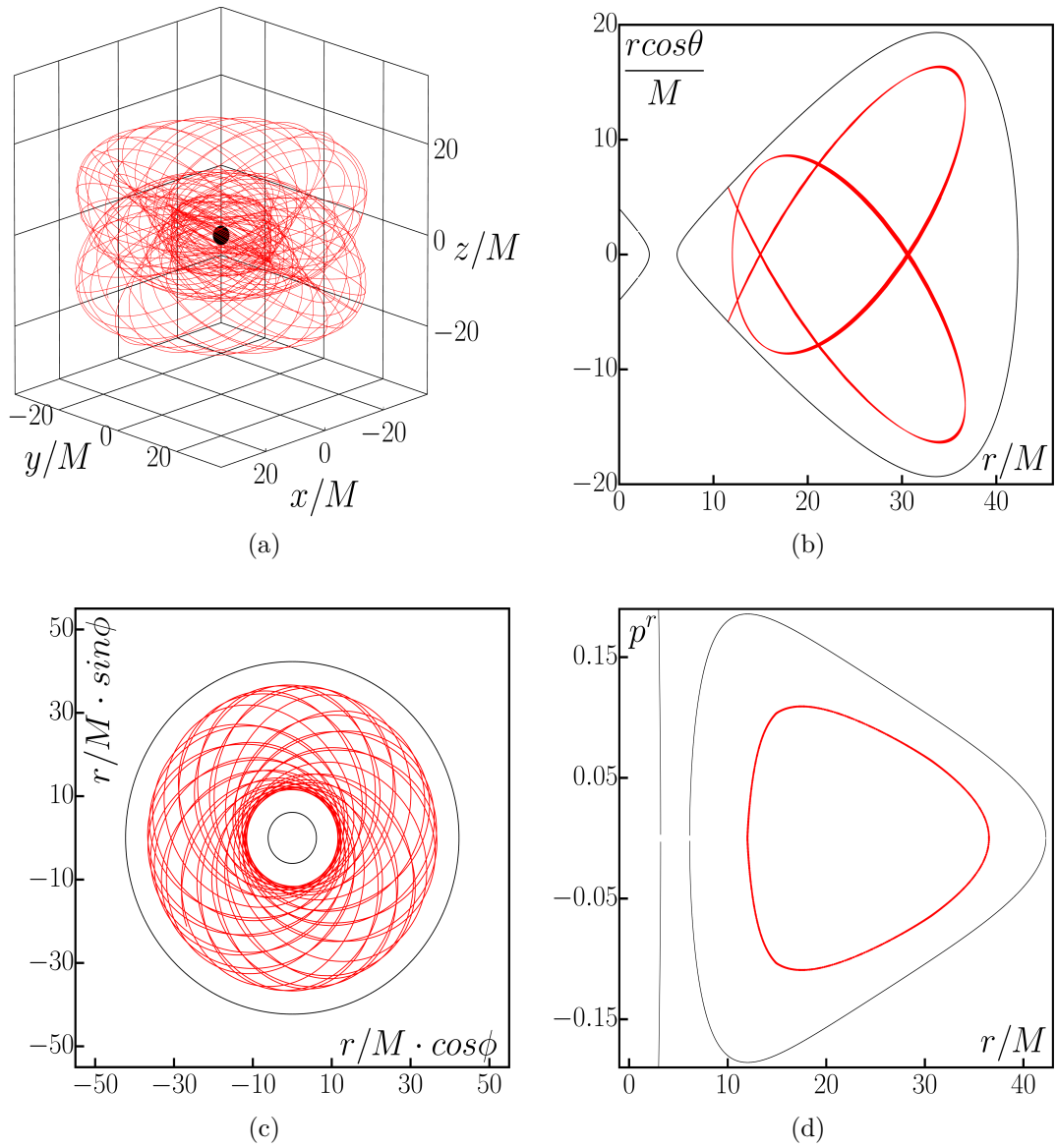

Figure 2.3: The invariant KAM trajectory of the perturbed system. Figure (a) shows the spatial motion in Cartesian-like coordinates, with the trajectory calculated over $\tau = 50000$ time steps. Figure (b) presents the corresponding CZV, whereas figure (c) shows a projection of the motion onto the equatorial plane ($\theta = \pi/2$). Figure (d) depicts the Poincaré surface of section. The parameters taken are $L = 4.0M, E = 0.98, \mathcal{Q} = 10^{-6}M^{-2}, r\,[0] = 12M, p^r\,[0] = 0$ and $\theta\,[0] = \pi/2$.

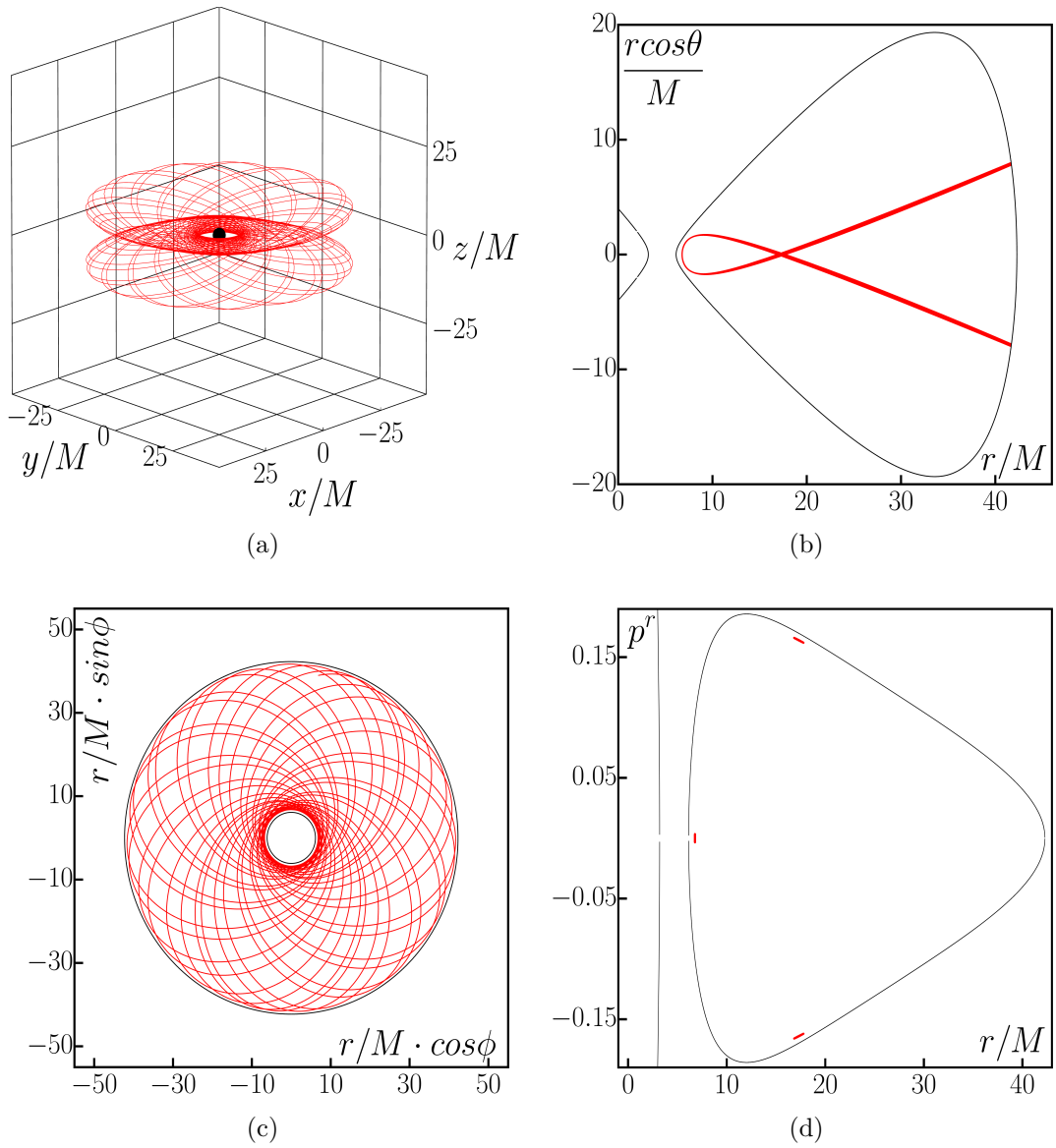

Figure 2.4: The resonant motion of the perturbed system with the ratio of the fundamental frequencies equal to 2/3. Figure (a) shows the spatial motion in Cartesian-like coordinates, with the trajectory calculated over $\tau = 50000$ time steps. Figure (b) presents the corresponding CZV, whereas figure (c) shows a projection of the motion onto the equatorial plane ($\theta = \pi/2$). Figure (d) depicts the Poincaré surface of section. The parameters taken are $L = 4.0M, E = 0.98, \mathcal{Q} = 10^{-6}M^{-2}, r\,[0] = 6.8M, p^r\,[0] = 0$ and $\theta\,[0] = \pi/2$.

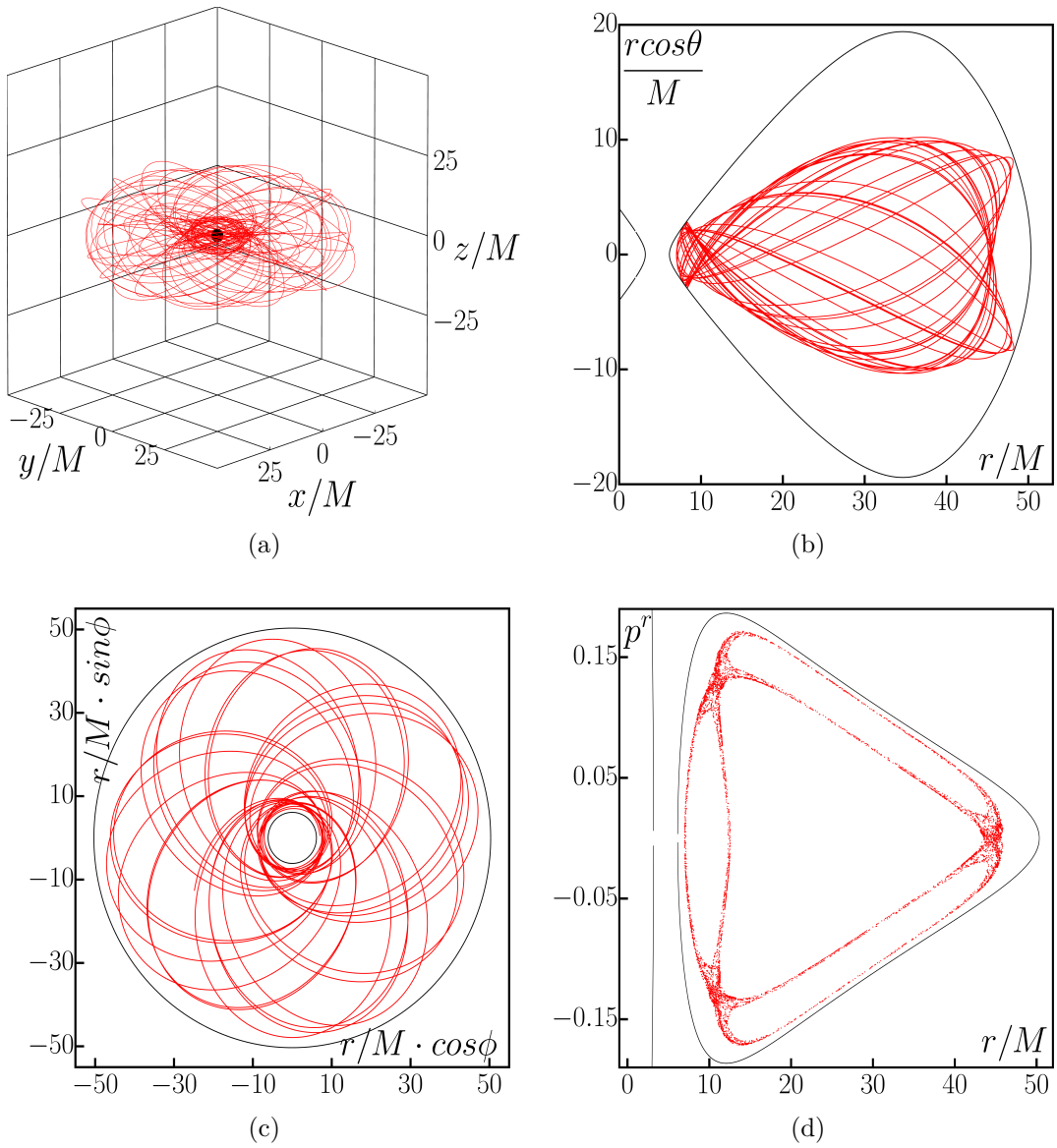

Figure 2.5: The chaotic motion of the significantly perturbed system. Figure (a) shows the spatial motion in Cartesian-like coordinates, with the trajectory calculated over $\tau = 50000$ time steps. Figure (b) presents the corresponding CZV, whereas figure (c) shows a projection of the motion onto the equatorial plane ($\theta = \pi/2$). Figure (d) depicts the Poincaré surface of section. The parameters taken are $L = 4.0M, E = 0.98, \mathcal{Q} = 5 \cdot 10^{-6} M^{-2}, r\,[0] = 7M, p^r\,[0] = 0$ and $\theta\,[0] = \pi/2$.

2.4 Rotation numbers

With the utilisation of Poincaré surfaces of section, we can proceed to employ the rotation numbers as described in section 1.13. Following the procedure, we initially distinguish the centre of the main island of stability. This fixed point is unique to each $\mathcal{Q}$ value and must be computed separately. Notably, as the quadrupole perturbation parameter $\mathcal{Q}$ increases, the centre gradually moves farther away from the black hole.

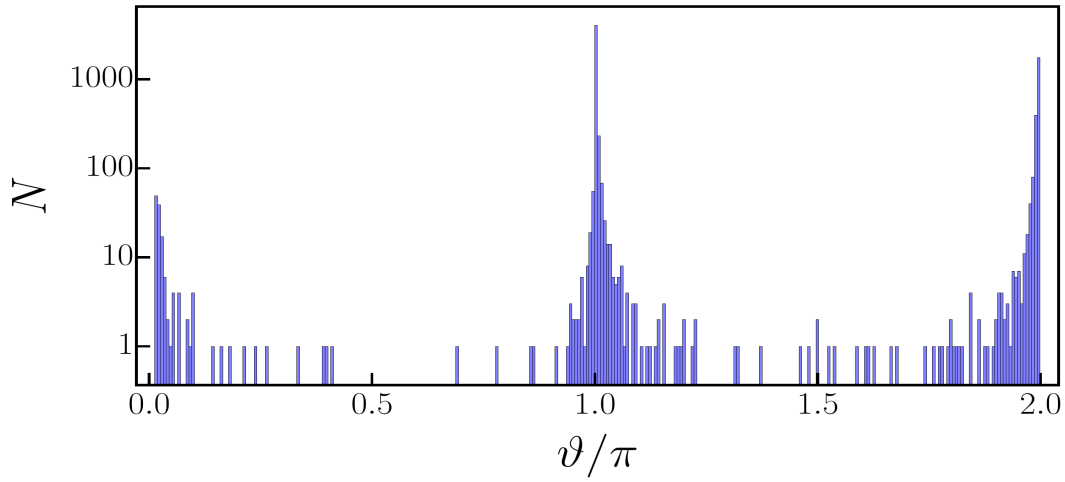

(a)

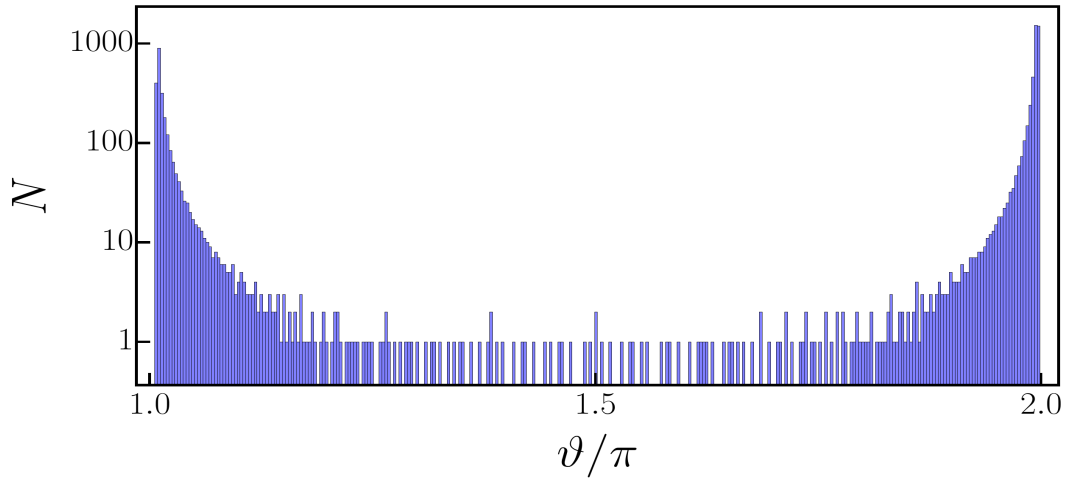

(b)

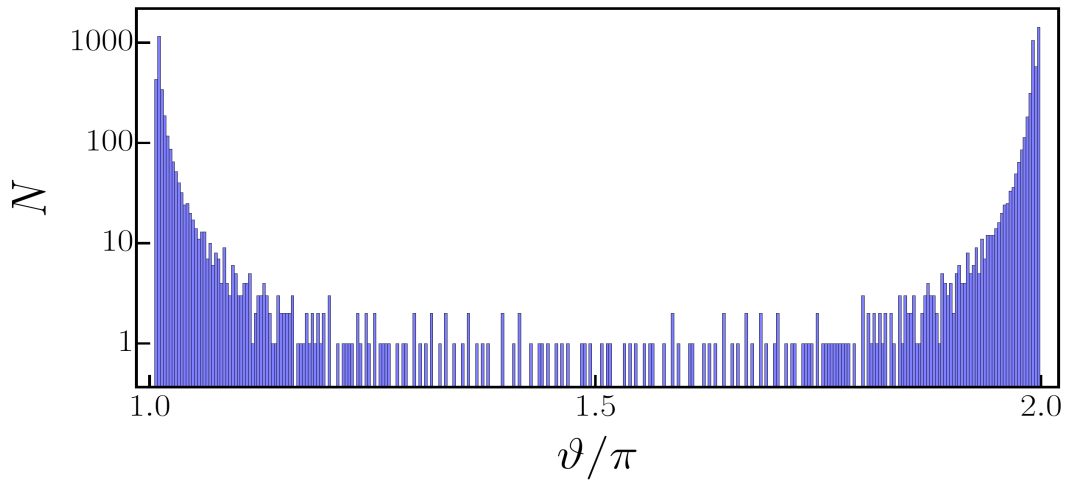

(c)

Figure 2.6: Rotation number spectra of a chaotic trajectory (a), a KAM trajectory (b) and a resonance trajectory (c). Histograms are in logarithmic scale with 7000 rotation angles in total distributed into 250 equally sized bins. The parameters employed to create these plots are $L = 4.0M, E = 0.98$, $\mathcal{Q} = 5 \cdot 10^{-6} M^{-2}$, $p^r\,[0] = 0$, $\theta\,[0] = \pi/2$ and $r_a\,[0] = 12.298M$; $r_b\,[0] = 21.298M$; $r_c\,[0] = 32.298M$.

Consequently, we are able to compute the rotation angles (1.72). As was mentioned earlier, it is necessary to ensure that the rotation angle spectrum does not have any discontinuity. In Fig. 2.6 are plotted three rotation spectra. We see that the chaotic spectrum lies within the interval $[0, 2\pi)$, whereas the KAM and resonance spectra are in the interval $[\pi, 2\pi)$. However, none of them possesses any discontinuity. Therefore, we can proceed to calculate the rotation numbers as given by equation (1.73).

The definition of rotation numbers (1.73) assumes that as the number of rotation angles N approach infinity, the rotation number corresponds to the ratio of two fundamental frequencies ω^1/ω^2. For finite N, the inaccuracy of calculations is approximately equal to [32]:

$$\delta_\vartheta = \frac{\Delta}{N}, \text{ where } 0 < \Delta < 1. \tag{2.6}$$

Hence, in order to obtain more precise values of rotation numbers, it is necessary to record more rotation angles. Typically, we calculate the trajectory for the subsequent plots until the 7000 rotation angles have been recorded. However, in section 2.5, we need to acquire better accuracy; therefore, the motion undergoes the calculation until 35000 rotation angles have been recorded.

Figs. 2.7 - 2.24 depict Poincaré surfaces of section along with the corresponding rotation curve for several different values of the quadrupole perturbation parameter $\mathcal{Q}$.

2.5 Resonance growth

We have previously described in the theoretical section 1.13 that the resonance width is a useful measure as it can be related to the perturbation parameter ϵ. From Fig. 2.7 - 2.24, it is evident that this width of all resonances grows as the quadrupole perturbation parameter $\mathcal{Q}$ increases.

By taking the logarithm of the equation (1.79), we obtain:

$$\log w\left(\mathcal{Q}\right) = \frac{1}{2}\log \epsilon\left(\mathcal{Q}\right) + \log 4\sqrt{\frac{\alpha}{\beta}}, \tag{2.7}$$

where we emphasise that on the right-hand side of the equation, only ϵ is dependent on $\mathcal{Q}$ as α and β are positive parameters. Therefore, by plotting the width of the resonance with respect to the quadrupole perturbation parameter on a logarithmic scale and performing the linear regression, we are able to quantify the relation between ϵ and $\mathcal{Q}$. The aforementioned linear regression takes the following form:

$$\log \frac{w\left(\mathcal{Q}\right)}{M} = A \cdot \log \mathcal{Q}M^2 + B. \tag{2.8}$$

Thus, by comparing the equations (2.7) and (2.8), we obtain the following power law expression for the perturbation parameter:

$$\epsilon = (\mathcal{Q}M^2)^{2A}. \tag{2.9}$$

In the subsequent sections, we examine four resonances, which have already been identified in Fig. 2.7 - 2.24.

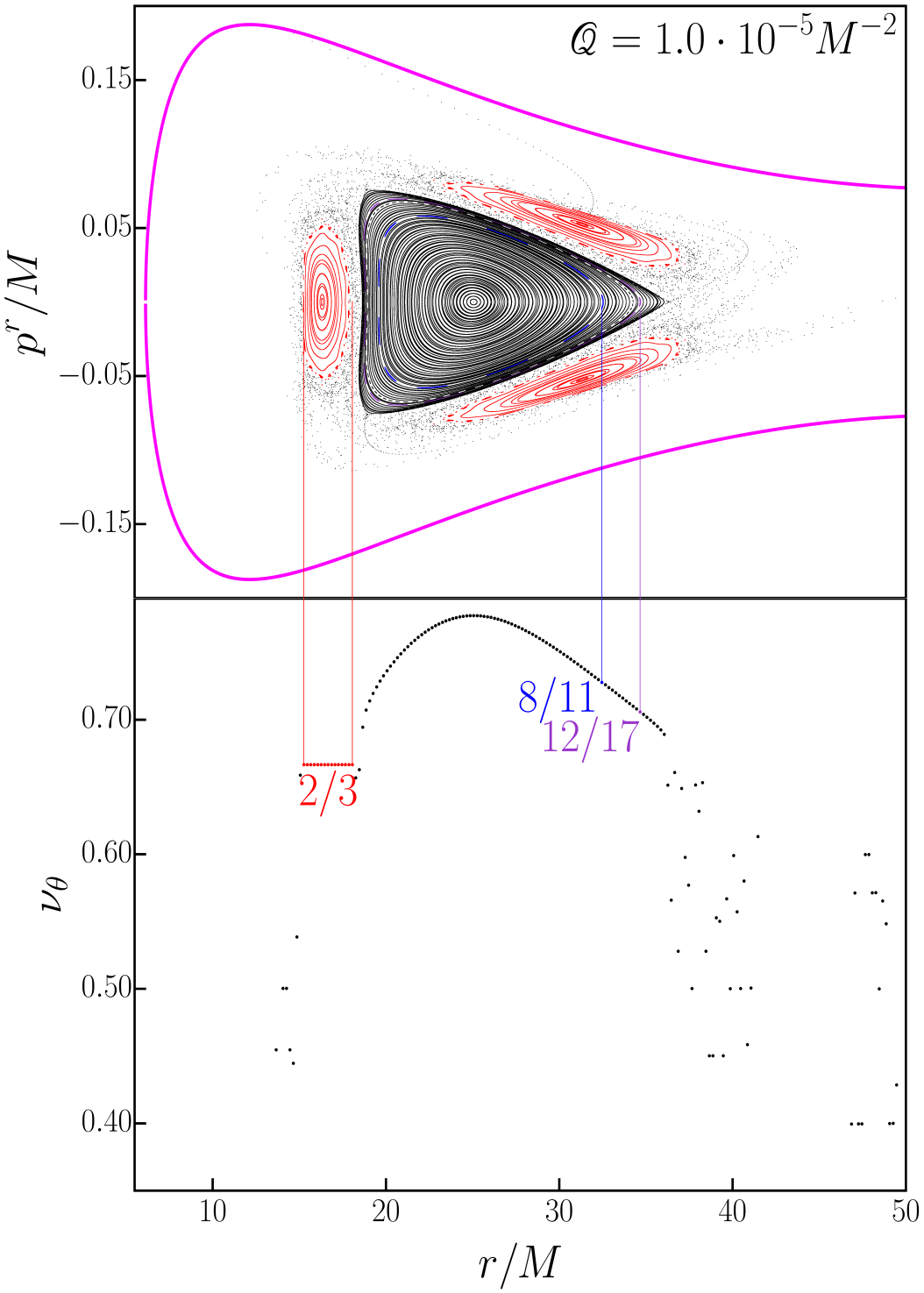

Figure 2.7: The top figure displays a Poincaré surface of section, while the bottom figure shows the corresponding rotation curve computed along the $p^r = 0$ line. The dominant resonances are prominently marked in both figures, along with their ratios of fundamental frequencies. The parameters taken are $L = 4.0M$, $E = 0.98$, $\theta\,[0] = \pi/2$ and $r\,[0] \in (6.063M; 50.063M)$ with step size $0.2M$.

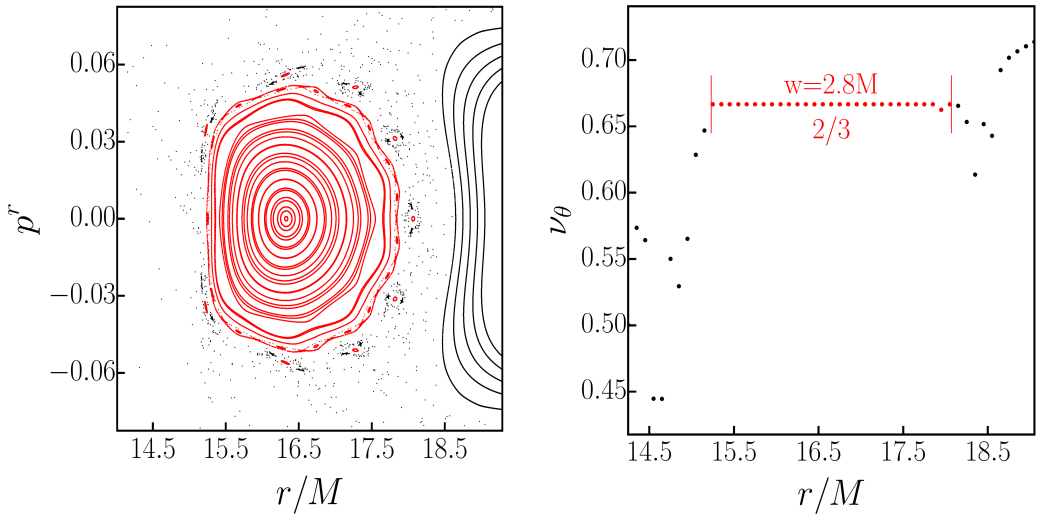

(a) The resonance $\omega^1/\omega^2 = 2/3$

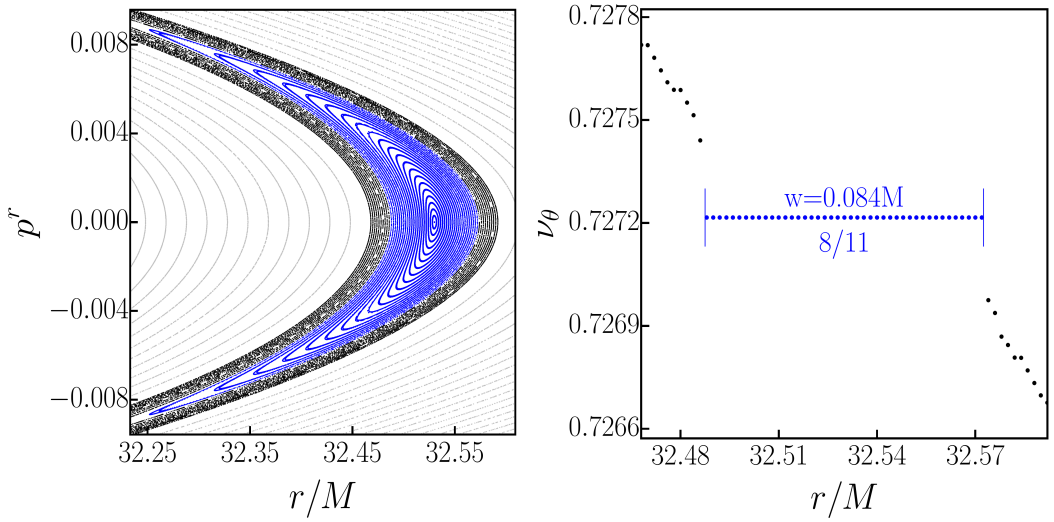

(b) The resonance $\omega^1/\omega^2 = 8/11$

Figure 2.8: Details from the Poincaré surface of section shown in Fig. 2.7 that focus on the most prominent resonances. In (a) the initial radius $r\,[0] \in (14.25M; 19.05M)$ and changes with step size $0.1M$; in (b) $r\,[0] \in (32.468M; 32.592M)$ with step size $0.002M$. Away from the resonance, the step size is magnified ten times, and the respective KAMs are depicted in the figure in grey colour.

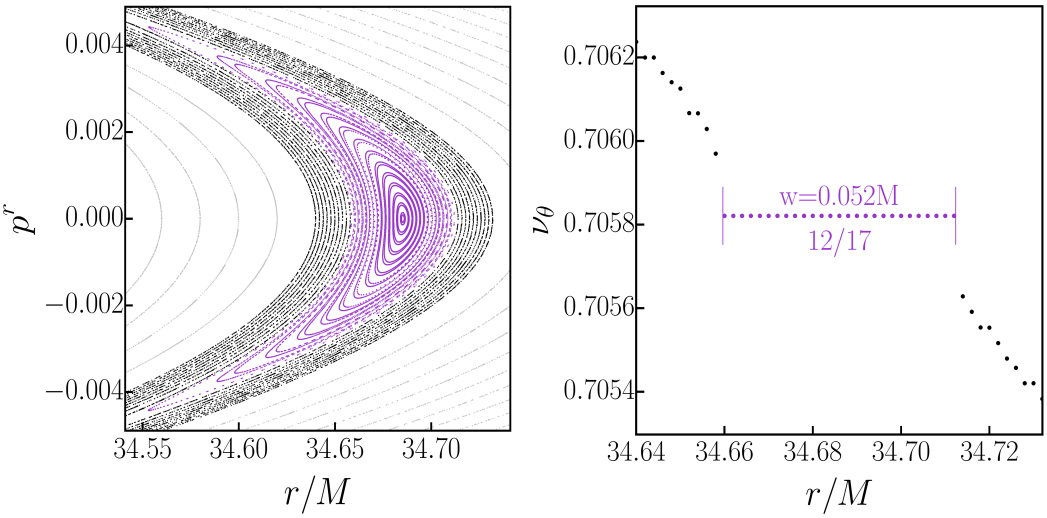

(c) The resonance $\omega^1/\omega^2 = 12/17$

Figure 2.8: In (c) $r\,[0] \in (34.640M; 34.732M)$ with step size $0.002M$.

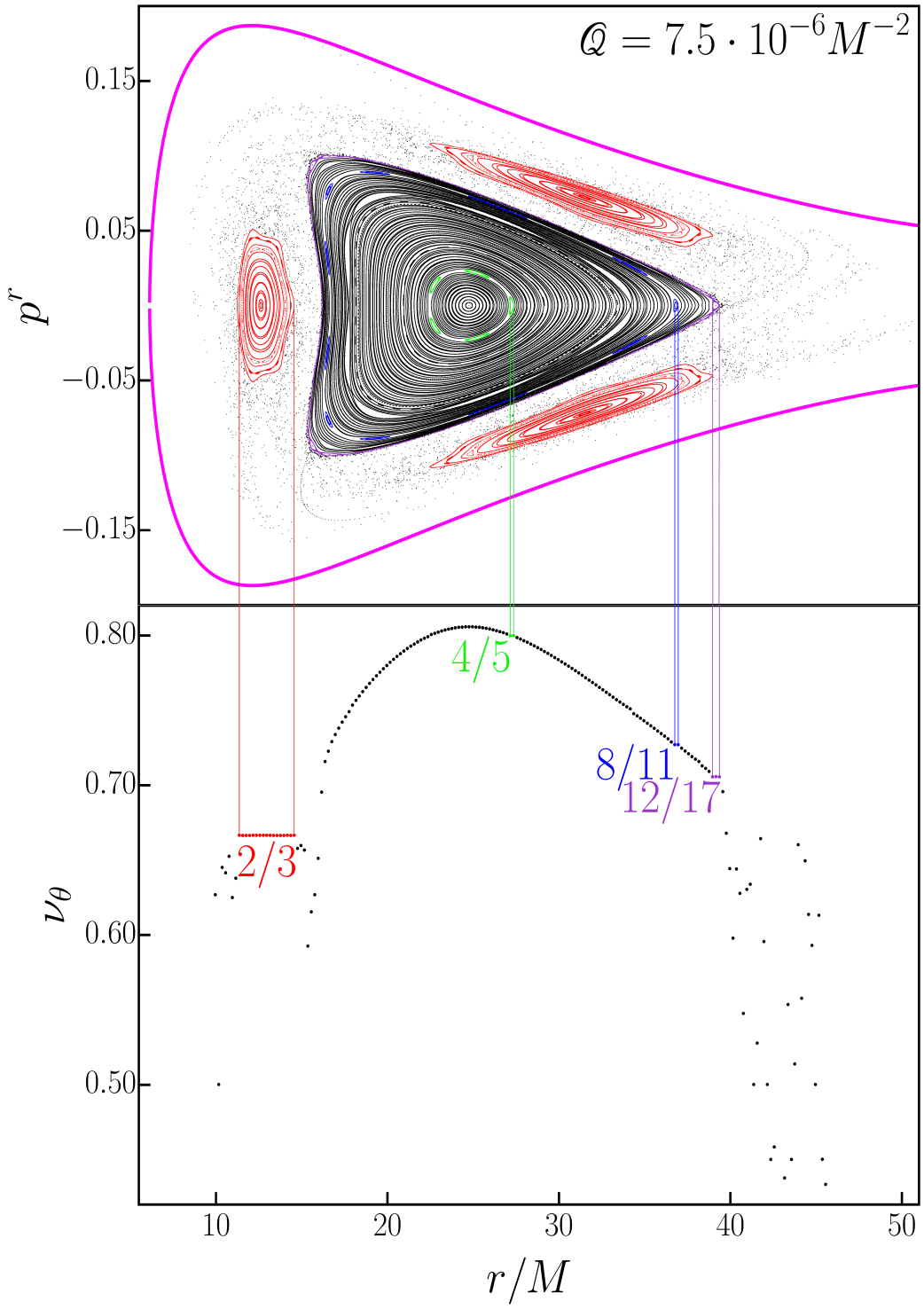

Figure 2.9: The top figure displays a Poincaré surface of section, while the bottom figure shows the corresponding rotation curve computed along the $p^r = 0$ line. The dominant resonances are prominently marked in both figures, along with their ratios of fundamental frequencies. The parameters taken are $L = 4.0M$, $E = 0.98$, $\theta\,[0] = \pi/2$ and $r\,[0] \in (6.159M; 50.159M)$ with step size $0.2M$.

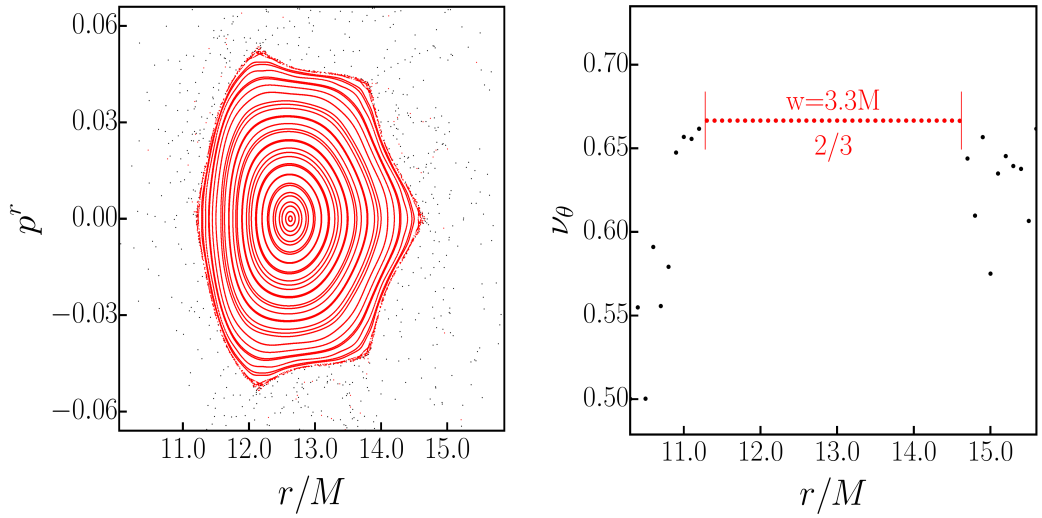

(a) The resonance $\omega^1/\omega^2 = 2/3$

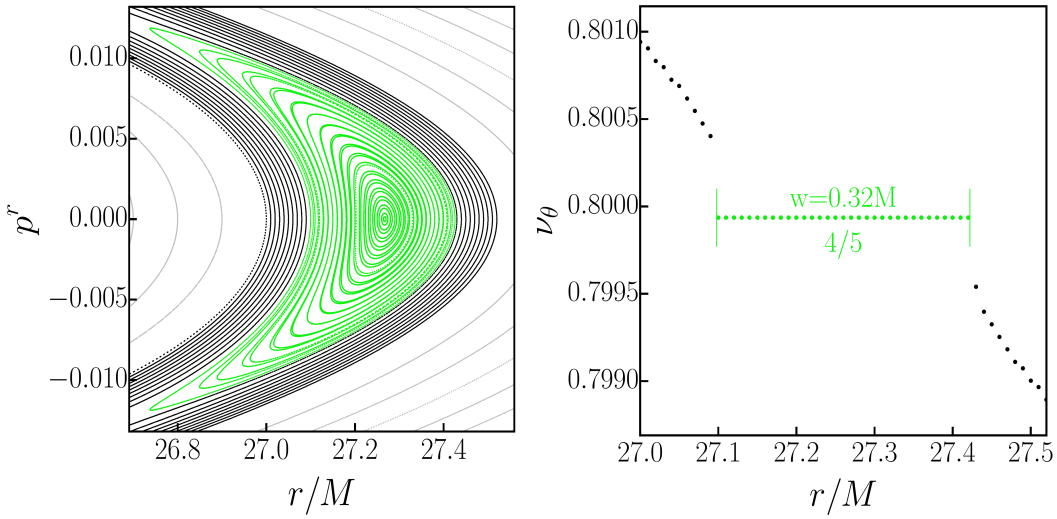

(b) The resonance $\omega^1/\omega^2 = 4/5$

Figure 2.10: Details from the Poincaré surface of section shown in Fig. 2.9 that focus on the most prominent resonances. In (a) the initial radius $r\,[0] \in (10.3M; 15.6M)$ and changes with step size $0.1M$; in (b) $r\,[0] \in (27.00M; 27.52M)$ with step size $0.01M$. Away from the resonance, the step size is magnified ten times, and the respective KAMs are depicted in the figure in grey colour.

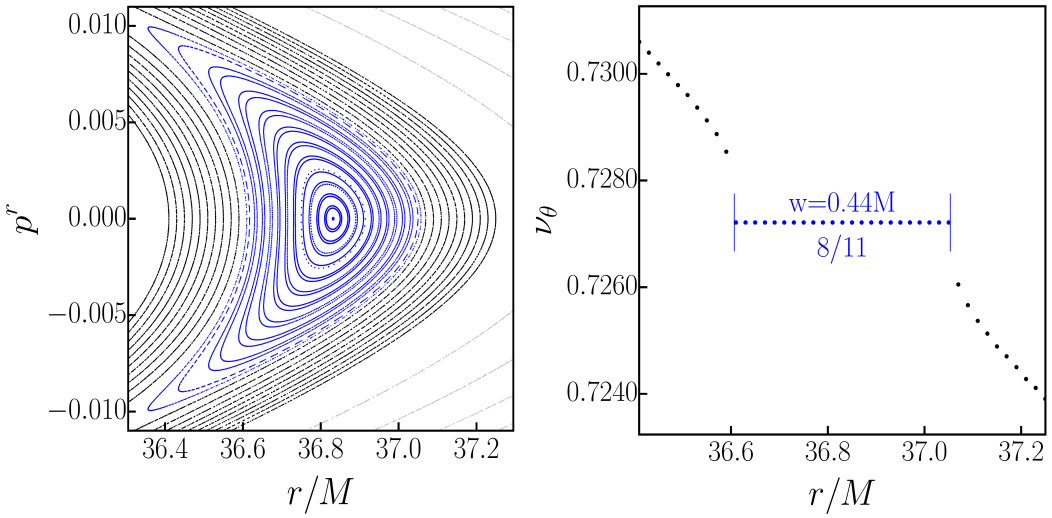

(c) The resonance $\omega^1/\omega^2 = 8/11$

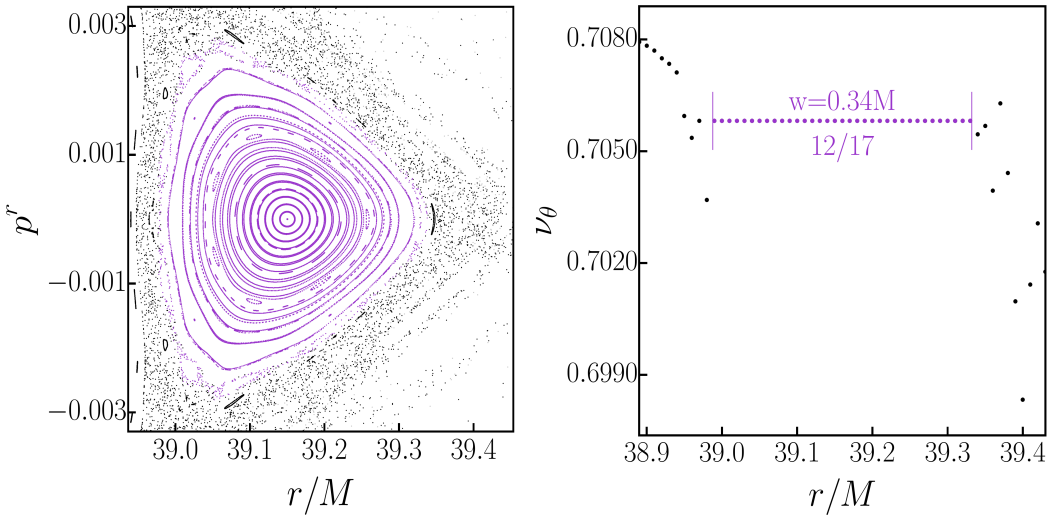

(d) The resonance $\omega^1/\omega^2 = 12/17$

Figure 2.10: In (c) the initial radius $r\,[0] \in (36.41M; 37.25M)$ with step size $0.02M$; in (d) $r\,[0] \in (38.89M; 39.43M)$ with step size $0.01M$.

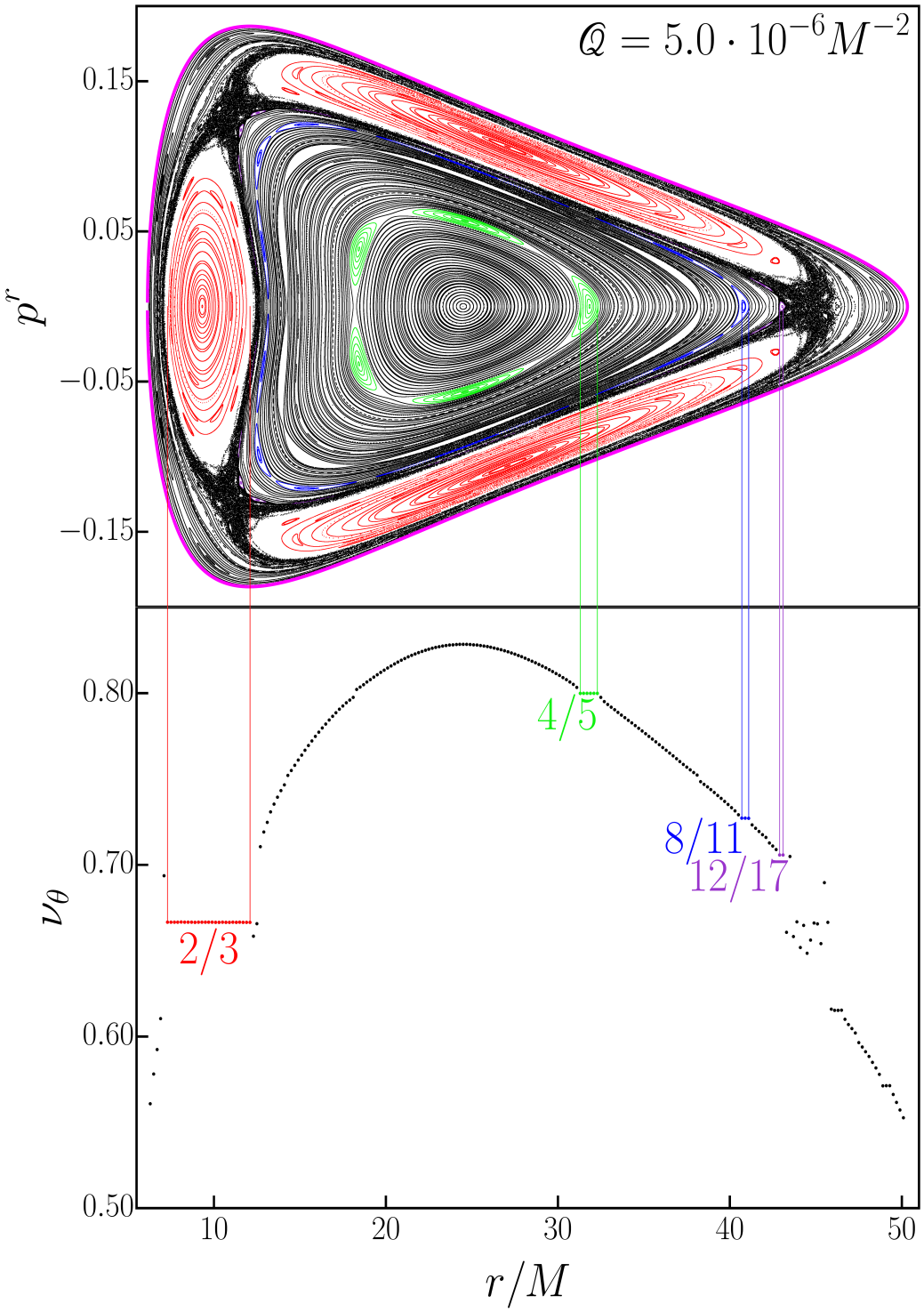

Figure 2.11: The top figure displays a Poincaré surface of section, while the bottom figure shows the corresponding rotation curve computed along the $p^r = 0$ line. The dominant resonances are prominently marked in both figures, along with their ratios of fundamental frequencies. The parameters taken are $L = 4.0M$, $E = 0.98$, $\theta\,[0] = \pi/2$ and $r\,[0] \in (6.298M; 50.098M)$ with step size $0.2M$.

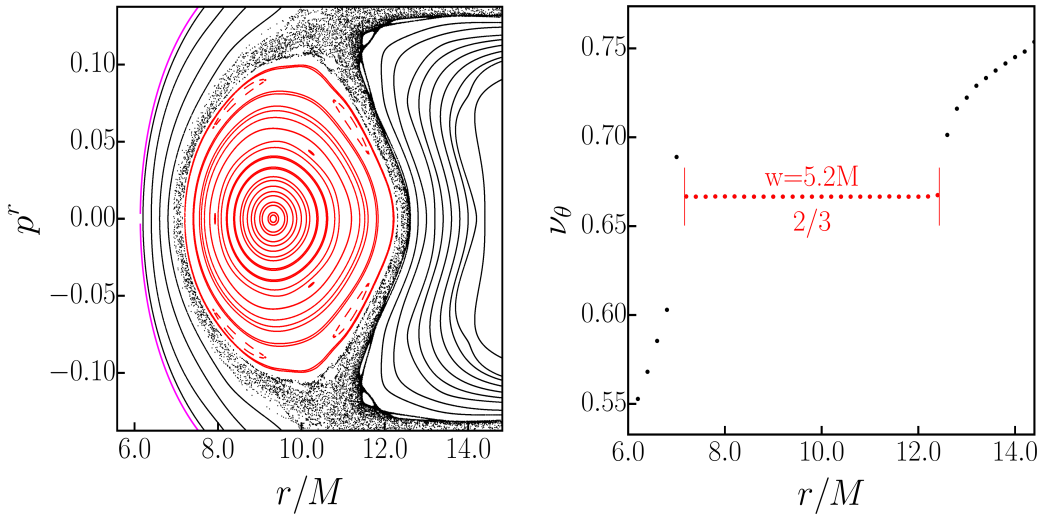

(a) The resonance $\omega^1/\omega^2 = 2/3$

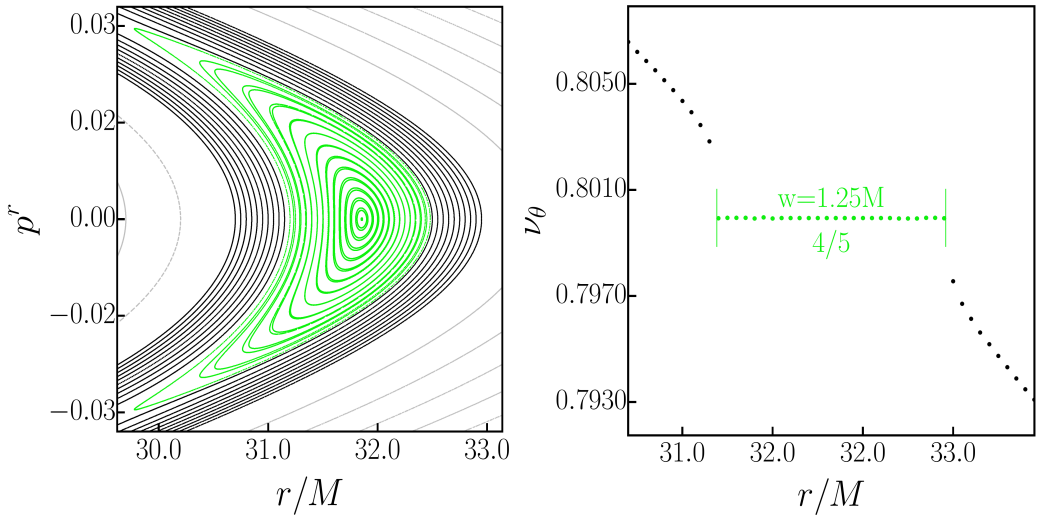

(b) The resonance $\omega^1/\omega^2 = 4/5$

Figure 2.12: Details from the Poincaré surface of section shown in Fig. 2.11 that focus on the most prominent resonances. In (a) the initial radius $r\,[0] \in (6.0M; 14.0M)$ and changes with step size $0.2M$; in (b) $r\,[0] \in (30.7M; 32.95M)$ with step size $0.05M$. Away from the resonance, the step size is magnified ten times, and the respective KAMs are depicted in the figure in grey colour.

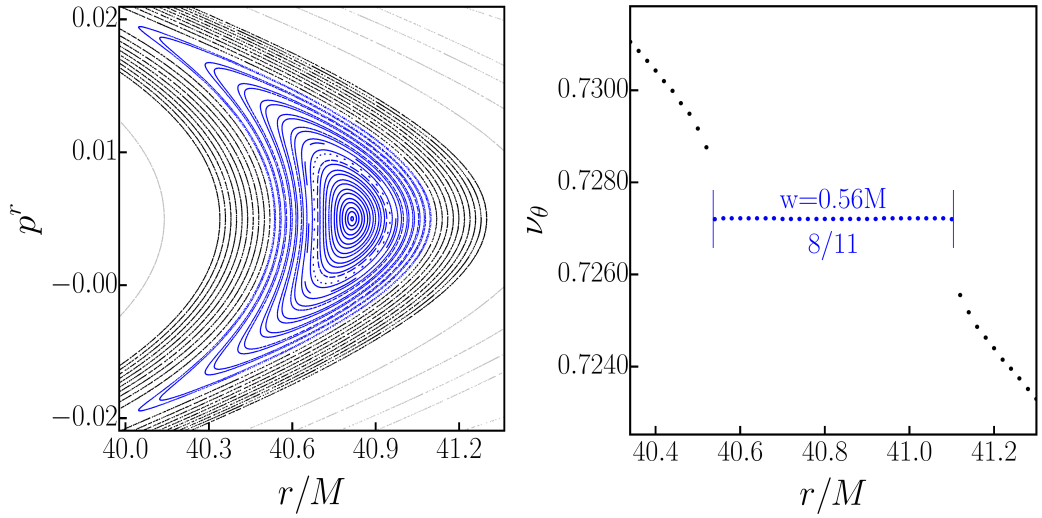

(c) The resonance $\omega^1/\omega^2 = 8/11$

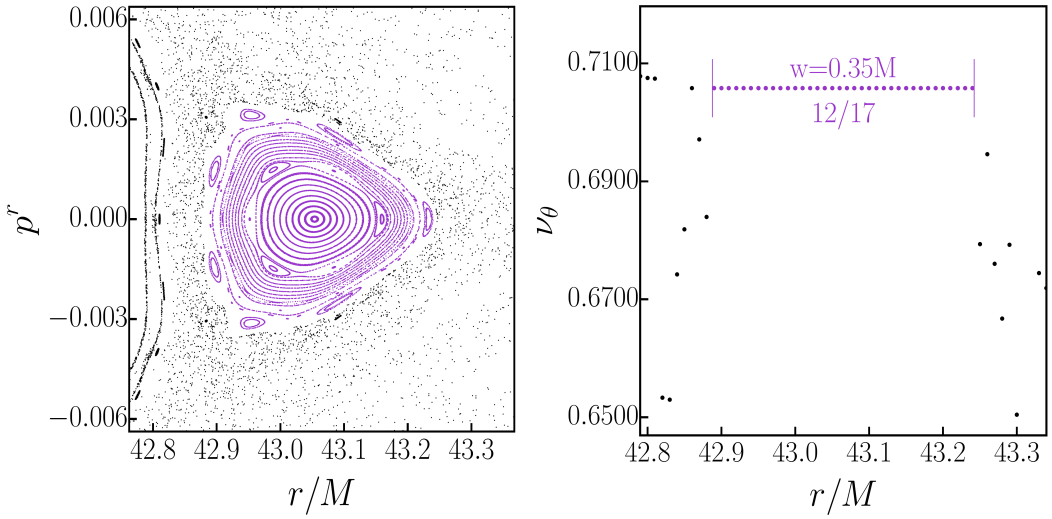

(d) The resonance $\omega^1/\omega^2 = 12/17$

Figure 2.12: In (c) the initial radius $r\,[0] \in (40.34M; 41.30M)$ with step size $0.02M$; in (d) $r\,[0] \in (42.79M; 43.34M)$ with step size $0.01M$.

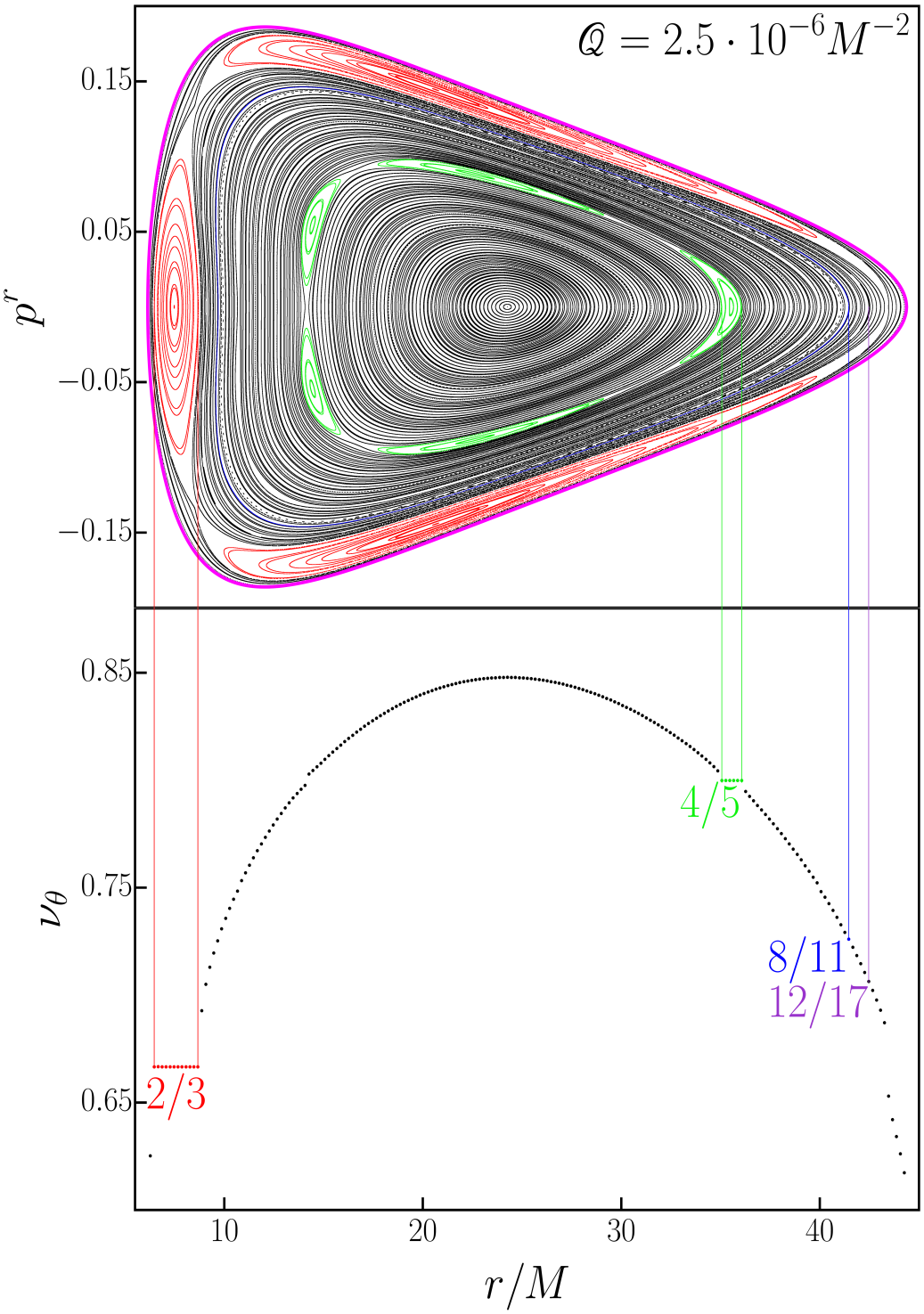

Figure 2.13: The top figure displays a Poincaré surface of section, while the bottom figure shows the corresponding rotation curve computed along the $p^r = 0$ line. The dominant resonances are prominently marked in both figures, along with their ratios of fundamental frequencies. The parameters taken are $L = 4.0M$, $E = 0.98$, $\theta\,[0] = \pi/2$ and $r\,[0] \in (6.266M; 44.266M)$ with step size $0.2M$.

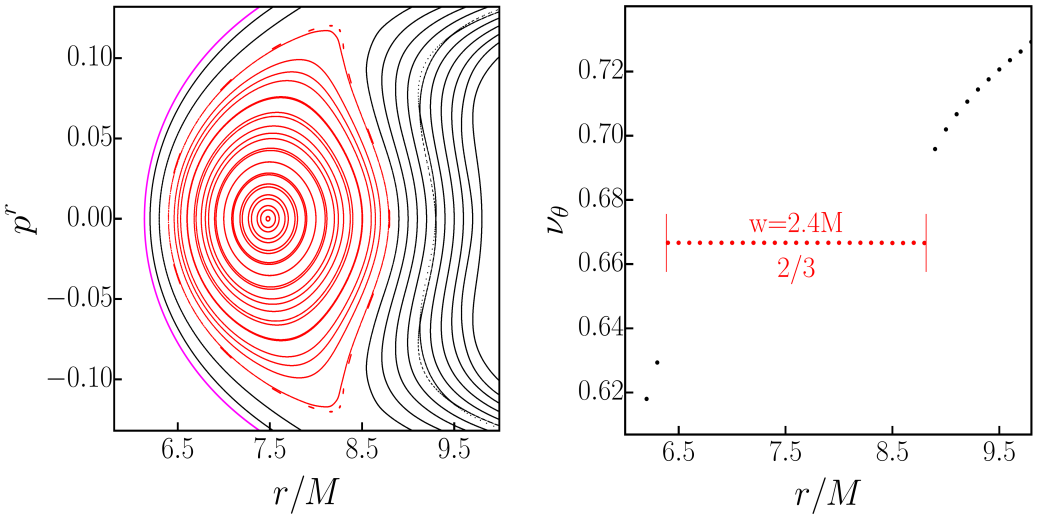

(a) The resonance $\omega^1/\omega^2 = 2/3$

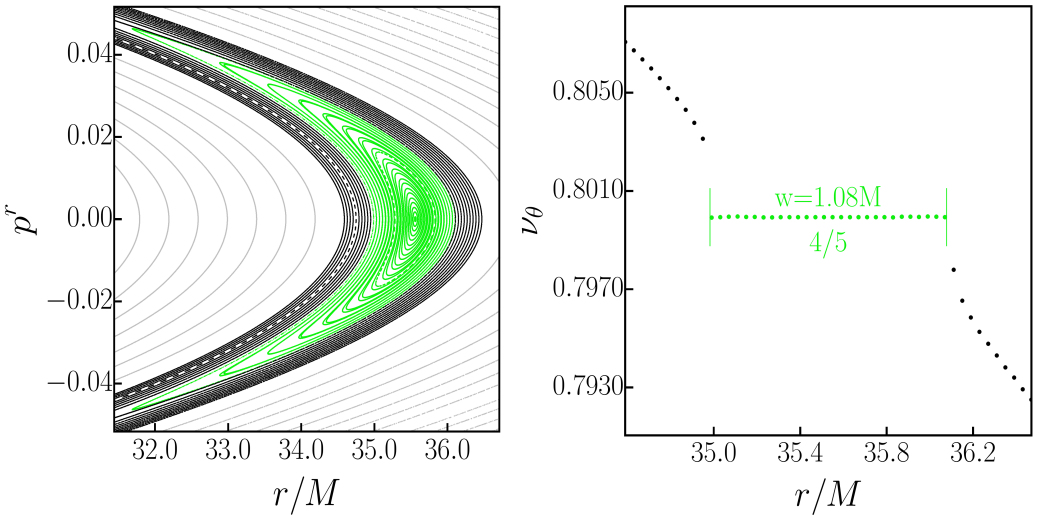

(b) The resonance $\omega^1/\omega^2 = 4/5$

Figure 2.14: Details from the Poincaré surface of section shown in Fig. 2.13 that focus on the most prominent resonances. In (a) the initial radius $r\,[0] \in (6.0M; 9.8M)$ and changes with step size $0.1M$; in (b) $r\,[0] \in (34.59M; 36.47M)$ with step size $0.04M$. Away from the resonance, the step size is magnified ten times, and the respective KAMs are depicted in the figure in grey colour.

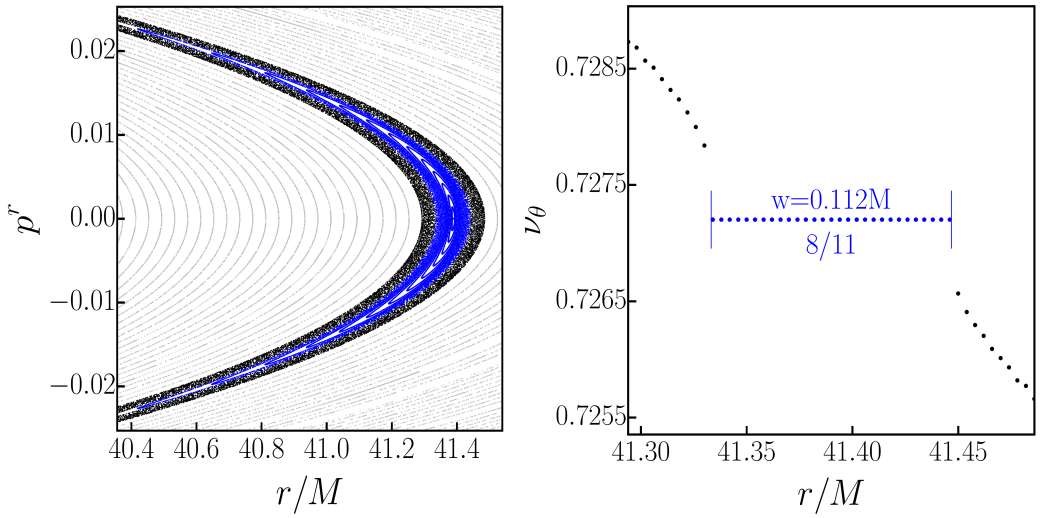

(c) The resonance $\omega^1/\omega^2 = 8/11$

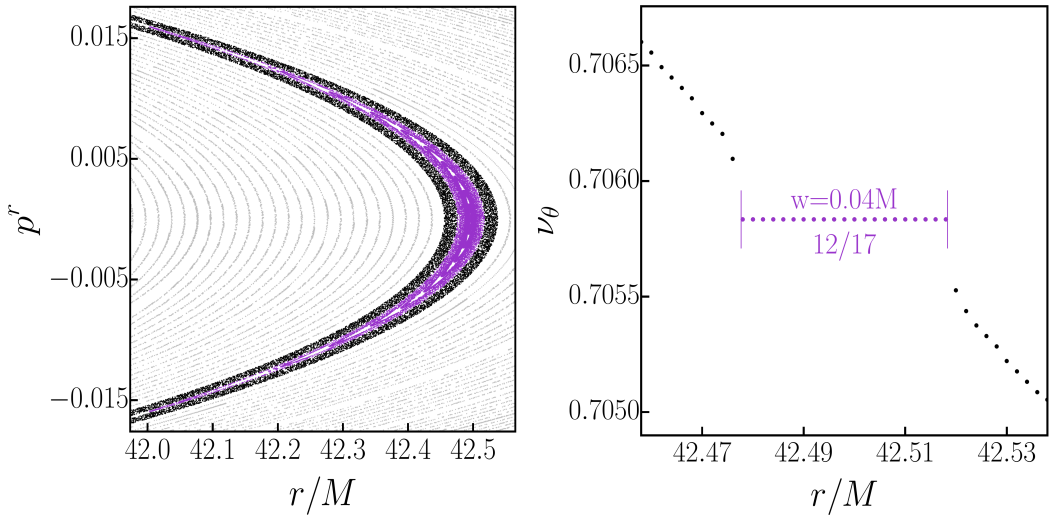

(d) The resonance $\omega^1/\omega^2 = 12/17$

Figure 2.14: In (c) the initial radius $r\,[0] \in (41.294M; 41.486M)$ with step size $0.004M$; in (d) $r\,[0] \in (42.458M; 42.538M)$ with step size $0.002M$.

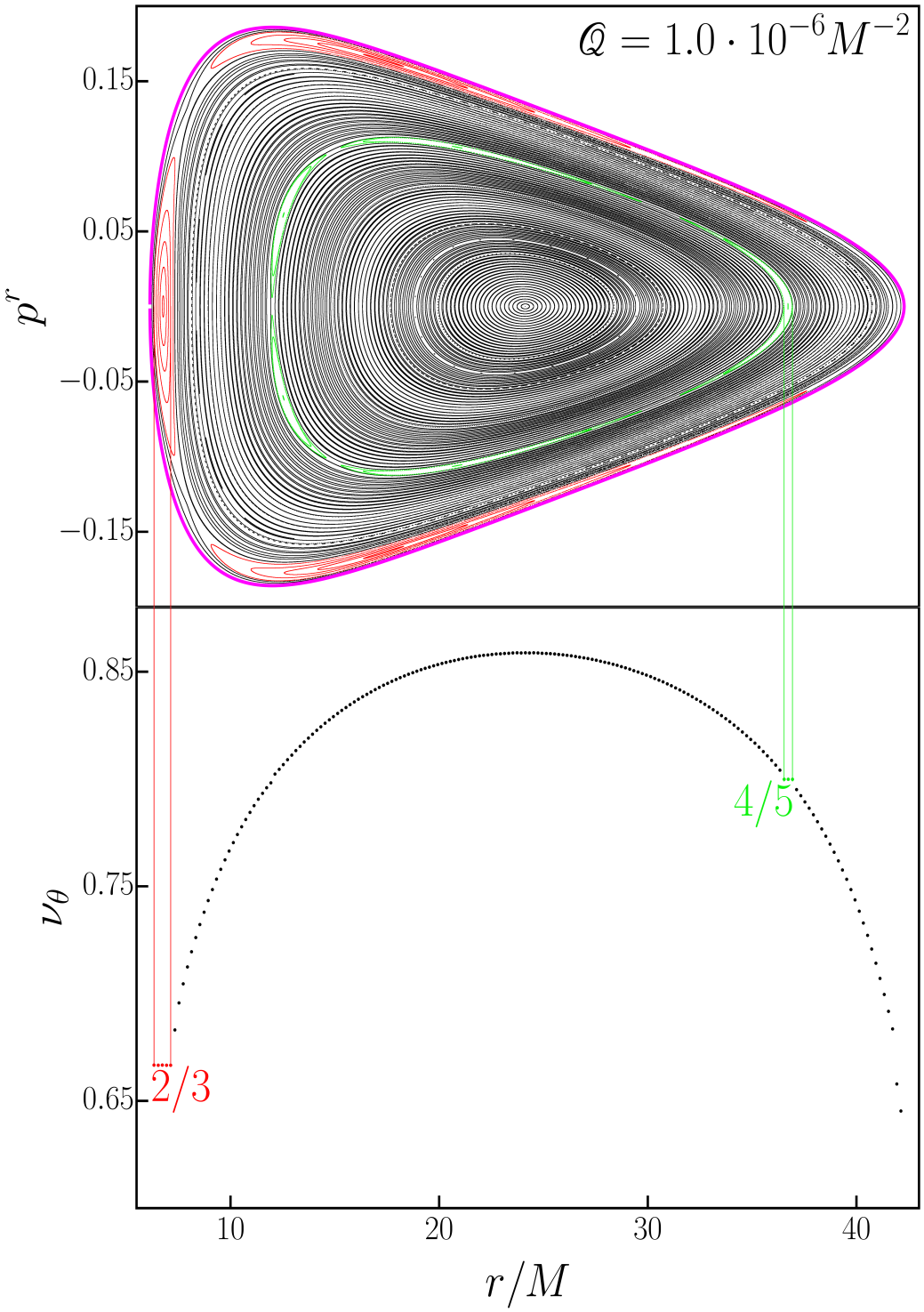

Figure 2.15: The top figure displays a Poincaré surface of section, while the bottom figure shows the corresponding rotation curve computed along the $p^r = 0$ line. The dominant resonances are prominently marked in both figures, along with their ratios of fundamental frequencies. The parameters taken are $L = 4.0M$, $E = 0.98$, $\theta\,[0] = \pi/2$ and $r\,[0] \in (6.336M; 42.136M)$ with step size $0.2M$.

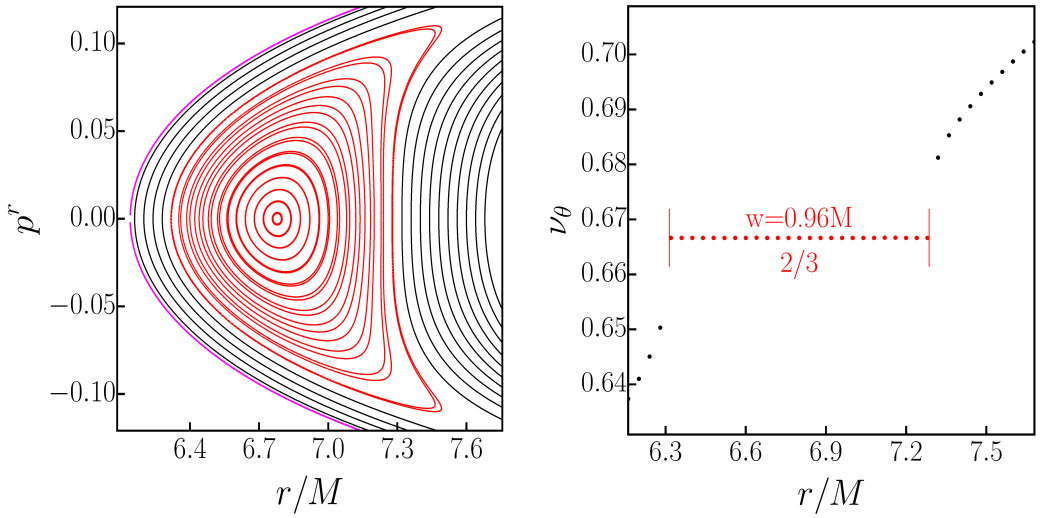

(a) The resonance $\omega^1/\omega^2 = 2/3$

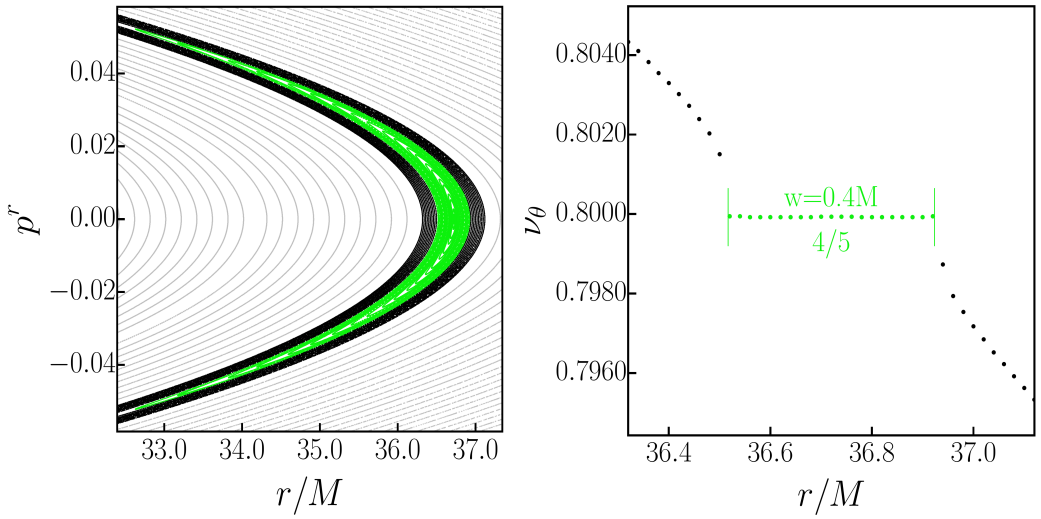

(b) The resonance $\omega^1/\omega^2 = 4/5$

Figure 2.16: Details from the Poincaré surface of section shown in Fig. 2.15 that focus on the most prominent resonances. In (a) the initial radius $r\,[0] \in (6.16M; 7.68M)$ and changes with step size $0.04M$; in (b) $r\,[0] \in (36.32M; 37.12M)$ with step size $0.02M$. Away from the resonance, the step size is magnified ten times, and the respective KAMs are depicted in the figure in grey colour.

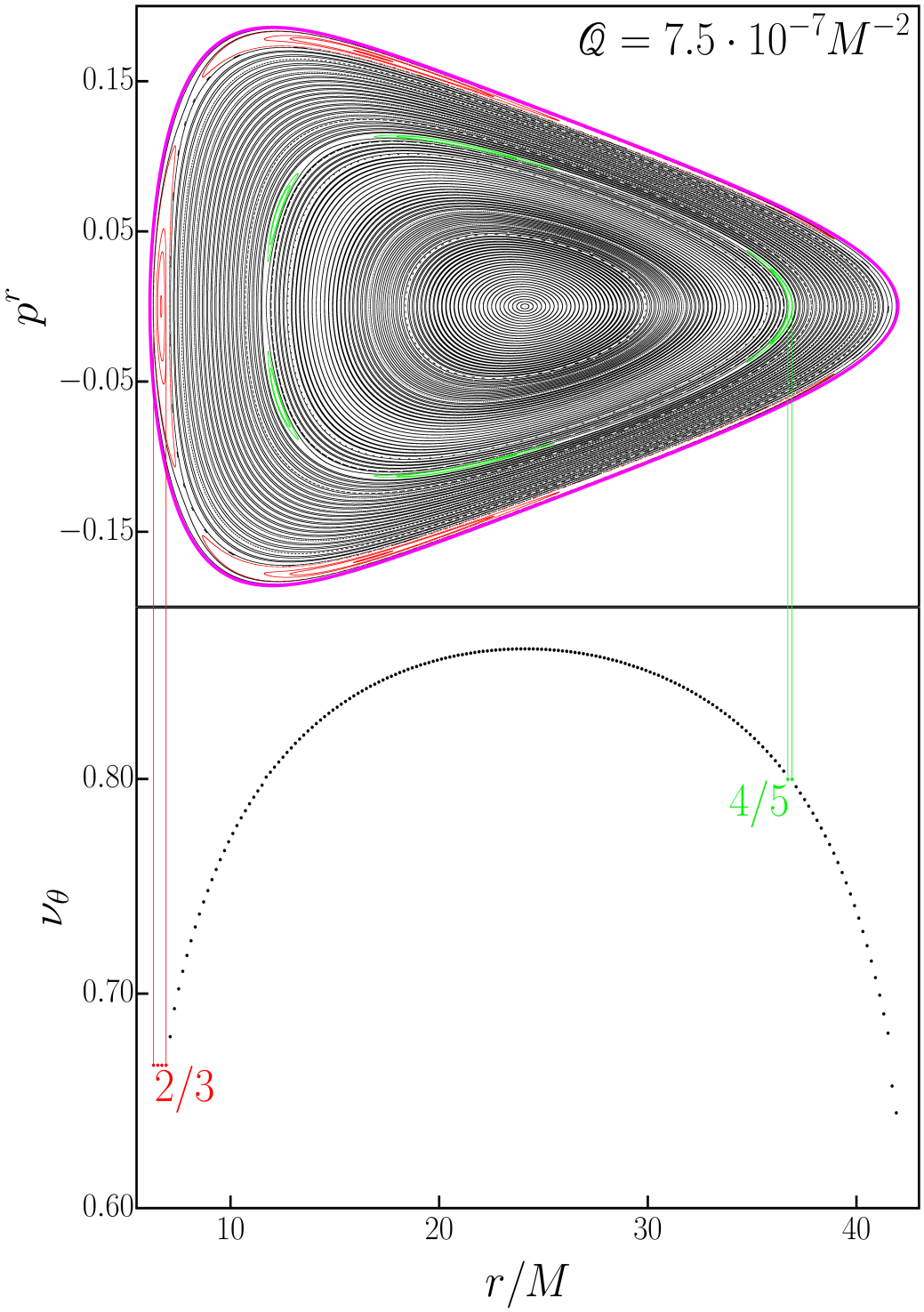

Figure 2.17: The top figure displays a Poincaré surface of section, while the bottom figure shows the corresponding rotation curve computed along the $p^r = 0$ line. The dominant resonances are prominently marked in both figures, along with their ratios of fundamental frequencies. The parameters taken are $L = 4.0M$, $E = 0.98$, $\theta\,[0] = \pi/2$ and $r\,[0] \in (6.115M; 41.915M)$ with step size $0.2M$.

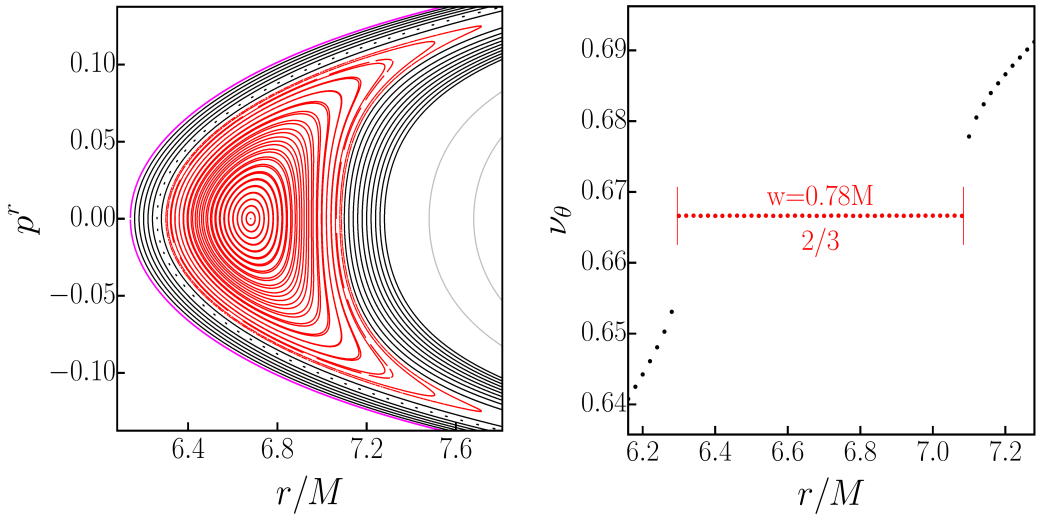

(a) The resonance $\omega^1/\omega^2 = 2/3$

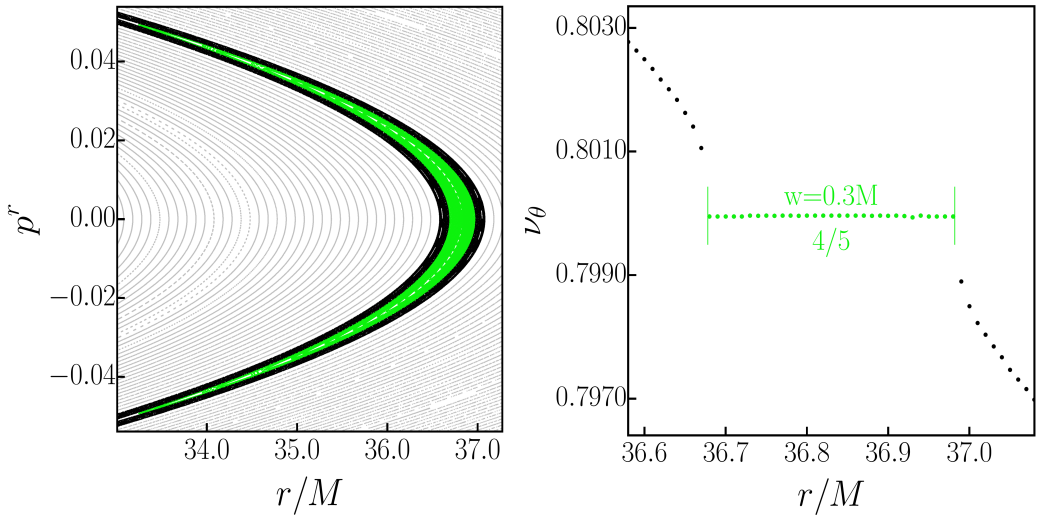

(b) The resonance $\omega^1/\omega^2 = 4/5$

Figure 2.18: Details from the Poincaré surface of section shown in Fig. 2.17 that focus on the most prominent resonances. In (a) the initial radius $r\,[0] \in (6.16M; 7.28M)$ and changes with step size 0.02; in (b) $r\,[0] \in (36.58M; 37.08M)$ with step size $0.01M$. Away from the resonance, the step size is magnified ten times, and the respective KAMs are depicted in the figure in grey colour.

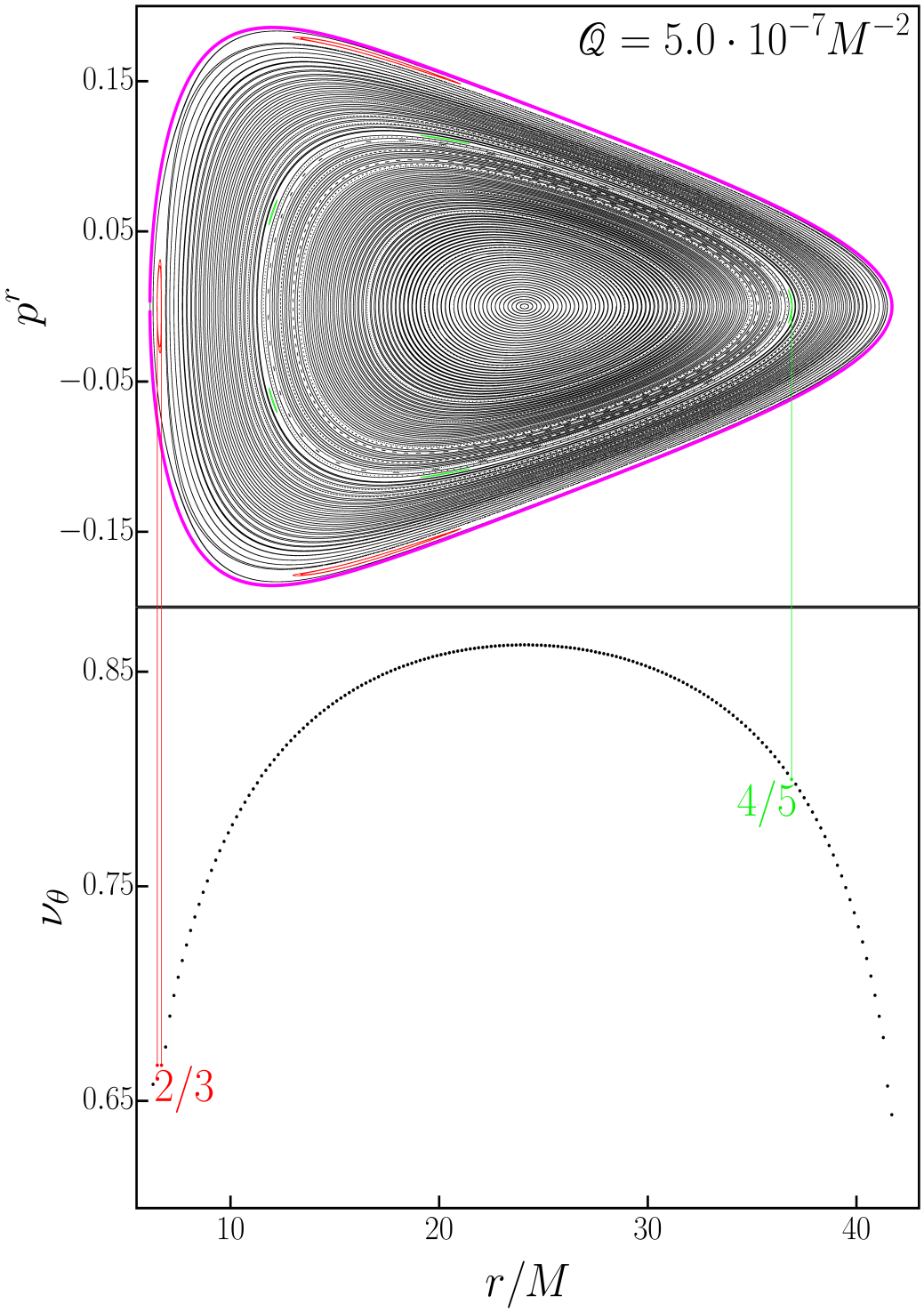

Figure 2.19: The top figure displays a Poincaré surface of section, while the bottom figure shows the corresponding rotation curve computed along the $p^r = 0$ line. The dominant resonances are prominently marked in both figures, along with their ratios of fundamental frequencies. The parameters taken are $L = 4.0M$, $E = 0.98$, $\theta\,[0] = \pi/2$ and $r\,[0] \in (6.294M; 41.694M)$ with step size $0.2M$.

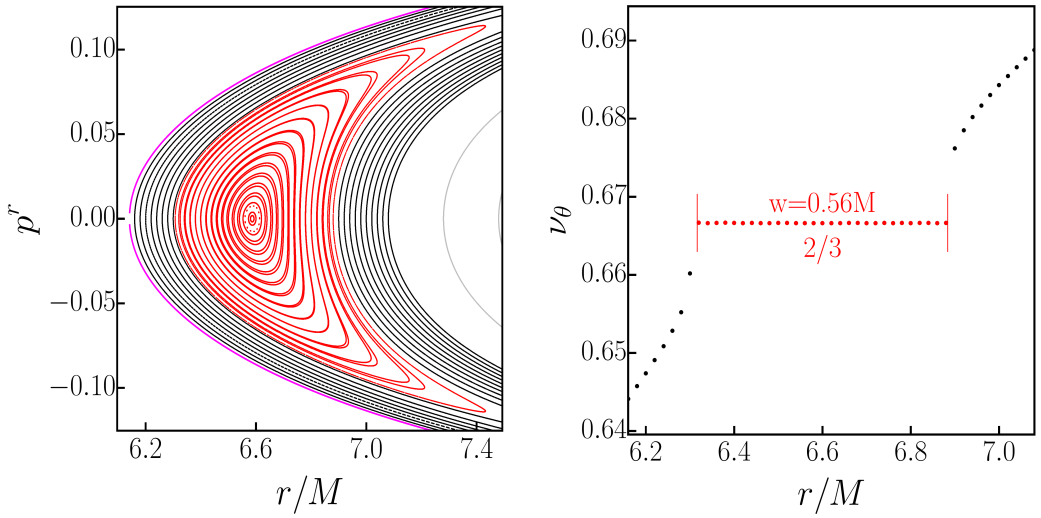

(a) The resonance $\omega^1/\omega^2 = 2/3$

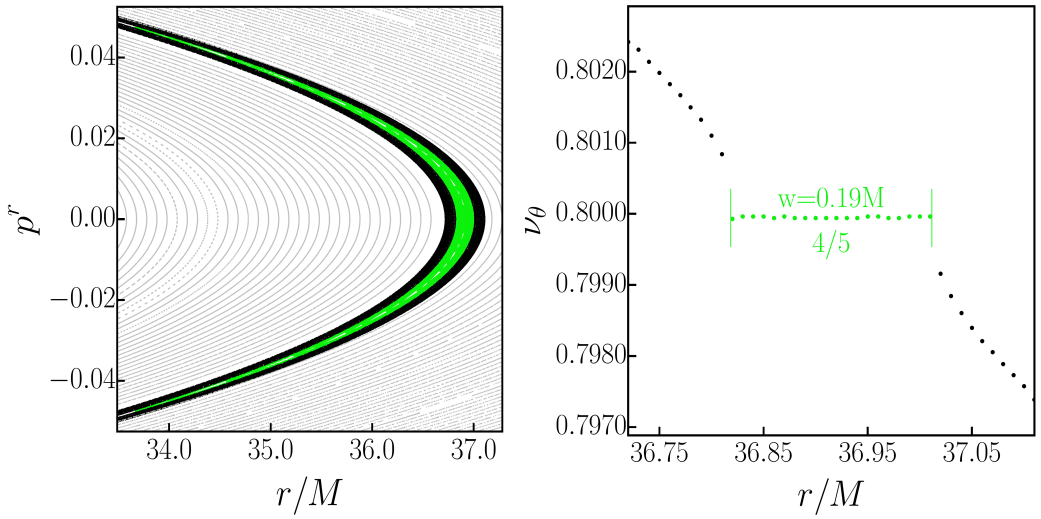

(b) The resonance $\omega^1/\omega^2 = 4/5$

Figure 2.20: Details from the Poincaré surface of section shown in Fig. 2.19 that focus on the most prominent resonances. In (a) the initial radius $r\,[0] \in (6.16M; 7.08M)$ and changes with step size $0.02M$; in (b) $r\,[0] \in (36.72M; 37.11M)$ with step size $0.01M$. Away from the resonance, the step size is magnified ten times, and the respective KAMs are depicted in the figure in grey colour.

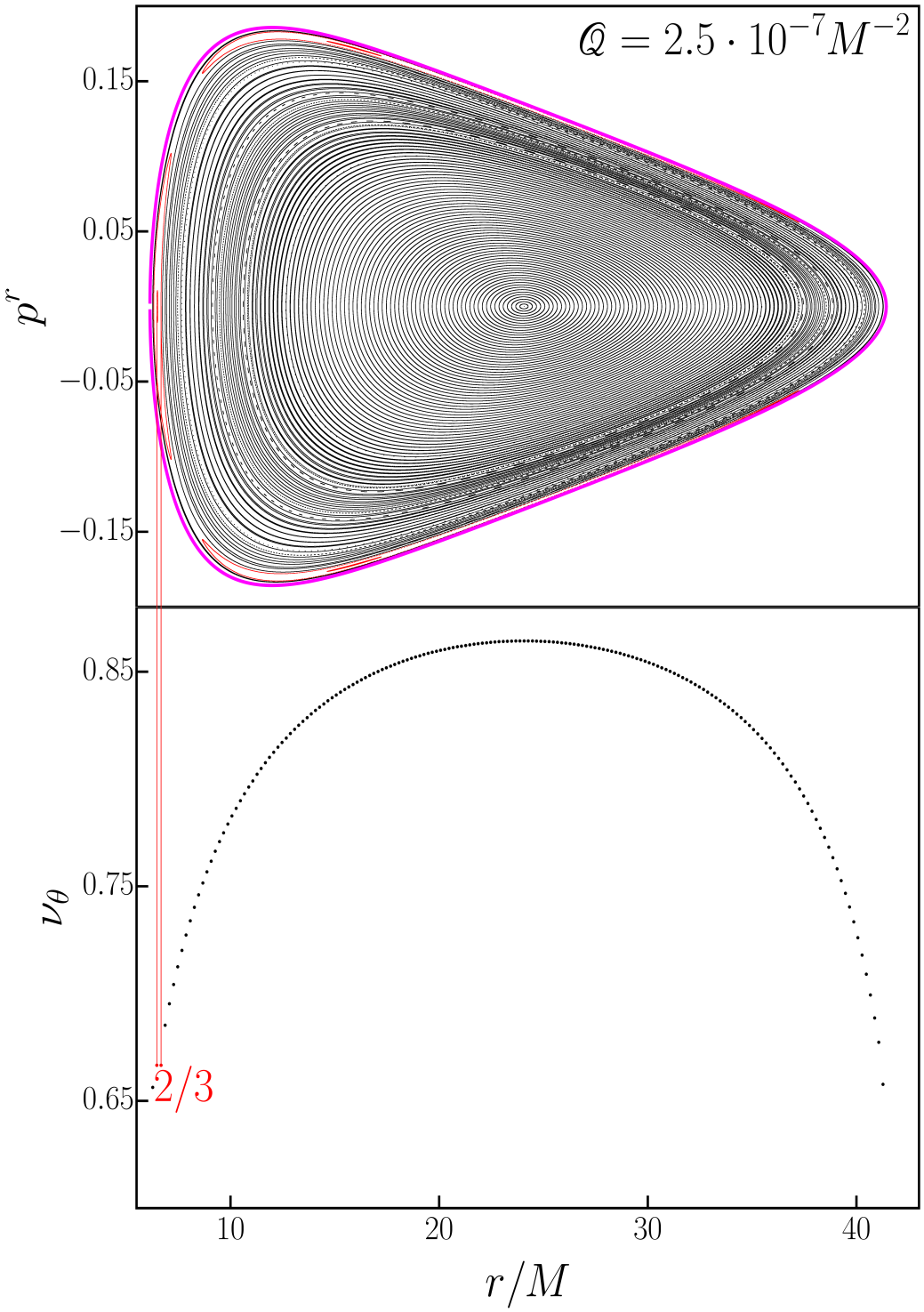

Figure 2.21: The top figure displays a Poincaré surface of section, while the bottom figure shows the corresponding rotation curve computed along the $p^r = 0$ line. The dominant resonances are prominently marked in both figures, along with their ratios of fundamental frequencies. The parameters taken are $L = 4.0M$, $E = 0.98$, $\theta\,[0] = \pi/2$ and $r\,[0] \in (6.274M; 41.274M)$ with step size $0.2M$.

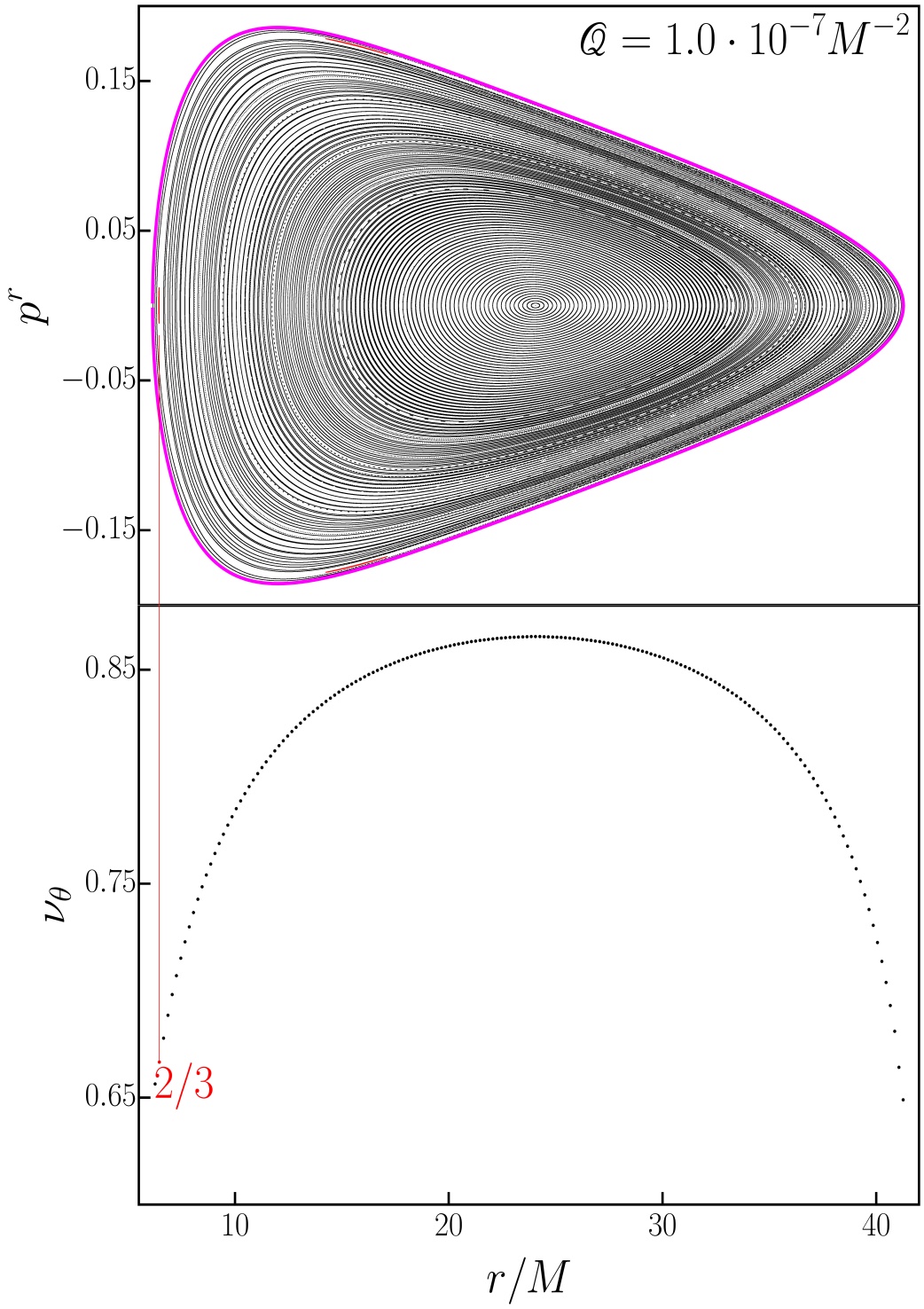

Figure 2.22: The top figure displays a Poincaré surface of section, while the bottom figure shows the corresponding rotation curve computed along the $p^r = 0$ line. The dominant resonances are prominently marked in both figures, along with their ratios of fundamental frequencies. The parameters taken are $L = 4.0M$, $E = 0.98$, $\theta\,[0] = \pi/2$ and $r\,[0] \in (6.261M; 41.261M)$ with step size $0.2M$.

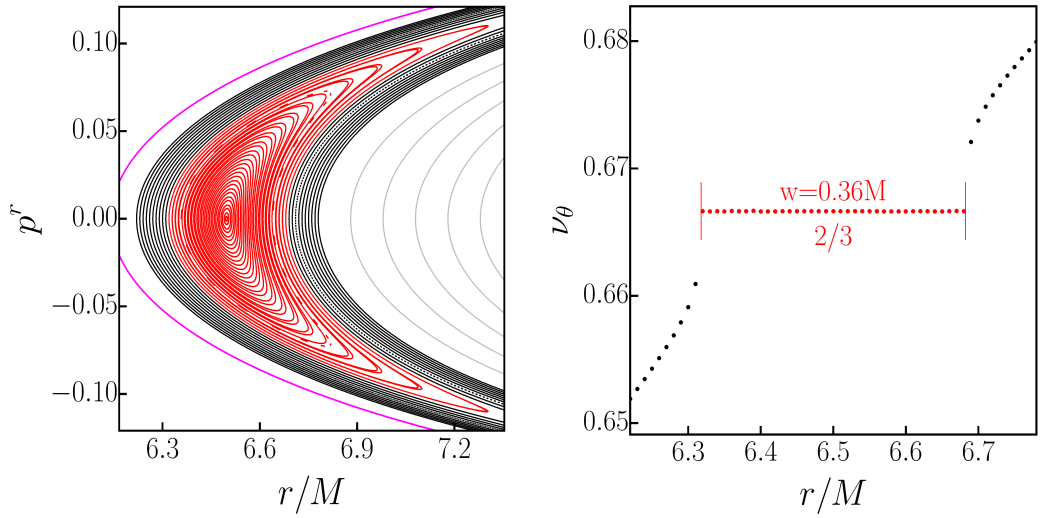

Figure 2.23: Details from the Poincaré surface of section shown in Fig. 2.21 that focus on the resonance $\omega^1/\omega^2 = 2/3$. The initial radius $r\,[0] \in (6.22M; 6.78M)$ and changes with step size $0.01M$. Away from the resonance, the step size is magnified ten times, and the respective KAMs are depicted in the figure in grey colour.

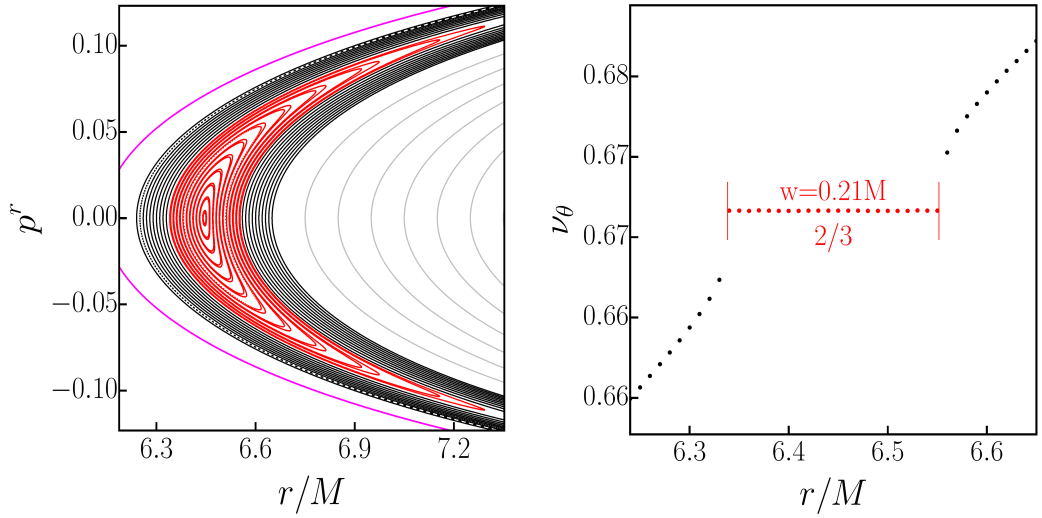

Figure 2.24: Details from the Poincaré surface of section shown in Fig. 2.22 that focus on the resonance $\omega^1/\omega^2 = 2/3$. The initial radius $r\,[0] \in (6.24M; 6.65M)$ and changes with step size $0.01M$. Away from the resonance, the step size is magnified ten times, and the respective KAMs are depicted in the figure in grey colour.

2.5.1 2/3 Resonance

The 2/3 resonance, observed in our perturbed system is depicted in red colour in Fig. 2.7 - 2.24. Table 2.1 provides a summary of the widths of the 2/3 resonance with respect to the different values of the quadrupole perturbation parameter. During the calculations, all other parameters were kept fixed, i.e. $E = 0.98$, $L = 4.0M$, and the initial conditions were chosen along the $p^r = 0$ line in Poincaré

surface of section. The value δ_w represents the step size used to obtain the width of the resonance. The final uncertainty in the width is determined by the law of propagation of uncertainty (see Ref. [40]), therefore, given as $\sqrt{2} \cdot \delta_w$.

The values from Table 2.1 are plotted in Fig. 2.25, where a linear regression is applied. During the linear regression, certain data points were omitted (marked in a particular figure with empty circles). This exclusion is due to those points corresponding to the quadrupole perturbation parameter, where a large chaotic layer surrounds the particular resonance. Large chaotic layers, in general, have a tendency to distort the width of resonance since we depart from the pendulum approximation discussed in Sec. 1.13; thus, these data points cannot be used in the linear regression analysis.

The regression parameters in equation 2.8 for the 2/3 resonance are as follows:

$$A = 0.511 \pm 0.002,$$
$$B = 2.91 \pm 0.01.$$

Therefore, the inclination is approximately equal to $A \approx 0.5$. Consequently, we establish the following relation for the perturbation parameter ϵ and the quadrupole perturbation parameter $\mathcal{Q}$ for 2/3 resonance as follows:

$$\epsilon = \mathcal{Q} M^2. \tag{2.10}$$

Hence, the perturbation parameter ϵ is directly proportional to the quadrupole perturbation parameter $\mathcal{Q}$ in a linear relationship.

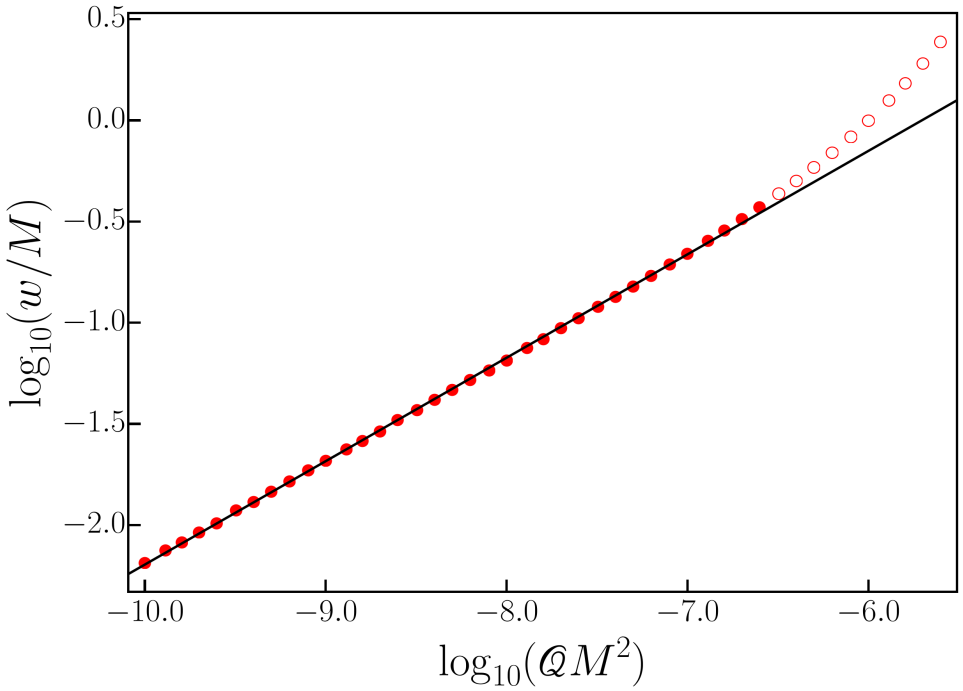

Figure 2.25: Logarithmic plot of widths of the 2/3 resonance with respect to the quadrupole perturbation parameter. The figure omits the error bars as their size is smaller than the plot symbols (the relative error was maintained below 1%). Empty circles symbolise the data that were excluded from the linear regression analysis.

Table 2.1: The values of quadrupole perturbation parameter $\mathcal{Q}$ along with the respective widths of the 2/3 resonance and their computing steps.

$\mathcal{Q}\ (\cdot M^2)$	$w\ (/M)$	$\delta_w\ (/M)$	$\mathcal{Q}\ (\cdot M^2)$	$w\ (/M)$	$\delta_w\ (/M)$
$\mathbf{1.0 \cdot 10^{-10}}$	0,0065	0,0001	$\mathbf{2.0 \cdot 10^{-8}}$	0,094	0,001
$\mathbf{1.3 \cdot 10^{-10}}$	0,0075	0,0001	$\mathbf{2.5 \cdot 10^{-8}}$	0,105	0,001
$\mathbf{1.6 \cdot 10^{-10}}$	0,0082	0,0002	$\mathbf{3.2 \cdot 10^{-8}}$	0,120	0,001
$\mathbf{2.0 \cdot 10^{-10}}$	0,0092	0,0002	$\mathbf{4.0 \cdot 10^{-8}}$	0,134	0,001
$\mathbf{2.5 \cdot 10^{-10}}$	0,0102	0,0002	$\mathbf{5.0 \cdot 10^{-8}}$	0,151	0,001
$\mathbf{3.2 \cdot 10^{-10}}$	0,0118	0,0002	$\mathbf{6.3 \cdot 10^{-8}}$	0,170	0,001
$\mathbf{4.0 \cdot 10^{-10}}$	0,0130	0,0002	$\mathbf{8.0 \cdot 10^{-8}}$	0,194	0,001
$\mathbf{5.0 \cdot 10^{-10}}$	0,0146	0,0002	$\mathbf{1.0 \cdot 10^{-7}}$	0,219	0,001
$\mathbf{6.3 \cdot 10^{-10}}$	0,0164	0,0002	$\mathbf{1.3 \cdot 10^{-7}}$	0,254	0,001
$\mathbf{8.0 \cdot 10^{-10}}$	0,0186	0,0002	$\mathbf{1.6 \cdot 10^{-7}}$	0,285	0,001
$\mathbf{1.0 \cdot 10^{-9}}$	0,0208	0,0002	$\mathbf{2.0 \cdot 10^{-7}}$	0,325	0,001
$\mathbf{1.3 \cdot 10^{-9}}$	0,0236	0,0002	$\mathbf{2.5 \cdot 10^{-7}}$	0,372	0,001
$\mathbf{1.6 \cdot 10^{-9}}$	0,0260	0,0005	$\mathbf{3.2 \cdot 10^{-7}}$	0,434	0,001
$\mathbf{2.0 \cdot 10^{-9}}$	0,0290	0,0005	$\mathbf{4.0 \cdot 10^{-7}}$	0,502	0,001
$\mathbf{2.5 \cdot 10^{-9}}$	0,0330	0,0005	$\mathbf{5.0 \cdot 10^{-7}}$	0,585	0,001
$\mathbf{3.2 \cdot 10^{-9}}$	0,0370	0,0005	$\mathbf{6.3 \cdot 10^{-7}}$	0,692	0,001
$\mathbf{4.0 \cdot 10^{-9}}$	0,0415	0,0005	$\mathbf{8.0 \cdot 10^{-7}}$	0,829	0,001
$\mathbf{5.0 \cdot 10^{-9}}$	0,0465	0,0005	$\mathbf{1.0 \cdot 10^{-6}}$	0,996	0,001
$\mathbf{6.3 \cdot 10^{-9}}$	0,052	0,001	$\mathbf{1.3 \cdot 10^{-6}}$	1,253	0,001
$\mathbf{8.0 \cdot 10^{-9}}$	0,058	0,001	$\mathbf{1.6 \cdot 10^{-6}}$	1,525	0,001
$\mathbf{1.0 \cdot 10^{-8}}$	0,065	0,001	$\mathbf{2.0 \cdot 10^{-6}}$	1,911	0,001
$\mathbf{1.3 \cdot 10^{-8}}$	0,075	0,001	$\mathbf{2.5 \cdot 10^{-6}}$	2,440	0,001
$\mathbf{1.6 \cdot 10^{-8}}$	0,083	0,001			

2.5.2 4/5 Resonance

Following the same procedure as for the 2/3 resonance in section 2.5.1, we can now analyse the second resonance, the 4/5 resonance, depicted in green colour in Fig. 2.7-2.24. Table 2.2 summarises the widths of the 4/5 resonance for different values of the quadrupole perturbation parameter. During the calculations, all other parameters were kept fixed, i.e. $E = 0.98, L = 4.0M$, and the initial conditions were chosen along the $p^r = 0$ line in Poincaré surface of section. The values from Table 2.2 are plotted in Fig. 2.26, where a linear regression is applied. Similarly to the previous analysis, during the linear regression, certain points were omitted (marked in a particular figure with empty circles). The regression parameters 2.8 for the 4/5 resonance are:

$$A = 1.038 \pm 0.004,$$
$$B = 5.85 \pm 0.03.$$

Therefore, the inclination is approximately equal to $A \approx 1.0$. Consequently, we establish the following relation for the perturbation parameter ϵ and the quadrupole

perturbation parameter $\mathcal{Q}$ for 4/5 resonance as follows:

$$\epsilon = \mathcal{Q}^2 M^4. \tag{2.11}$$

Hence, the perturbation parameter ϵ is directly proportional to the quadrupole perturbation parameter $\mathcal{Q}$ in a quadratic relationship.

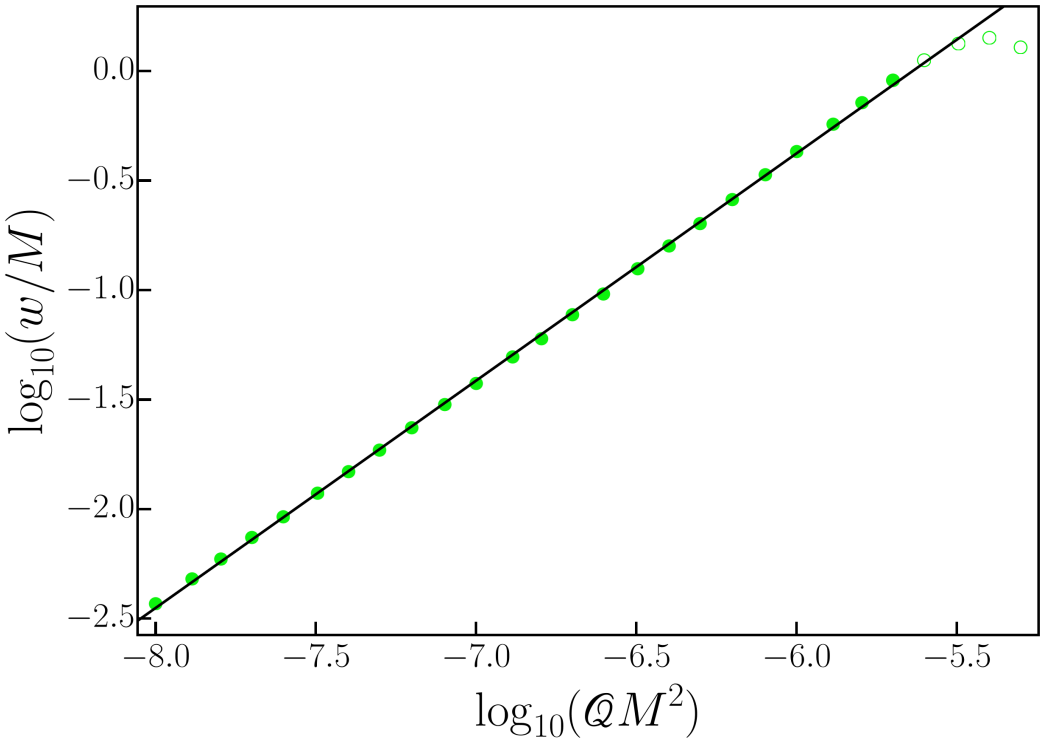

Figure 2.26: Logarithmic plot of widths of the 4/5 resonance with respect to the quadrupole perturbation parameter. The figure omits the error bars as their size is smaller than the plot symbols (the relative error was maintained below 1%). Empty circles symbolise the data that were excluded from the linear regression analysis.

2.5.3 8/11 Resonance

Continuing on the third resonance, 8/11 resonance, depicted in blue colour in Fig. 2.7-2.24. Table 2.3 provides a summary of the widths of the 8/11 resonance with respect to the different values of the quadrupole perturbation parameter. During the calculations, all other parameters were kept fixed, i.e. $E = 0.98$, $L = 4.0M$, and the initial conditions were chosen along the $p^r = 0$ line in Poincaré surface of section. The values from Table 2.1 are plotted in Fig. 2.25, where a linear regression is applied. Similarly to the previous analysis, during the linear regression, certain points were omitted (marked in a particular figure with empty circles).

The regression parameters 2.8 for the 8/11 resonance are:

$$A = 2.491 \pm 0.027,$$
$$B = 13.01 \pm 0.16.$$

Table 2.2: The values of quadrupole perturbation parameter $\mathcal{Q}$ along with the respective widths of the 4/5 resonance and their computing steps.

$\mathcal{Q}\ (\cdot M^2)$	$w\ (/M)$	$\delta_w\ (/M)$	$\mathcal{Q}\ (\cdot M^2)$	$w\ (/M)$	$\delta_w\ (/M)$
$\mathbf{1.0 \cdot 10^{-8}}$	0.0037	0.0001	$\mathbf{2.5 \cdot 10^{-7}}$	0.096	0.001
$\mathbf{1.3 \cdot 10^{-8}}$	0.0048	0.0001	$\mathbf{3.2 \cdot 10^{-7}}$	0.125	0.001
$\mathbf{1.6 \cdot 10^{-8}}$	0.0059	0.0001	$\mathbf{4.0 \cdot 10^{-7}}$	0.159	0.001
$\mathbf{2.0 \cdot 10^{-8}}$	0.0074	0.0002	$\mathbf{5.0 \cdot 10^{-7}}$	0.201	0.001
$\mathbf{2.5 \cdot 10^{-8}}$	0.0092	0.0002	$\mathbf{6.3 \cdot 10^{-7}}$	0.259	0.001
$\mathbf{3.2 \cdot 10^{-8}}$	0.0118	0.0002	$\mathbf{8.0 \cdot 10^{-7}}$	0.336	0.001
$\mathbf{4.0 \cdot 10^{-8}}$	0.0148	0.0002	$\mathbf{1.0 \cdot 10^{-6}}$	0.429	0.001
$\mathbf{5.0 \cdot 10^{-8}}$	0.0186	0.0002	$\mathbf{1.3 \cdot 10^{-6}}$	0.572	0.001
$\mathbf{6.3 \cdot 10^{-8}}$	0.0235	0.0005	$\mathbf{1.6 \cdot 10^{-6}}$	0.718	0.001
$\mathbf{8.0 \cdot 10^{-8}}$	0.0300	0.0005	$\mathbf{2.0 \cdot 10^{-6}}$	0.907	0.001
$\mathbf{1.0 \cdot 10^{-7}}$	0.0375	0.0005	$\mathbf{2.5 \cdot 10^{-6}}$	1.119	0.001
$\mathbf{1.3 \cdot 10^{-7}}$	0.0495	0.0005	$\mathbf{3.2 \cdot 10^{-6}}$	1.334	0.001
$\mathbf{1.6 \cdot 10^{-7}}$	0.060	0.001	$\mathbf{4.0 \cdot 10^{-6}}$	1.417	0.001
$\mathbf{2.0 \cdot 10^{-7}}$	0.077	0.001	$\mathbf{5.0 \cdot 10^{-6}}$	1.283	0.001

Therefore, the inclination is approximately equal to $A \approx 2.5$. Consequently, we establish the following relation for the perturbation parameter ϵ and the quadrupole perturbation parameter $\mathcal{Q}$ for 8/11 resonance as follows:

$$\epsilon = \mathcal{Q}^5 M^{10}. \tag{2.12}$$

Hence, the perturbation parameter ϵ is directly proportional to the quadrupole perturbation parameter $\mathcal{Q}$ raised to the power of five.

Table 2.3: The values of quadrupole perturbation parameter $\mathcal{Q}$ along with the respective widths of the 8/11 resonance and their computing steps.

$\mathcal{Q}\ (\cdot M^2)$	$w\ (M)$	$\delta_w\ (/M)$
$\mathbf{5.0 \cdot 10^{-7}}$	0.0022	0.0001
$\mathbf{6.3 \cdot 10^{-7}}$	0.0038	0.0001
$\mathbf{8.0 \cdot 10^{-7}}$	0.0065	0.0001
$\mathbf{1.0 \cdot 10^{-6}}$	0.0110	0.0002
$\mathbf{1.3 \cdot 10^{-6}}$	0.0205	0.0005
$\mathbf{1.6 \cdot 10^{-6}}$	0.0350	0.0005
$\mathbf{2.0 \cdot 10^{-6}}$	0.062	0.001
$\mathbf{2.5 \cdot 10^{-6}}$	0.114	0.001
$\mathbf{3.2 \cdot 10^{-6}}$	0.220	0.001
$\mathbf{4.0 \cdot 10^{-6}}$	0.382	0.001
$\mathbf{5.0 \cdot 10^{-6}}$	0.570	0.001

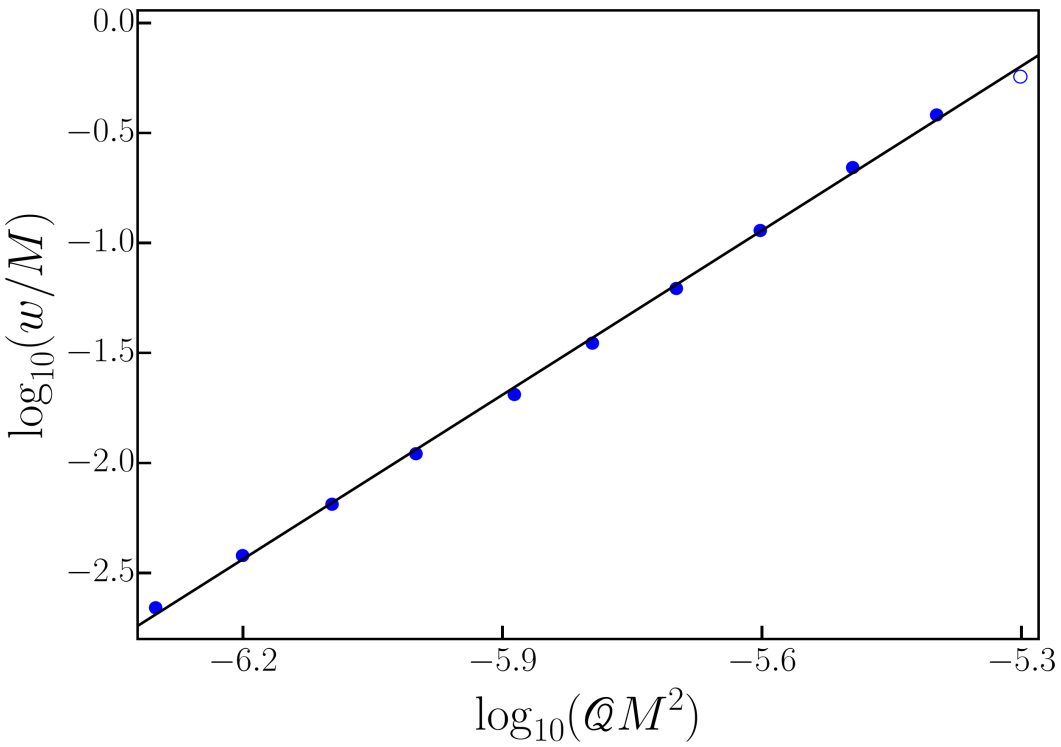

Figure 2.27: Logarithmic plot of widths of the 8/11 resonance with respect to the quadrupole perturbation parameter. The figure omits the error bars as their size is smaller than the plot symbols (the relative error was maintained below 1%). Empty circles symbolise the data that were excluded from the linear regression analysis.

2.5.4 12/17 Resonance

Applying the previously used procedure of the last resonance, 12/17 resonance, depicted in purple colour in Fig. 2.7-2.24. Table 2.4 provides a summary of the widths of the 12/17 resonance with respect to the different values of the quadrupole perturbation parameter. During the calculations, all other parameters were kept fixed, i.e. $E = 0.98, L = 4.0M$, and the initial conditions were chosen along the $p^r = 0$ line in Poincaré surface of section. The values from Table 2.4 are plotted in Fig. 2.28, where a linear regression is applied.

The regression parameters 2.8 for the 12/17 resonance are:

$$A = 3.880 \pm 0.040,$$
$$B = 20.34 \pm 0.23.$$

The inclination is approximately equal to $A \approx 4.0$. Consequently, we establish the following relation for the perturbation parameter ϵ and the quadrupole perturbation parameter $\mathcal{Q}$ for 12/17 resonance as follows:

$$\epsilon = \mathcal{Q}^8 M^{16}. \tag{2.13}$$

Hence, the perturbation parameter ϵ is directly proportional to the quadrupole perturbation parameter $\mathcal{Q}$ raised to the power of eight.

Table 2.4: The values of quadrupole perturbation parameter $\mathcal{Q}$ along with the respective widths of the 12/17 resonance and their computing steps.

$\mathcal{Q}\ (\cdot M^2)$	$w\ (/M)$	$\delta_w\ (/M)$
$\mathbf{1.0 \cdot 10^{-6}}$	0.0012	0.0001
$\mathbf{1.3 \cdot 10^{-6}}$	0.0031	0.0001
$\mathbf{1.6 \cdot 10^{-6}}$	0.0065	0.0001
$\mathbf{2.0 \cdot 10^{-6}}$	0.0168	0.0005
$\mathbf{2.5 \cdot 10^{-6}}$	0.0405	0.0005
$\mathbf{3.2 \cdot 10^{-6}}$	0.108	0.001
$\mathbf{4.0 \cdot 10^{-6}}$	0.243	0.001

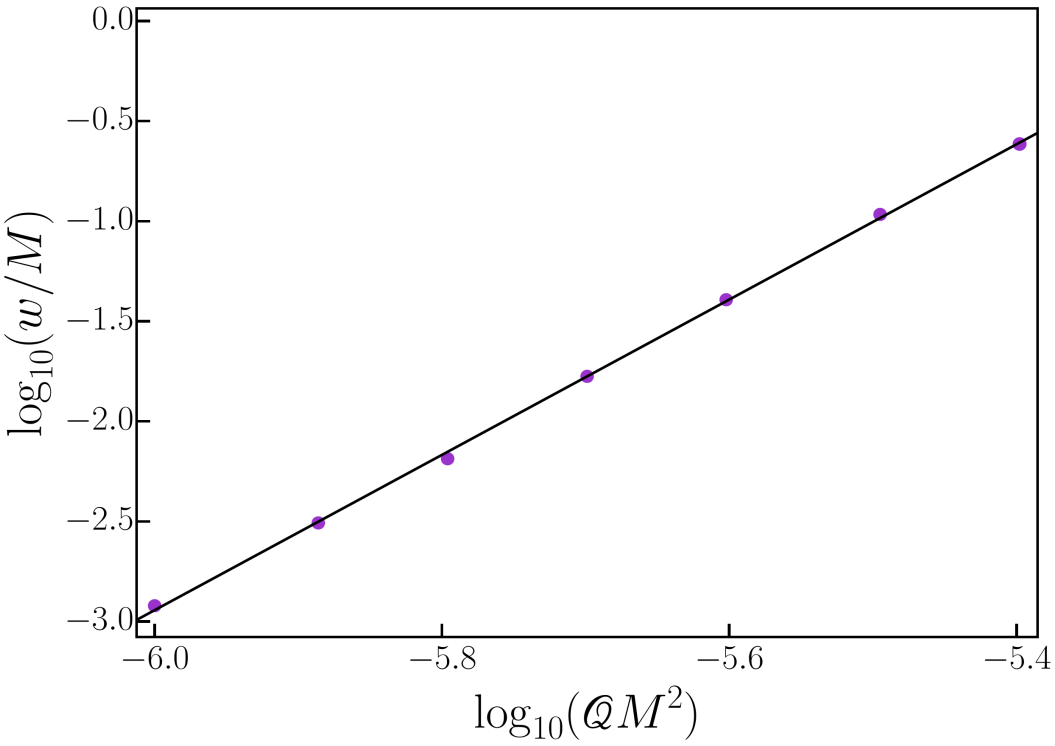

Figure 2.28: Logarithmic plot of widths of the 12/17 resonance with respect to the quadrupole perturbation parameter. The figure omits the error bars as their size is smaller than the plot symbols (the relative error was maintained below 1%).

2.6 Perturbation parameter

We see from the equations 2.10 - 2.13 that the relation between the quadrupole perturbation parameter $\mathcal{Q}$ and the perturbation parameter ϵ is not uniform and differ for each resonance. This is in contradiction with the outcomes of works [8, 41], where similar relations were consistent.

Apart from the energy and the L_z, in the Schwarzschild case, there is the total angular momentum constant. The total angular momentum is not constant of motion after the perturbation is imposed. The absence of this constant

drives the system from integrability. For small perturbation values, a total angular momentum-like quantity should oscillate around an averaged value (see Ref. [6, 42]). We speculate that the order $\mathcal{O}(Q^n)$ at which the Poisson bracket of this quantity with the Hamiltonian departs from zero near each resonance should correspond to the value we are finding. However, this speculation is yet to be investigated. What we can deduce from the obtained results is that each resonance appears to be driven from a different order in the perturbation. Moreover, it appears that the value of n in $\mathcal{O}(Q^n)$ grows as the denominator in the resonance ratio increases.

Conclusion

The first chapter provides an overview of the fundamental theory of classical mechanical systems applied in the general relativistic framework, encompassing both Lagrangian and Hamiltonian formalism. Building upon this foundation, we further developed Hamiltonian formalism and introduced advanced techniques such as canonical transformations, Hamilton-Jacobi theory and canonical perturbation theory. The geodesic equations were also derived, and their essential properties were analysed. Then we proceed to the theory of integrability and non-integrability, introducing two fundamental theorems regarding the integrability of Hamiltonian systems. Moreover, standard methods for studying deterministic chaos were presented.

The guidelines of this thesis were to gain a thorough understanding of the essential characteristics of geodesic motion in curved spacetime and acquire proficiency in methods for analysing deterministic chaos. To achieve these goals, a new program has been developed in *Wolfram Mathematica*, enabling the evolution of the geodesic motion within prescribed spacetime. Several examples of Poincaré surface of section, along with corresponding rotation curves, were provided using this program. By utilising the aforementioned methods, we could distinguish chaotic, respectively resonant trajectories. Towards the end of the thesis, we advanced further and began to study the relation between the perturbation parameter of Hamiltonian and the quadrupole perturbation parameter describing the metric.

The research led to the identification of four different relations between the perturbation parameter and the quadrupole perturbation parameter, contrary to the findings of previously published works addressing similar problems [41, 8, 43], which indicated one single relation. Therefore, we verified that the validity of such a relation is not necessarily global and can differ from resonance to resonance in the phase space.

The values of the quadrupole perturbation parameter, like $\mathcal{Q} = 10^{-7}M^2$, used in this work were slightly exaggerated, since by taking into account that the quadrupole perturbation parameter is defined as $\mathcal{Q} \equiv \mathscr{M}_r/r_r^3$, the radius of the gravitating ring should be, for instance, at $r_r = 100M$ and the mass of the ring should be $\mathscr{M}_r = 0.1M$. However, the findings remain interesting, even if they do not correspond to probable astrophysical scenarios, for which $\mathcal{Q}$ should be much smaller. With respect to the perturbation parameter and $\mathcal{Q}$ relation the only reasonable resonance is 2/3, rendering the remaining resonances negligible. Thus, it is possible to utilise the linear relation between the perturbation parameter and the quadrupole perturbation parameter in most regions of the phase space.

To expand upon this research, future works could focus on studying extreme mass ratio inspirals in such systems, as demonstrated in the work [6]. These systems generate gravitational waves in the mHz frequency band. In the upcoming years, multiple new-generation gravitational wave observatories are scheduled for launch, presenting an opportunity to observe these gravitational waves [4, 5]. Consequently, this would enhance our comprehension of these systems and allow for verifying the presented results.

Bibliography

[1] Reinhard Genzel, Frank Eisenhauer, and Stefan Gillessen. The galactic center massive black hole and nuclear star cluster. *Rev. Mod. Phys.*, 82:3121–3195, Dec 2010.

[2] Otto A. Hannuksela, Kenny C. Y. Ng, and Tjonnie G. F. Li. Extreme dark matter tests with extreme mass ratio inspirals. *Phys. Rev. D*, 102:103022, Nov 2020.

[3] Miguel C. Ferreira, Caio F. B. Macedo, and Vitor Cardoso. Orbital fingerprints of ultralight scalar fields around black holes. *Phys. Rev. D*, 96:083017, Oct 2017.

[4] Christopher P. L. Berry, Scott A. Hughes, Carlos F. Sopuerta, Alvin J. K. Chua, Anna Heffernan, Kelly Holley-Bockelmann, Deyan P. Mihaylov, M. Coleman Miller, and Alberto Sesana. The unique potential of extreme mass-ratio inspirals for gravitational-wave astronomy, 3 2019.

[5] Pau Amaro-Seoane, Heather Audley, Stanislav Babak, et al. Laser interferometer space antenna, 2017.

[6] Lukáš Polcar, Georgios Lukes-Gerakopoulos, and Vojtěch Witzany. Extreme mass ratio inspirals into black holes surrounded by matter. *Phys. Rev. D*, 106(4):044069, August 2022.

[7] Antonio Ribeiro and Francisco Nogueira Lima. An exact solution of the orbit equation for a massive particle in Schwarzschild metric, 2020.

[8] Georgios Lukes-Gerakopoulos and Vojtěch Witzany. *Nonlinear Effects in EMRI Dynamics and Their Imprints on Gravitational Waves*, pages 1625–1668. Springer Nature Singapore, Singapore, 2022.

[9] Stanislav Babak, Jonathan Gair, Alberto Sesana, Enrico Barausse, Carlos F. Sopuerta, Christopher P. L. Berry, Emanuele Berti, Pau Amaro-Seoane, Antoine Petiteau, and Antoine Klein. Science with the space-based interferometer LISA. V. Extreme mass-ratio inspirals. *Physical Review D*, 95(10):103012, May 2017.

[10] Charles W. Misner, Kip Stephen Thorne, and John Archibald Wheeler. *Gravitation*. Princeton University Press, Princeton, 2017.

[11] Lev Davidovich Landau and Evgenii Mikhailovich Lifschits. *The Classical Theory of Fields*, volume Volume 2 of *Course of Theoretical Physics*. Pergamon Press, Oxford, third edition, 1971.

[12] Jerry B. Griffiths and Jiří Podolský. *Exact Space-Times in Einstein's General Relativity*. Cambridge Monographs on Mathematical Physics. Cambridge University Press, Cambridge, 2009.

[13] Hans C. Ohanian and Remo Ruffini. *Gravitation and Spacetime*. Cambridge University Press, Cambridge, third edition, 2013.

[14] Lev Davidovich Landau and Evgenii Mikhailovich Lifschits. *Mechanics*, volume Volume 1 of *Course of Theoretical Physics*. Butterworth-Heinemann, Oxford, third edition, 1976.

[15] Herbert Goldstein, Charles Poole, and John Safko. *Classical Mechanics*. Addison-Wesley Publishing Company, Boston, third edition, 2001.

[16] Wolfgang Rindler. *Relativity: Special, General, and Cosmological*. Oxford University Press, Oxford, second edition, 2006.

[17] Richard H. Price and Kip Stephen Thorne. Lagrangian vs Hamiltonian: The best approach to relativistic orbits. *American Journal of Physics*, 86(9):678–682, 09 2018.

[18] Anatolii Isakovich Lurie. *Analytical Mechanics*. Springer, New York, 2002nd edition, 2002.

[19] Cornelius Lanczos. *The Variational Principles of Mechanics*. Dover Publications, Garden City, forth edition, 1986.

[20] Robert Geroch. What is a singularity in general relativity? *Annals of Physics*, 48(3):526–540, July 1968.

[21] Harald Iro. *Modern Approach To Classical Mechanics*. World Scientific Publishing Co. Pte. Ltd., Singapore, second edition, 2016.

[22] Karl Schwarzschild. On the gravitational field of a mass point according to Einstein's theory. *Sitzungsber. Preuss. Akad. Wiss. Berlin (Math. Phys.)*, 1916:189–196, 1916.

[23] Oliver Davis Johns. *Analytical Mechanics for Relativity and Quantum Mechanics*. Oxford University Press, Oxford, first edition, 2005.

[24] Darryl D Holm. *Geometric Mechanics: Dynamics and symmetry*. Imperial College Press, London, first edition, 2008.

[25] Vladimir Igorevich Arnold. *Mathematical Methods of Classical Mechanics*. Springer, New York, first edition, 1989.

[26] Andrey Nikolaevich Kolmogorov. On conservation of conditionally periodic motions for a small change in Hamilton's function. *Dokl. Akad. Nauk SSSR*, 98:527–530, 1954.

[27] Vladimir Igorevich Arnold. Proof of a theorem of A. N. Kolmogorov on the invariance of quasi-periodic motions under small perturbations of the Hamiltonian. *Russian Mathematical Surveys*, 18(5):9, oct 1963.

[28] Kurt Jürgen Moser. On invariant curves of area-preserving mappings of an annulus. *Nachr. Akad. Wiss. Göttingen, II*, pages 1–20, 1962.

[29] Henri Poincaré. Sur un théorème de géométrie. *Rendiconti del Circolo Matematico di Palermo*, 33:375–407, 1912.

[30] George David Birkhoff. Proof of poincaré's geometric theorem. *Transactions of the American Mathematical Society*, 14(1):14–22, 1913.

[31] Alessandro Morbidelli. *Modern Celestial Mechanics: Dynamics in the Solar System*. Taylor & Francis, 2002.

[32] Nikos Voglis, George Contopoulos, and Christos Efthymiopoulos. Detection of ordered and chaotic motion using the dynamical spectra. *Impact of Modern Dynamics in Astronomy, Colloquium 172 of the International Astronomical Union*, 73:211–220, 1990.

[33] Vladimir Igorevich Arnold, Valery Vasilevich Kozlov, and Anatoly Neishtadt. *Mathematical Aspects of Classical and Celestial Mechanics*. Encyclopaedia of Mathematical Sciences. Springer Berlin Heidelberg, 2007.

[34] Robert L. Devaney. *An Introduction to Chaotic Dynamical Systems*. Addison-Wesley Publishing Company, Boston, second edition, 1989.

[35] John Banks, John Brooks, Grant Cairns, and Peter Stacey. On Devaney's definition of chaos. *The American Mathematical Monthly*, 99(4):332–334, 1992.

[36] Carsten Knudsen. Chaos without nonperiodicity. *The American Mathematical Monthly*, 101(6):563–565, 1994.

[37] Georgios Lukes-Gerakopoulos. The non-integrability of the Zipoy-Voorhees metric. *Phys. Rev. D*, 86:044013, 2012.

[38] Kyriakos Destounis, Arthur George Suvorov, and Kostas D. Kokkotas. Testing spacetime symmetry through gravitational waves from extreme-mass-ratio inspirals. *Phys. Rev. D*, 102(6):064041, 2020.

[39] Lukáš Polcar, Petra Suková, and Oldřich Semerák. Free Motion around Black Holes with Disks or Rings: Between Integrability and Chaos–V. *Astrophys. J.*, 877(1):16, 2019.

[40] Paolo Fornasini. *The Uncertainty in Physical Measurements: An Introduction to Data Analysis in the Physics Laboratory*. Springer Science & Business Media, 2008.

[41] Ondřej Zelenka, Georgios Lukes-Gerakopoulos, Vojtěch Witzany, and Ondřej Kopáček. Growth of resonances and chaos for a spinning test particle in the Schwarzschild background. *Phys. Rev. D*, 101(2):024037, 2020.

[42] Morteza Kerachian, Lukáš Polcar, Viktor Skoupý, Christos Efthymiopoulos, and Georgios Lukes-Gerakopoulos. Action-Angle formalism for extreme mass ratio inspirals in Kerr spacetime. *arXiv e-prints*, page arXiv:2301.08150, January 2023.

[43] Sajal Mukherjee, Ondřej Kopáček, and Georgios Lukes-Gerakopoulos. Resonance crossing of a charged body in a magnetized Kerr background: An analog of extreme mass ratio inspiral. *Physical Review D*, 107(6):064005, March 2023.

[44] Fabio Bacchini, Bart Ripperda, Alexander Yuran Chen, and Lorenzo Sironi. Generalized, energy-conserving numerical simulations of particles in general relativity. I. Time-like and null geodesics. *Astrophys. J. Suppl.*, 237(1):6, 2018.

List of Figures

List of Tables

A. Attachments

A.1 Numerical Accuracy

To numerically integrate geodesic equations (1.13), a new program has been written in the *Wolfram Mathematica* environment (version 13.2.0). The program consists of two versions, which differ in their integration algorithm scheme.

The first version employed the "LocalAdaptive" algorithm, provided by default by *Wolfram Mathematica*. The algorithm dynamically adjusts the integration method and step size during the process, making it versatile for a wide range of problems. By adapting the integration method in pathological situations, this algorithm generates effective but less accurate numerical results, which are valuable for insight into the geodesic motion. However, when higher accuracy is required, this method becomes ineffective.

The second version utilises the standard fourth-order explicit Runge-Kutta algorithm. This method is widely employed in geodesic motion integration (for comparing inaccuracies with different methods frequently used in geodesics integration, see Ref. [44]), as it constantly provides accurate numerical results in most situations while maintaining reasonable computation time.

To ensure that the inaccuracies remain below a certain level, we monitor the conservation of four-momentum. Since the form of Lagrangian 1.28 has an identical form to four-momentum, it becomes synonymous with monitoring the Lagrangian. Let us denote the value of the Lagrangian at the beginning as $\mathcal{L}(0)$ and the value at step τ as $\mathcal{L}(\tau)$. Therefore, we can calculate the relative error of the Lagrangian as follows:

$$\Delta\mathcal{L}_{\mathrm{rel}} = \left| \frac{\mathcal{L}(\tau) - \mathcal{L}(0)}{\mathcal{L}(0)} \right|. \tag{A.1}$$

Fig. A.1 summarise the numerical accuracy achieved during the integration by both algorithms. In chapter 2, we integrated the geodesic equations with typically five to ten million integration steps. However, when computing the widths of resonances for the final section of the second chapter, the integration required twenty million integration steps. Nevertheless, Fig. A.1 demonstrates that the inaccuracy of RungeKutta numerical results is still reasonable even for twenty million integration steps. On the other hand, the LocalAdaptive method exhibits poor accuracy during longer integration periods. This is depicted in the top left panel of Fig. A.1, where the Poincaré surfaces of section for both methods are depicted using a specific quasi-periodic trajectory. The results reveal that the RungeKutta algorithm provides precise outcomes. At the same time, the LocalAdaptive method, during integration, shifted across several invariant curves (i.e. altered the conserved energy) and magnified the actual width of Poincaré surface of section.

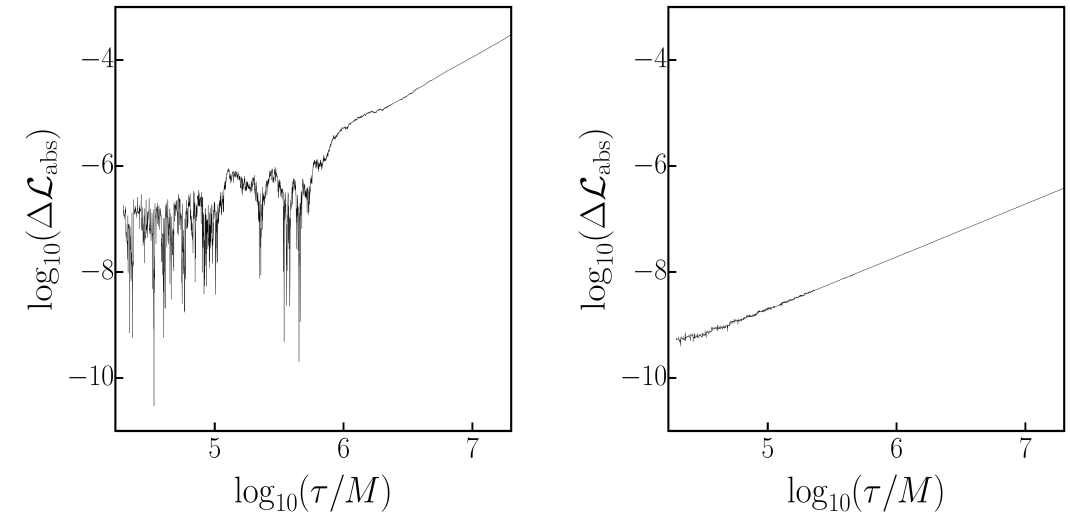

(a) LocalAdaptive: Absolute error

(b) RungeKutta: Absolute error

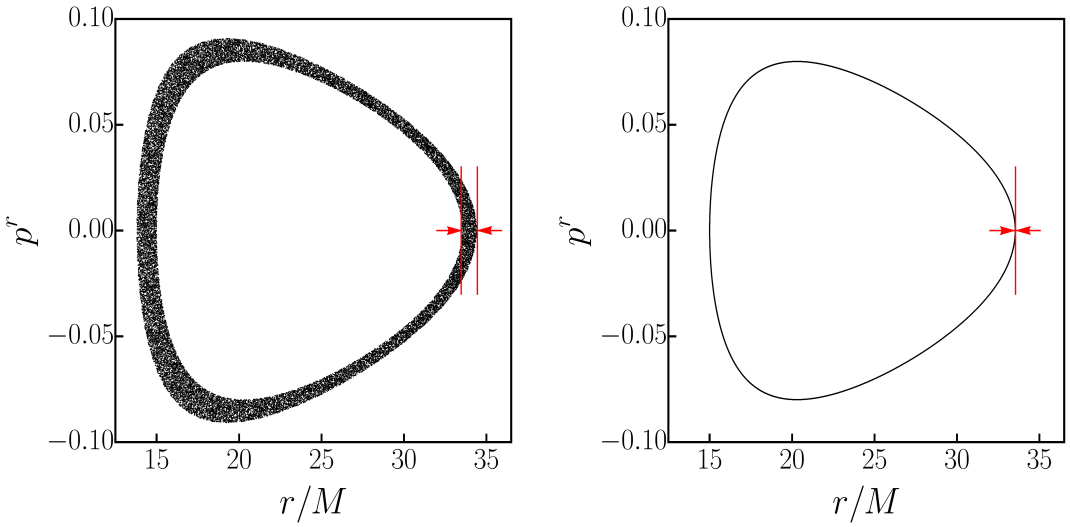

(c) LocalAdaptive: Poincare surface of section

(d) RungeKutta: Poincare surface of section

Figure A.1: The summary of the numerical inaccuracies of both employed algorithms. The top panels display the absolute error encountered during the integration process utilising twenty million steps. The bottom panels show the corresponding Poincaré surface of section for both methods. The parameters utilised during the calculation were $E = 0.98$, $L = 4.0M$, $\mathcal{Q} = 1.0 \cdot 10^{-6} M^{-2}$, $\theta\,[0] = \pi/2$, $p^r\,[0] = 0M$ and $r\,[0] = 15.0M$.